GENERATION AND EXPERIMENTAL INVESTIGATIONS OF GUSTY FLOWS IN WIND TUNNELS

A THESIS SUBMITTED TO
THE GRADUATE SCHOOL OF NATURAL AND APPLIED SCIENCES
OF
MIDDLE EAST TECHNICAL UNIVERSITY

BY

MERT ALİ ANDIRIN

IN PARTIAL FULFILLMENT OF THE REQUIREMENTS
FOR
THE DEGREE OF MASTER OF SCIENCE
IN
AEROSPACE ENGINEERING

JUNE 2022

Approval of the thesis:

GENERATION AND EXPERIMENTAL INVESTIGATIONS OF GUSTY FLOWS IN WIND TUNNELS

submitted by **MERT ALİ ANDIRIN** in partial fulfillment of the requirements for the degree of **Master of Science** i**n Aerospace Engineering, Middle East Technical University** by,

Prof. Dr. Halil Kalıpçılar
Dean, Graduate School of **Natural and Applied Sciences** _____

Prof. Dr. Serkan Özgen
Head of the Department, **Aerospace Engineering** _____

Prof. Dr. Oğuz Uzol
Supervisor, **Aerospace Engineering, METU** _____

Assist. Prof. Dr. Mustafa Perçin
Co-Supervisor, **Aerospace Engineering, METU** _____

Examining Committee Members:

Prof. Dr. Serkan Özgen
Aerospace Engineering, METU _____

Prof. Dr. Oğuz Uzol
Aerospace Engineering, METU _____

Assist. Prof. Dr. Mustafa Perçin
Aerospace Engineering, METU _____

Prof. Dr. Mehmet Metin Yavuz
Mechanical Engineering, METU _____

Assoc. Prof. Dr. Mustafa Kaya
Faculty of Aeronautics and Space Sciences, Ankara YBU _____

Date: 16.06.2022

I hereby declare that all information in this document has been obtained and presented in accordance with academic rules and ethical conduct. I also declare that, as required by these rules and conduct, I have fully cited and referenced all material and results that are not original to this work.

Name, Last name : Mert Ali Andırın

Signature :

ABSTRACT

GENERATION AND EXPERIMENTAL INVESTIGATIONS OF GUSTY FLOWS IN WIND TUNNELS

Andırın, Mert Ali
Master of Science, Aerospace Engineering
Supervisor: Prof. Dr. Oğuz Uzol
Co-Supervisor: Assist. Prof. Dr. Mustafa Perçin

June 2022, 108 pages

Wind tunnels are designed to operate at low turbulence intensities, which makes it unfeasible to study the turbulent and gusty flows that are observed in nature and in engineering applications. To conduct such studies number of unconventional methods are adopted in wind tunnels, one of which is the use of active grids. Active grids consist of motor-driven rods which accommodate flaps and they are generally placed at the inlet of wind tunnel test sections. By regulating the motion of the agitator wings, flows with high turbulence intensities and tunable properties can be achieved or atmospheric boundary layers or gusts can be generated. Active grids are usually used to generate three-dimensional flow structures. There are also more primitive devices compared to active grids to generate gust flows which are called gust generators or 2-D active grids. In this context, the main objective of this thesis is to design an active grid on an open-loop suction-type wind tunnel and investigate the gust flow characteristics of the flow field of the near wake of the active grid using experiments. For this purpose, a more primitive design, a 2D two-wing active grid, a gust generator, is used to examine the gust produced by the flapping wing in the

wake region of the gust generator. Firstly, the reduced frequency values of the vanes are changed at fixed pitching amplitude and secondly, the pitching amplitude is changed at fixed reduced frequency to investigate the gust characteristics of the flow. Unlike most of the literature, in this study, instead of using hot-wire anemometry measurements in the test section, particle image velocimetry measurements are taken in the wake of the agitator wings, which allows for exploring the physical relation between the wake structures and downstream flow profile. By the helpf of observing the whole flow field behind the gust vanes it is observed that even well-defined sinusoidal profiles of the transverse and stream-wise gust ratio in a period can be obtained using in-phase and out-of phase motion of the gust vanes, the one should be careful of the drawback of flow separation and number of coherent vortices shed into the wake.

Keywords: Active Grid, Gust, Wind tunnel, Particle Image Velocimetry

ÖZ

RÜZGAR TÜNELLERİNDE SAĞANAK AKIŞLARIN ÜRETİMİ VE DENEYSEL ARAŞTIRMALARI

Andırın, Mert Ali
Yüksek Lisans, Havacılık ve Uzay Mühendisliği
Tez Yöneticisi: Prof. Dr. Oğuz Uzol
Ortak Tez Yöneticisi: Dr. Öğr. Üyesi Mustafa Perçin

Haziran 2022, 108 sayfa

Rüzgar tünelleri, düşük türbülans yoğunluklarında çalışacak şekilde tasarlanmıştır, bu da rüzgar tünellerinde doğada ve mühendislik uygulamalarında gözlenen türbülanslı ve sağanak akışların incelenmesini olanaksız kılar. Bu tür çalışmaları yürütmek için, biri aktif ızgaraların kullanımı olan bir dizi geleneksel olmayan yöntem benimsenmiştir. Aktif ızgaralar, kanatların yerleştirildiği motor tahrikli çubuklardan oluşur ve genellikle rüzgar tüneli test bölümlerinin girişine yerleştirilir. Kanatçıklarının hareketini düzenleyerek, yüksek türbülans yoğunluklarına ve ayarlanabilir özelliklere sahip akışlar elde edilebilir veya atmosferik sınır tabakaları veya sağanaklar oluşturulabilir. Üç boyutlu akış yapıları oluşturmak için çoğunlukla aktif ızgaralar kullanılır. Ayrıca, sağanak akış üretecileri olarak adlandırılan sağanak rüzgar akışları oluşturmak için aktif ızgaralara kıyasla daha ilkel cihazlar da vardır. Bu bağlamda, bu tezin temel amacı, açık döngü emme tipi bir rüzgar tüneli üzerinde bir aktif ızgara tasarlamak ve aktif ızgaranın yakın izinin akış alanının sağnak akış özelliklerini deneyler yoluyla incelemektir. Bu amaçla, daha ilkel bir tasarım olan iki boyutlu iki kanatlı bir aktif ızgara, yani bir sağanak akış üreteci, üretecin iz bölgesinde çırpan kanat tarafından üretilen sağanak rüzgarın incelenmesi için

kullanılmıştır. İlk olarak, kanatların indirgenmiş frekans değerleri yunuslama açısı sabit tutularak değiştirilmiş ve ikinci olarak, akışın sağanak özelliklerini araştırmak için, yunuslama genliği indirgenmiş frekans sabit tutularak değiştirilmiştir. Literatürün çoğundan farklı olarak bu çalışmada, test kesitindeki sıcak tel anemometri ölçümleri yerine, kanatçıkların izinde eşzamanlı parçacık görüntülemeli hız ölçümleri alınmıştır, bu da iz yapıları ile akış aşağı akış profili arasındaki fiziksel ilişkiyi keşfetmeye olanak tanır. Rüzgar kanatlarının arkasındaki tüm akış alanının gözlemlenmesi sayesinde, bir periyotta enine ve akış yönündeki sağanak oranının iyi tanımlanmış sinüzoidal profillerinin bile, kanatçıkların faz içi ve faz dışı hareketi kullanılarak elde edilebildiği gözlenmesine rağmen, kanatlardan kaynaklı akış ayrılmasının dezavantajına ve iz bölgesine giren girdapların sayısına dikkat edilmelidir.

Anahtar Kelimeler: Aktif Izgara, Sağanak Akış, Rüzgar Tüneli, Parçacık Görüntülemeli Hız Ölçer

To my dearest parents, Tülay and Mustafa

ACKNOWLEDGMENTS

First and foremost, I want to sincere gratitude to my supervisor, Prof. Dr. Oğuz Uzol, and my co-supervisor Asst. Prof. Mustafa Perçin, for their invaluable assistance and patience over the years. I could not have finished this study without their excitement, energy, support, and advice. Also, I would like to thank Asst. Prof. Dr. Özge Başkan Perçin for her suggestions and comments during the gust generator study. I also want to thank Dr. Anas Abdulrahim who introduced me to the lab, and experiments and who always guided and supported me during my studies.

My special thanks are to my love Gözde Gözütok. I am lucky to know her and I am very grateful to her for her patience, care and support and for being there for me whenever I need. I am also thankful to Orhun Bulut for his friendship, wisdom, supportive approach, and encouragement. I also want to thank Gökçe Törenli and Nazlı Barçın Doğan for their support and help during my studies. I also want to thank my cousins Alican Andırın and Ecem Özdemir for their support.

I have been working with lots of graduate and undergraduate students in the Aerodynamics lab, for which I am very grateful. I have enjoyed working and studying with you all, İmge Yığılı, Abdelrahman Hassanein, Buğrahan Öztürk, M. Tuğrul Akpolat, Mahdi Yazdanpanah, Burcu Erol, Batuhan Doğan, and, Yusufcan Taşmaz. I would also like to thank the staff of ODTÜ RÜZGEM for their support.

Finally, I would like to thank my parents and family, Mustafa and Tülay Andırın and my brother Arda. I would not have been able to achieve my goals if it had not been for their unwavering love and support. They always have been my inspiration and will continue to be my driving force in my life.

This study is supported by the Scientific and Technological Research Council of Turkey (TÜBITAK) under project number 120M497 and by the METU Center for Wind Energy (RÜZGEM). Their support is greatly appreciated.

TABLE OF CONTENTS

ABSTRACT v

ÖZ vii

ACKNOWLEDGMENTS x

TABLE OF CONTENTS xi

LIST OF TABLES xiii

LIST OF FIGURES xiv

LIST OF ABBREVIATIONS xix

LIST OF SYMBOLS xx

CHAPTERS

1 INTRODUCTION 1

1.1 Overview of Gust Generators 2

1.1.1 Definition of the Gust 2

1.1.2 Gust Generation in a Wind Tunnel 5

1.1.3 Overview of Active Grids 10

1.2 Objectives and Thesis Layout 20

2 EXPERIMENTAL SETUP AND MEASUREMENT METHODS 21

2.1 Active Grid Design 21

2.1.1 Wind Tunnel 21

2.1.2 Conceptual Design of the Active Grid Frame 22

2.1.3 Motor Sizing of the Active Grid 27

2.1.4 Motion Controller Architecture Design 31

2.2 2D Active Grid System 33

2.2.1 Wind Tunnel and Gust Generator 33
2.2.2 PIV Setup 35
2.2.3 Data Processing Techniques 46
2.2.4 Analysis of the Measurement Errors 47
3 RESULTS AND DISCUSSION 51
3.1 Temporal Results 51
3.2 Spatial Results 59
3.2.1 Effect of Increasing Amplitude on the Gust Parameters 63
3.2.2 Effect of Increasing Reduced Frequency on the Gust Parameters 66
4 CONCLUSIONS AND FUTURE WORK 69
REFERENCES 73
APPENDICES
A. Contour plots for all the test cases 79

LIST OF TABLES

TABLES

Table 1.1: Details of the Gust Generator Setup in the literature [I] 9
Table 1.2: Details of the Gust Generator Setup in the literature [II] 10
Table 1.3: Wind Tunnel test section areas and background freestream turbulence intensity values in the literature where active grids are used 19
Table 2.1: Some important dimensions of active grid design 27
Table 2.2: 2D2C PIV Experimental Setup parameters (I) 38
Table 2.3: 2D2C PIV Experimental Setup Parameters (II) 39
Table 2.4: Phase Locked 2D2C PIV triggered angle values of a single period for different reduced frequencies 44
Table 2.5: Phase Locked 2D2C PIV triggered angle values of a single period for different amplitudes 45

LIST OF FIGURES

FIGURES

Figure 1.1: Examples of EOG (left) and ECG (right) types from IEC 61400-1 standards (IEC 61400-1)..... 3
Figure 1.2: Comparison between measured gust events and IEC gust model. (Rakib et al., 2019)..... 3
Figure 1.3: Three different types of discrete gust encounters (Jones and Cetiner, 2021)..... 4
Figure 1.4: The first gust generator facility at Langley NASA, 1945 5
Figure 1.5: The Transonic Dynamics Tunnel at Langely with the gust vanes installed upstream of a scaled B-52 aircraft model 7
Figure 1.6: Flow visualization experiments of the gust generator system at different reduced frequency values from Delft University of Technology (Lancelot et.al. 2015)..... 9
Figure 1.7: Makita-style (left) and low-blockage (right) flap designs designed for the University of Oldenburg active grid system (Reinke et al., 2017) 16
Figure 1.8: Active Grid drawing designed by Makita (Makita and Sassa 1991) 17
Figure 1.9: Active grid application consisting of adjacent flaps placed perpendicular to each other 18
Figure 2.1: RÜZGEM C3 open-loop suction type wind tunnel 22
Figure 2.2: Preliminary conceptual design of the Active Grid..... 23
Figure 2.3: Active grid system chassis designs: (a) Initial design based on the slide system; (b) the second design connected to the fixed cross-section duct; (c) final design with frame of sigma profiles 24
Figure 2.4: Active grid detailed design flap dimensions and clearance amounts ... 25
Figure 2.5: Active grid detailed design placement of horizontal and vertical bars . 26
Figure 2.6: 3-D CAD sketch of the detailed design of the active grid 26
Figure 2.7: Blade orientation and force/torque values used in the motor sizing study 28

Figure 2.8: Servo motor motion controller GUI for the active grid written in LABVIEW software 32
Figure 2.9: Variation of the position information received from the motors performing a sinusoidal pitching motion with a frequency of 10 Hz and an amplitude of 12° for 2 periods 33
Figure 2.10: RUZGEM C1 open-loop wind tunnel's schematics and coordinate system. 34
Figure 2.11: RÜZGEM C1 open-circuit wind tunnel and integrated two-dimensional gust generator (left), a three-dimensional CAD drawing of two-dimensional gust generator (right) 35
Figure 2.12: 2D2C PIV experiment setup configuration with the gust generator system 37
Figure 2.13: The overlap zones and the field of views are shown in the PIV measurement domain with the NACA 0015 gust vanes 40
Figure 2.14: Comparison of the vane position data for the in-phase and the out-of-phase cases at k=0.25 and at $\theta = 12^{\circ}$ for a period. 42
Figure 2.15: Representation of the phase-locked PIV angles in a period for three different frequency test cases at a fixed pitching amplitude for out-of-phase and in-phase motions (motor position data is presented by black and blue lines, the phase-phase locked angles are presented by red dots.) 43
Figure 2.16: Representation of the phase-locked PIV angles in a period for three different pitching amplitude test cases at a fixed reduced frequency for out-of-phase and in-phase motions (motor position data is presented by black and blue lines, the phase-phase locked angles are presented by red dots.) 43
Figure 3.1: Comparison of the angle of incidence ($\phi \circ$) for different frequencies and different amplitudes of a sinusoidal period for both in and out-of-phase cases at x/c=0.6 and y/c=0 location..... 52
Figure 3.2: Comparison of the normalized transverse gust ratio $v/U\infty$ for different frequencies and different amplitudes of a sinusoidal period for both in and out-of-phase cases at x/c=0.6 and y/c=0 location 53

Figure 3.3: Comparison of the normalized stream-wise gust ratio $u/U\infty$ for different frequencies and different amplitudes of a sinusoidal period for both in and out-of-phase cases at x/c=0.6 and y/c=0 location.....54
Figure 3.4: Comparison of AoI variations at near and far wake regions (x/c=0.6, x/c=4 and x/c=6) for three different reduced frequencies *k*=0.13, *f* =5 Hz (black) *k*=0.19 , f =7.5 Hz (blue) *k*=0.25 , *f* =10 Hz (red) at y/c=0 and at $U\infty$=10 m/s.....55
Figure 3.5: Comparison of transverse gust ratio variations at near and far wake regions (x/c=0.6, x/c=4 and x/c=6) for three different reduced frequencies *k*=0.13, *f* =5 Hz (black) *k*=0.19 , f =7.5 Hz (blue) *k*=0.25 , *f* =10 Hz (red) at y/c=0 and at $U\infty$=10 m/s 55
Figure 3.6: Comparison of stream-wise gust ratio variations at near and far wake regions (x/c=0.6, x/c=4 and x/c=6) for three different reduced frequencies *k*=0.13, *f* =5 Hz (black) *k*=0.19 , f =7.5 Hz (blue) *k*=0.25 , *f* =10 Hz (red) at y/c=0 and at $U\infty$=10 m/s 56
Figure 3.7: Comparison of AoI variations at near and far wake regions (x/c=0.6, x/c=4 and x/c=6) for three different pitching amplitude $\theta = 8°$ (black) , $\theta = 12°$ (blue), $\theta = 16°$ (red) at y/c=0, at a fixed frequency *k=0.25* and at $U\infty$=10 m/s ..57
Figure 3.8: Comparison of transverse gust ratio variations at near and far wake regions (x/c=0.6, x/c=4 and x/c=6) for three different pitching amplitude $\theta = 8°$ (black) , $\theta = 12°$ (blue), $\theta = 16°$ (red) at y/c=0, at a fixed frequency *k=0.25* and at $U\infty$=10 m/s.....57
Figure 3.9: Comparison of stream-wise gust ratio variations at near and far wake regions (x/c=0.6, x/c=4 and x/c=6) for three different pitching amplitude $\theta = 8°$ (black) , $\theta = 12°$ (blue), $\theta = 16°$ (red) at y/c=0, at a fixed frequency *k=0.25* and at $U\infty$=10 m/s.....58
Figure 3.10: Stream-wise gust ratio contour plots of FOV for reduced frequency *k* = 0.25 and with a maximum amplitude of $\theta = 12°$ in-phase case at different phase angles.....60

Figure 3.11: Transverse gust ratio contour plots of FOV for reduced frequency k =0.25 and with a maximum amplitude of $\theta = 12°$ in-phase case at different phase angles 60
Figure 3.12: Contours of out-of-plane vorticity at the reduced frequency of k = 0.25 and the pitching amplitude of $\theta = 12°$ for in-phase case at different phase angles 61
Figure 3.13: Stream-wise gust ratio contour plots of FOV for reduced frequency k = 0.25 and with a maximum amplitude of $\theta = 12°$ out-of-phase case at different phase angles 62
Figure 3.14: Transverse gust ratio contour plots of FOV for reduced frequency k = 0.25 and with a maximum amplitude of $\theta = 12°$ out-of-phase case at different phase angles 62
Figure 3.15: Contours of out-of-plane vorticity at the reduced frequency of k = 0.25 and the pitching amplitude of $\theta = 12°$ out-of-phase case at different phase angles 63
Figure 3.16: Comparison of the stream-wise and transverse gust ratio and vorticity for different maximum deflection angles for their maximum amplitudes (8°, 12°, 16°) at k=0.25 for in-phase case 64
Figure 3.17: Comparison of the stream-wise and transverse gust ratio and vorticity for different maximum deflection angles for their maximum amplitudes (-8°, -12°, -16°) at k=0.25 for in-phase case 64
Figure 3.18: Comparison of the stream-wise and transverse gust ratio and vorticity for different maximum deflection angles for their maximum amplitudes (8°, 12°, 16°) at k=0.25 for out-of-phase case 65
Figure 3.19: Comparison of the stream-wise and transverse gust ratio and vorticity for different maximum deflection angles for their maximum amplitudes (-8°, -12°, -16°) at k=0.25 for out-of-phase case 65

Figure 3.20: Comparison of the stream-wise and transverse gust ratio and vorticity fields for different reduced frequencies (k=0.13, k=0.19, and k=0.25) at the same deflection angle $\theta = 12°$ for in-phase case 67
Figure 3.21: Comparison of the stream-wise and transverse gust ratio and vorticity fields for different reduced frequencies (k=0.13, k=0.19, and k=0.25) at the same deflection angle $\theta = -12°$ for in-phase case 67
Figure 3.22: Comparison of the stream-wise and transverse gust ratio and vorticity fields for different reduced frequencies (k=0.13, k=0.19, and k=0.25) at the same deflection angle $\theta = 12°$ for out-of-phase case 68
Figure 3.23: Comparison of the stream-wise and transverse gust ratio and vorticity for different reduced frequencies (k=0.125, k=0.188, and k=0.251) at the same deflection angle $\theta = -12°$ for out-of-phase case 68

LIST OF ABBREVIATIONS

ABBREVIATIONS

AoI	Angle of Incidence
2D2C PIV	Two-dimensional Two-component Particle Image Velocimetry
CAD	Computer Aided Drawing
cRIO	Compact Reconfigurable Input Output
ECG	Extreme Coherent Gust
EOC	Extreme Operating Condition
FOV	Field of View
GR	Gust Ratio
kW	kiloWatt
Nd:YAG	Neodymium-Doped Yttrium Aluminum Garnet (Nd:$Y_3AI_5O_{12}$)
PIV	Particle Image Velocimetry
PLA	Polylactic Acid
RPM	Revolutions per Minute
TTL	Transistor-Transistor Logic

LIST OF SYMBOLS

SYMBOLS

C	Chord of the gust vane [m]
f	Flap rotation frequency [$1/s$]
ρ	Density [kg/m^3]
J	Moment of Inertia of the system
J_{rod}	Moment of Inertia of the active grid rod
k	Reduced frequency
L	Integral length scale
m_{flap}	Mass of the active grid flaps [kg]
m_{rod}	Mass of the active grid rods [kg]
Re_M	Reynolds number based on mesh size
Re_λ	Reynolds number based on Taylor's microscale
t	Time [s]
T	Period [s]
U	Mean streamwise velocity [m/s]
U_∞	Freestream velocity [m/s]
V	Mean lateral velocity [m/s]
ϵ	Dissipation rate [m^2/s^3]
η	Kolmogorov length scale

s_{ij}	Turbulence strain rate
θ	Deflection angle of the gust vanes [degrees]
$\bar{\theta}$	Maximum pitching amplitude of the gust vanes [degrees]
ϕ	Angle of Incidence of the flow velocity [degrees]
τ	Inertia torque [Nm]
ν	Kinematic viscosity [Ns/m^2]
ω	Angular speed of the flap [rad/s]

CHAPTER 1

INTRODUCTION

Varying inflow conditions affects the aerodynamic systems in nature. Gust is an example of these inflow conditions. Gust can be stated as a sudden change of the mean wind speed. Wind turbines are one of the most suitable examples of the effect of varying inflow conditions on the aerodynamic systems. The rotating blades are confronted with wind gusts and as a result, dynamic stall is observed on the wind turbine blades. Dynamic stall causes excessive loads on the turbine blades and those loads lead to fatigue in long-term applications. Recognizing the significance of gusts in aviation development, the National Advisory Council on Aeronautics (NACA) set the first gust loading regulations for aircraft in 1934 (Harold N. et al. 1989). This sparked the development of the first gust wind tunnel facility shortly after. Since then, numerous facilities capable of inducing various forms of gusts or unsteadiness have been developed. This abundance of testing has resulted in a firm foundation of knowledge in the subject of unstable aerodynamics, but with new technologies emerging, there is still a need for further research in this area. There are also different unsteady flow regimes which affects the aerodynamic systems such as turbulence. It is a three-dimensional flow regime that we experience in many aspects of our lives. It is complex, irregular, unpredictable, and unsteady. Ocean currents and river flows, atmospheric boundary layer flows on the earth's surface, photosphere layers of the sun and similar stars, almost all combustion processes, boundary layer flows that develop on aircraft wings, wake areas of automobiles, ships, or planes, and in-pipe flows are all examples of this chaotic regime (Tennekes and Lumley, 1972). Although the examples above can be extended to numerous natural flow conditions and technical applications, even this small sample size indicates that many flow types

in various domains are in the turbulent regime, necessitating a thorough study and understanding of turbulent flows. Despite this requirement and several investigations since Reynolds' pioneering work (Reynolds, 1883a; Reynolds, 1883b), many questions about this complex flow regime explained by nonlinear Navier-Stokes equations remain unanswered (Mydlarski, 2017). Today, generating turbulent flows in wind tunnels is possible using devices called active grid. Since the turbulent flow regime is mostly three dimensional, the use of active grids provides ability for such flows. However, wind gusts generated in wind tunnels are mostly two-dimensional and to generate wind gusts 2-D active grids or gust generators are used in the literature.

1.1 Overview of Gust Generators

In this section, the common flow type that is seen in nature and investigated in this study, gust is defined briefly, and later literature review of the gust generators is introduced.

1.1.1 Definition of the Gust

Gusts are sudden changes in the direction and amplitude of airflow velocity. Turbulence, vortices, downdrafts, updrafts, and shear layers are all examples of flow structures found in gusts (Jones and Cetiner, 2021). Gusts are defined as a mathematical model in IEC 61400-1 standards. It is an international standard for wind turbine safety and wind turbine design requirements. Gusts are defined as Extreme Operating Condition (EOC) gusts and Extreme Coherent Gusts (ECG) types in IEC standards.

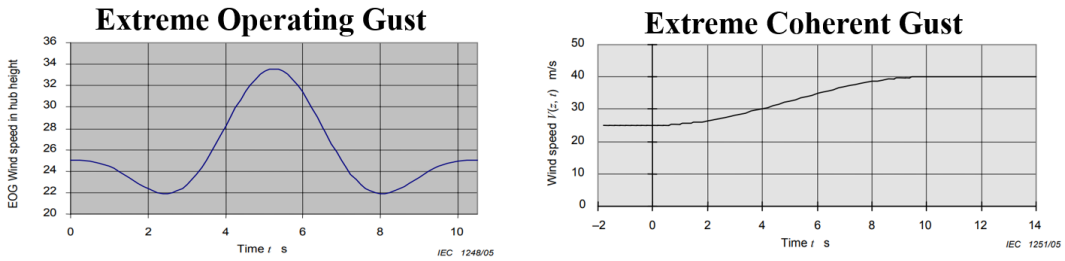


Figure 1.1: Examples of EOG (left) and ECG (right) types from IEC 61400-1 standards (IEC 61400-1)

Figure 1.1 shows the change of wind speeds for the EOG and ECG types according to different mathematical models from IEC 61400-1 standard. These models are derived from the gust types observed in nature using measurements of the wind speed. Rakib et al. (2019) showed that measured gust events in nature fits with the IEC EOG model (see Figure 1.2).

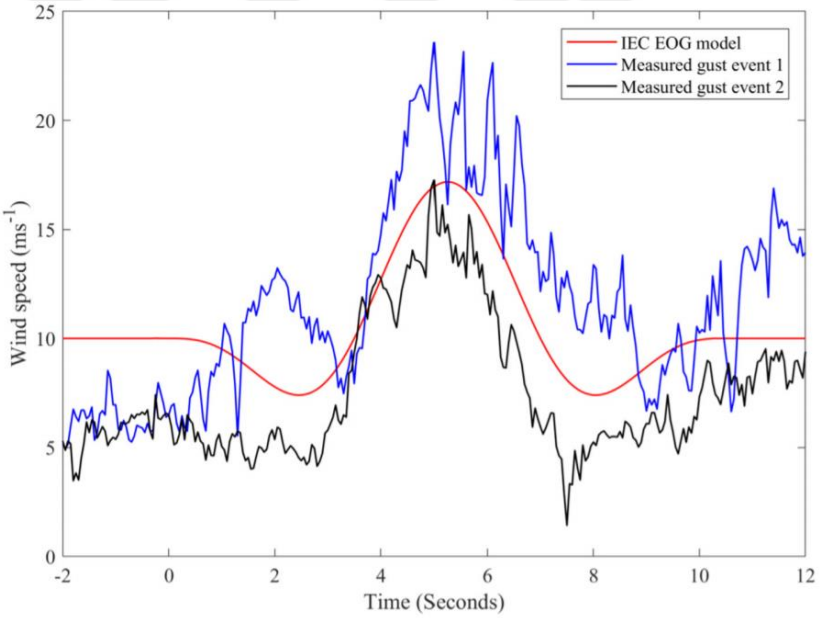


Figure 1.2: Comparison between measured gust events and IEC gust model. (Rakib et al., 2019)

In addition to the mathematical models defined for gust types in IEC standards, gusts in the atmosphere can be categorized into two different types: continuous and discrete. Continuous gusts are ergodic, meaning they are stationary in time and are

isotropic. The Dryden or von Kármán models (Beal 1993), both of which are composed of rational power spectral densities defined for translational gust velocities in each Cartesian axis, are the most often used stochastic models for evaluating continuous gusts. On the other hand, a discrete gust is an isolated flow structure that can take a variety of shapes, some of which can be named transverse, stream-wise, and vortex about the vehicle's nominal flight speed, U_∞. These three types of discrete gust are shown in Figure 1.3.

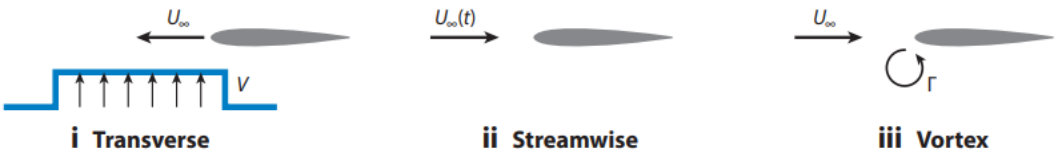


Figure 1.3: Three different types of discrete gust encounters (Jones and Cetiner, 2021)

Different parameters can be used to define the amplitude of the gust in the desired direction. One of the most common parameters is called the gust ratio. It is the ratio of the vertical component of the airflow velocity at the desired location to the free stream velocity. This type of gust ratio is called transverse gust ratio and is defined as $GR = v/U_\infty$. Besides, the changing amplitude of the periodically changing stream-wise velocity component in a flow field is crucial for gust flows. Hence, in addition to the traverse gust ratio, the periodic stream-wise gust ratio is another key non-dimensional parameter and described as $GR = u/U_\infty$. Furthermore, artificial gust generating devices are critical for studies involving the unstable response of lift-producing surfaces. In the next section, how gust generation in a wind tunnel is evolved in the history will be discussed and some critical parameters of the gust generation mechanisms in the near past will be mentioned.

1.1.2 Gust Generation in a Wind Tunnel

Wind turbines, helicopters, micro-air vehicles, and airplane studies have all become increasingly popular in recent years (Wei et al., 2019). Hence, conducting wind tunnel studies under more realistic inflow conditions is critical for gaining a better understanding of airflow. Wind tunnels, on the other hand, are meant to function at low turbulence intensities and under uniform flows, making it impossible to investigate turbulent or gusty flows seen in nature and engineering applications in them. Therefore, active grids can be employed in subsonic wind tunnels to generate gusts. For instance, the effects of the gusts on the flying animals and micro air vehicles are also investigated in a wind tunnel that uses an active grid at Stanford University Quin et al. (2017). Even though the active grids are the instruments to generate gusts in wind tunnels, they are not the only way for these studies.

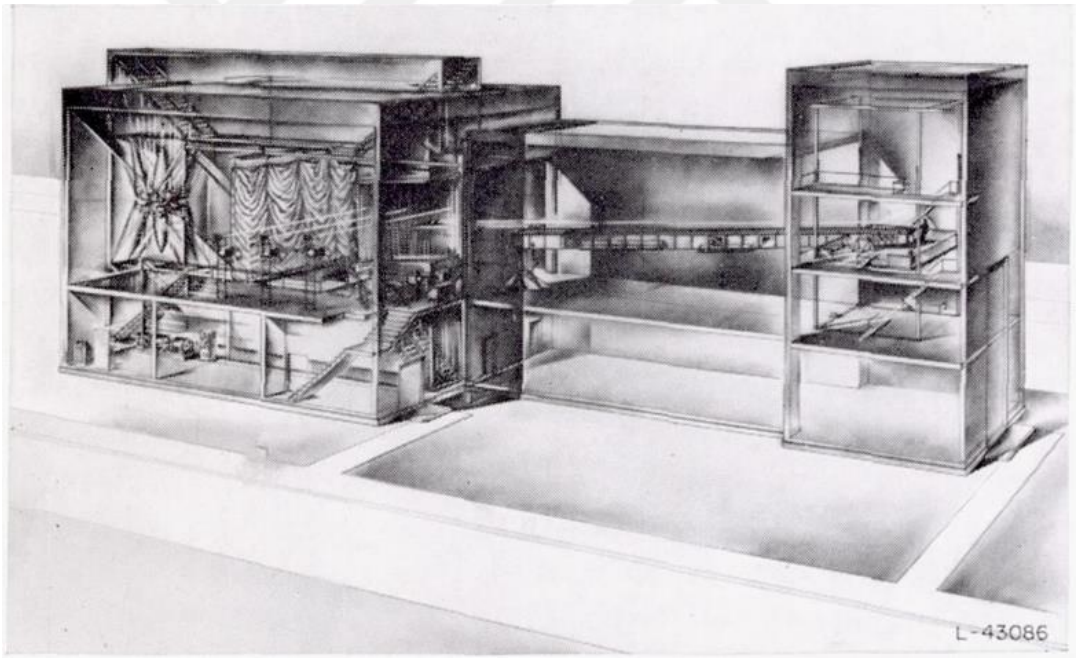


Figure 1.4: The first gust generator facility at Langley NASA, 1945

There are more primitive systems called gust generators which are available to generate two-dimensional gust profiles in the test section. Pioneering work to generate a gust in a wind tunnel is used by NASA (see Figure 1.4). A model plane

was driven into stable flight in calm air using a catapult before traveling through a transverse gust zone. A blower created the gust area, which could be modified in size, shape, and strength. A set of curtains then detained the model. Until the mid-1950s, this facility did ground-breaking work in the field (Donely, 1950). This facility produced experimental data on discrete sharp edge gusts on aircraft bodies, which could be compared to aircraft field observations. Those systems have two or more wings that are placed at the inlet of the wind and controlled by independent motors. Later on, the method of generating gust flow in a wind tunnel is changed to having an oscillating upstream airfoil. These airfoils deflect the flow away from the unaffected path, effectively changing the angle of attack of the model under test. With their changes to its Transonic Dynamics Tunnel, NASA Langley was once again one of the first in the field. As shown in Figure 1.5, a pair of synchronized vanes were mounted upstream of the test section in the contraction. In the test section, these vanes provided a sinusoidal oscillating airflow to examine the behavior of aircraft models flying on a suspension cable system (Wilmer, 1981). Many investigations on aero-elasticity were conducted at this facility, including a verification study that compared wind tunnel measurements of a scaled B-52 aircraft model to flight testing of non-dimensional wing bending in response to gusts. The results of this investigation demonstrated that wind tunnel tests, flight tests, and analytical predictions were all in good agreement.

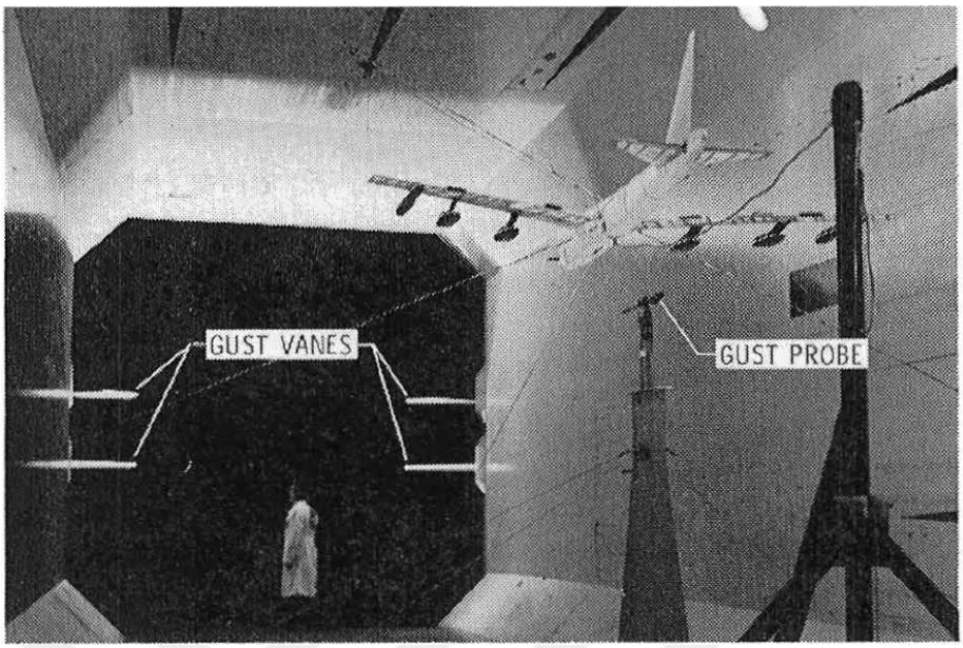


Figure 1.5: The Transonic Dynamics Tunnel at Langely with the gust vanes installed upstream of a scaled B-52 aircraft model

From the past to nowadays, artificial gust-generating systems became essential for the studies in which the unsteady response of lift-producing surfaces is of interest. Their practical use in a wide variety of wind tunnels has made them popular among the researchers who are interested in the gust response of wind turbines, helicopters, micro-air vehicles, and aircraft (Wei et al., 2019, Yigili et al. 2022) and have caused institutions to design their gust generating systems that can be employed in conventional wind tunnels, water channels or towing tanks (Jones and Cetiner, 2020). Today, gust generators are capable of generating gusts with different profiles and magnitudes (Yigili et al. 2021). They are usually composed of oscillating vanes, the number of which varies depending on the size of the wind tunnel and the intended gust uniformity in the test section (Lancelot et al., 2015). Oscillation of the vanes changes the flow direction in the test section as a result of the synthesis of two flows, i.e., the main flow of the wind tunnel and the flow induced by the oscillating vanes in the transversal direction. Different gust profiles can be obtained by varying the maximum deflection angle of the vanes and the frequency at which the vanes oscillate (Buell, 1969). A non-dimensional definition of the frequency of the

oscillating airfoils is defined as called reduced frequency by Leishman (2006). It is stated as follows:

$$k = \pi \frac{fc}{U_\infty},$$

where f is the frequency of the oscillating airfoils in terms of Hertz, c represents the chord length of the airfoil and U_∞ is the free-stream velocity. This non-dimensional constant is an important parameter and is commonly used in flapping wing aerodynamics. It is basically used to characterize the degree of the unsteadiness of the problem. Since the gust generation in a wind tunnel can be an unsteady phenomenon, the effect of the reduced frequency parameter on the gust characteristics becomes a question for the researchers. An example of the effect of the reduced frequency of the gust generator from the Delft University of Technology is in Figure 1.6. It is seen that the gust angle increases as increasing reduced frequency at higher maximum deflection angles of the gust generator. A list of details of upstream oscillating airfoil vane-type gust generators in the literature is shown in Table 1.1 and Table 1.2. While the number of vanes is varied from 2 to 9 for different gust generators, the maximum angle of attack of the airfoils is changed from 12° to 20°. The maximum reduced frequency ranged from 0.07 to 0.50.

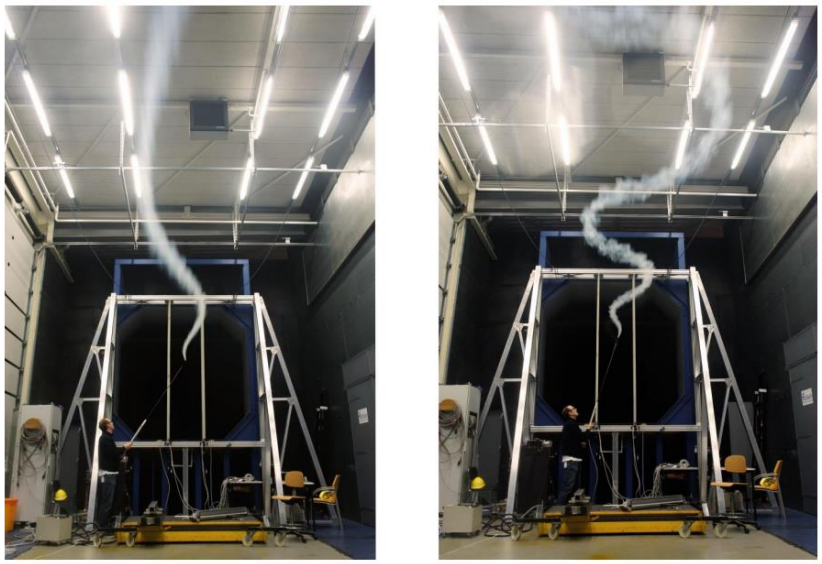


Figure 1.6: Flow visualization experiments of the gust generator system at different reduced frequency values from Delft University of Technology (Lancelot et.al. 2015)

Table 1.1: Details of the Gust Generator Setup in the literature [I]

Publication	**Vane Type**	**# of Vanes**	**Chord Length [m]**	**Drive Equipment**
Buel (1969)	NACA 0015	6	0.146	Induction motor
Simmons (1971)	NACA 0012	2	0.165	Servo-motor
Saddington (2015)	NACA 0015	6	0.114	Stepper motor
Lancelot (2015)	NACA 0014	2	0.300	Servo-motor
Wood (2017)	NACA 0012	2	0.030	Servo-motor
Wester (2022)	Flat Plate	9	0.090	Stepper motor
	NACA 0018	6	0.071	Stepper motor
	NACA 0009	2	0.180	Stepper motor

Table 1.2: Details of the Gust Generator Setup in the literature [II]

Publication	**Maximum Angle of Attack** °	**Maximum reduced frequency**	**Measurement Method**	**Location**
Buel (1969)	16.0	0.15	Hot-wire anemometry	N/A
Simmons (1971)	13.2	0.50	Pressure Transducer	N/A
Saddington (2015)	12.0	0.07	Hot-wire anemometry	7c
Lancelot (2015)	10.0	0.19	Hot-wire anemometry	4.6c
Wood (2017)	20.0	0.33	4-hole probe	45.9c
Wester (2022)	20.0	0.15	PIV and X-wire	9c
	20.0	0.15	PIV and X-wire	9c
	20.0	0.15	PIV and X-wire	9c

1.1.3 Overview of Active Grids

Investigation of the turbulent flow which has a complex character can be started with the homogeneous isotropic turbulence (HIT) which is the simplest state of a complex flow regime. Wind tunnel turbulence created by a grid comes closest to the ideal condition of homogenous isotropic turbulence (Mydlarski, 2017). When put at a sufficient distance in the flow direction (with $x/M \geq 20$ - 30, M the mesh size), this mesh structure consisting of horizontal and vertical bars placed before the

contraction cone in wind tunnels assures a flow with an approximately uniform and isotropic turbulent character (Isaza et al., 2014). In cases where the mesh size (M) used is considerably smaller than the wind tunnel width (W), it has been observed that the turbulent flow character is homogeneous in the regions far from the wall effects and the degree of isotropy is quite high ($u_{rms} \,/\, v_{rms} \approx 1.1$) (Mydlarski, 2017). However, the Reynolds number based on Taylor's microscale, R_λ, is limited, in this way for the grid-generated turbulence (Cekli 2011). On the other hand, having a high Reynolds number is very important for studying and dealing with fundamental investigations of turbulent flows. The ratio between the largest and the smallest length scales of a turbulent flow is described as follows:

$$\frac{L}{\eta} = Re^{3/4}$$

As seen above, to obtain a turbulence spectrum in which the largest (L, integral length scale) and the smallest scales (η, Kolmogorov length scale) are distinctly separated from each other, high Reynolds numbers are needed. The Re_λ obtained under laboratory conditions is of the order of 10^3 and its equivalent in the Reynolds number (Re) defined according to the integral scale is of the order of 10^5 (Warhaft, 2009). Studies with high Re_λ numbers are needed to experimentally examine the connection between the discontinuous structure in a turbulent flow and anisotropy at small scales and to check whether the local isotropy in small structures specified in Kolmogorov's postulate is achieved at high Reynolds numbers (Warhaft, 2009). In experimental studies performed in wind tunnels, the Re_λ number can be increased by increasing the tunnel size or the average tunnel velocity, but this is often a very difficult and expensive method (Cekli et al. 2011). One of the most known studies on this subject was performed in the world's largest wind tunnel which has a 24 x 36 m^2 test section at the NASA Ames Research Center. The obtained Reynolds number (Re_λ) even in the boundary layer that occurred in the tunnel is around 1450 (Saddoughi ve Veeravalli, 1994).

To increase the turbulence level in wind tunnel experiments and similar flow conditions, some different active methods have been tried in addition to the use of a passive method mentioned above (Cekli, 2011). Grids with oscillating agitator bars or grids with attached jets (Ling and Wan, 1972; Srdic et al., 1996; Thompson and Turner, 1975), jet flow as tip injection (Gad-El-Hak ve Corrsin, 1974; Thole et al., 1994) and usage of a series of fans in the tunnel (Ozono et al., 2006) are some of the methods tried to generate such flows. But, it is quite difficult to obtain the desired fully developed turbulence characteristics with these methods, and especially the applications of the last two methods in the tunnel are very difficult. As an alternative to the methods mentioned above, Makita (1991) designed the active grid system to be able to reach the higher turbulence levels in a small-scale wind tunnel. In the related study, in a tunnel with a test section cross-sectional area of 0.7 × 0.7 m^2, a test section length of 6 m, and a very low turbulence density under normal conditions ($u' / U_0 \approx 0.04\%$, u' means the square root of velocity fluctuations and U_0 is the average tunnel velocity). The active grid seen in Figure 1.8 is placed at the entrance of the test section. Originally working in the biplane, this grid consists of 7 horizontals and 8 vertical bars in total and a large number of flaps or winglets attached to these bars. As can be seen in the figure, the mesh size (M) of the grid structure is 46.7 mm and each bar is controlled by a different motor. The winglets have a random motion to generate a turbulent flow which will be affected by the wake regions of the rods on the grid and the flow separations that occurred on the leading and trailing edges of the winglets. The turbulent characteristics of the flow are measured by an X-type hotwire. As a result, a turbulence density of more than 16% was obtained 50 mesh size downstream of the grid (x/M = 50) using the active grid, and the order of Re_λ=390 was reached at a free flow velocity of 5 m/s in a relatively small wind tunnel. The measured longitudinal integral length scale is approximately 200 mm, and all these flow properties are equivalent to the turbulent flow properties produced by a passive grid with a Reynolds number Re_M of the order of 10^6 defined by the mesh size (Makita, 1991). It can be seen that a turbulent flow,

which requires the use of a much larger scale wind tunnel, can be produced in a small-scale wind tunnel and at low speeds thanks to the active grid.

The turbulent flow obtained in this study differs from the ideal case in a way that it shows an undeniable level of anisotropy. To remove this anisotropy three different methods are tried. Comte-Bellot and Corrsin (1966) passed the flow driven by the grid through the second cone of contraction before entering the test section, Larssen and Devenport (2011) placed the active grid at a point within the cone of contraction and Poorte and Biesheuvel (2002) changed the angles of the flaps located on the same rod. In this study, each adjacent flap on the same rod was placed perpendicular to the other as seen in Figure 1.9 and it was observed that the anisotropy decreased. However, in this case, the turbulence intensity and Reynolds number produced decreased compared to the previous studies.

In addition, to generate homogeneous isotropic turbulent flow with high Reynolds, active grids are also used to generate turbulent atmospheric boundary layers. As it is known, to create a turbulent atmospheric boundary layer in wind tunnels, a long test chamber and passive elements such as roughness elements, barriers, mixing elements, and mesh structures placed in an upstream position according to the test model are needed (Armitt and Counihan, 1967; Counihan, 1973; Cook, 1973; Cook, 1978, Irwin, 1981). Cekli and van de Water (2010) succeeded in forming the atmospheric boundary layer in a wind tunnel with a test section cross-sectional area of $0.7 \times 1.0\ m^2$, without the need for passive elements, using an active grid Even if an active grid may be used to generate a velocity profile of the atmospheric boundary layer in a wind tunnel, additional research is needed to acquire the fluctuation profiles in the atmospheric boundary layer Cekli (2011). Controlling the angles of the flaps on the active grid and designing probability density functions for these angles can produce the very turbulent and discontinuous flow pattern seen in atmospheric turbulence and these events are described as gusts which are the essential consequence of turbulent wind flows by Knebel et al. (2011). This discontinuous behavior observed in atmospheric turbulent flows cannot be modeled realistically in the turbulent flows generated in the wind tunnel experiments. In wind

tunnels, the mean flow velocity is generally constant, which is not the case in atmospheric flows. As a result, when studying the effects of atmospheric flows in wind tunnel studies, it's critical to mimic powerful gusts as well as produce a realistic atmospheric flow profile and active grid systems can be used to generate gust flows in the wind tunnels. There are some studies who used the active grids to generate gust in the wind tunnels in the literature.

Quinn et al. (2017) used the active turbulence grid to generate stream-wise gust in the test section by adjusting the vertical vanes at a constant angle and varying the horizontal vanes around a fixed angle to investigate the effect of the gust on micro air vehicles. Traphan et al. (2018) demonstrated that the active grid generating sinusoidal gusts for the experiments resulted in extremely three-dimensional flows and that the relative strengths of the gusts did not remain constant across the range of reduced frequencies investigated. Wei et al. (2019) studied the effect of increasing reduced frequency and increasing the angle of attack on the gust characteristics using an active grid. It is pointed out that at a higher angle of attack of the gust vanes, dynamic-stall phenomena become significant and need to be studied in detail in future studies. Neuhaus et al. (2021) could generate periodic sinusoidal velocity variations, velocity steps, and single gusts in the wind tunnel using an active turbulence grid by defining a transfer function which is defined by the relation between the blockage ratio of the grid and the corresponding velocity. Wester et al. (2022) described a path for designing a 2D active grid for dynamic flow modulation in wind tunnels and stated that by using aerodynamically shaped shafts, the flow quality can be improved in wind tunnels with a 2D active grid.

In general, active grid design parameters can be listed under four main headings, namely, the orientation of the flaps on the rotating bars, flap geometry, number of the flaps, and the blockage ratio. For the first of these, the orientation of the flaps, two basic orientation types stand out in the studies conducted in the literature. In the planar orientation, which is the first orientation type, all the flaps are connected on the same plane on the rod to which they are attached. The disadvantage of this

orientation is that the anisotropy in the turbulent flow produced is high ($u_{rms}/v_{rms}$of the order of about 1.2) (Makita 1991, Makita and Sassa 1991, Mydlarski & Warhaft 1996). In the study by Poorte and Biesheuvel (2002), it was observed that the placement of the flaps in the active grid has a significant effect on the isotropy ratio. In this study, each adjacent fin on the same rod was placed perpendicular to the other and it was observed that the anisotropy decreased. However, in this case, the turbulence intensity and Reynolds number produced decreased compared to the previous studies. Finally, a system in which the placement angle of the flaps on the same rod is increased sequentially and the angle between the flap at the beginning of the rod and the flap at the end of the rod is adjusted to be perpendicular to each other has been proposed, but such an application has not been found (Roadman and Mohseni, 2009).

It is seen that the flap geometry is mostly triangular (or diamond type), when the literature studies are examined. However, some researchers have drilled a certain number of circular holes on these triangular flaps to increase the homogeneity of the flow and reduce the inertia of the flap to make it easier to rotate. Thormann and Meneveau (2014), the first of two main studies on this subject, studied the effect of fractal geometry flaps on the flow of four different flaps. The four-wing types studied here are respectively "Sierpinski triangles", space-filling squares, "Apollonian packing" fractals (i.e. decreasing diameter), and non-fractal (solid) wings. The second study on the effect of flap geometry on flow was done by Hearst and Lavoie (2015). In this study, three types of flap structures perforated triangle, solid triangular, and solid semi-circular blades were investigated. Hearst and Lavoie (2015) found that different flap shapes produce flows with different turbulence intensities for the same grid bar rotational speeds. It is concluded that solid triangular flaps can produce the highest turbulence intensity. In addition, it was concluded that the flap shape did not have a significant effect on isotropy and integral length scale.

It is observed that active grid mesh length is determined as the lowest 3.75 cm (Poorte and Biesheuvel, 2002) and the highest 21 cm (Larssen and Devenport, 2011), when the mesh dimensions of the active grids in the literature are examined. The

number of meshes starts from 6 x 8 (Kang et al. 2003) to 20 x 20 (Michioka et al. 2011) in the studies in the literature. Since the main purpose in active grid systems is usually to reach the highest Reynolds number that can be reached in the wind tunnels with small test sections, M, which is expressed as mesh length, is tried to be chosen as large as possible. However, as the diagonal length of the mesh M increases, the integral length scale ℓ, increases, and the ratio of the tunnel section edge length to the integral length scale W/ℓ decreases. This occasion reduces the homogeneity of the flow behind the active grid. Considering that producing homogeneous isotropic and turbulent flow is one of the main purposes of active grid systems, it is concluded that it is not necessary to increase the diagonal length of the blades redundantly. As a result, when designing active grid systems, it is necessary to maintain a balance between high Reynolds number and flow homogeneity.

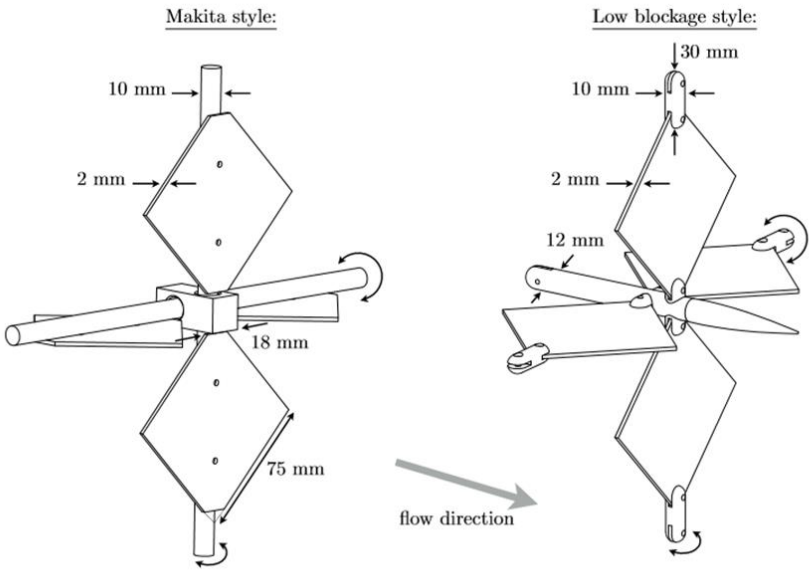


Figure 1.7: Makita-style (left) and low-blockage (right) flap designs designed for the University of Oldenburg active grid system (Reinke et al., 2017)

When all the flaps are open in the active grid systems, the highest flow speed and the lowest turbulence intensity are achieved. Knebel et al. (2011) found the turbulence

intensity to be around 5% in measurements made at 1.32 m downstream from the active grid. In other words, a higher flow speed and lower turbulence intensity cannot be achieved if the minimum blockage ratio (with all blades in the open position), caused by active grid systems at the tunnel entrance, is not reduced. To reduce this blockage ratio, Reinke et al. (2017) proposed a flap coupling system that produces a low blockage rate. With this setup, the blockage ratio of the Makita style active grids, which have an average minimum blocking ratio of 19.7%, can be reduced to around 6%, and thus the maximum turbulence intensity in the flow behind the active grid can be reduced to 1.7%. In this way, it was ensured that the active grid could also produce lower turbulence intensities.

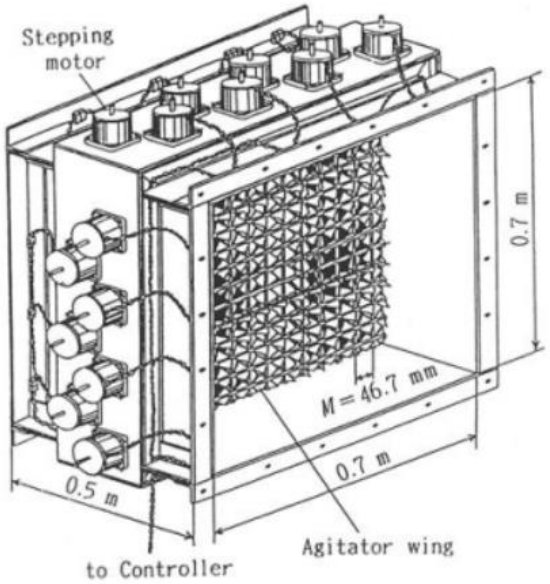


Figure 1.8: Active Grid drawing designed by Makita (Makita and Sassa 1991)

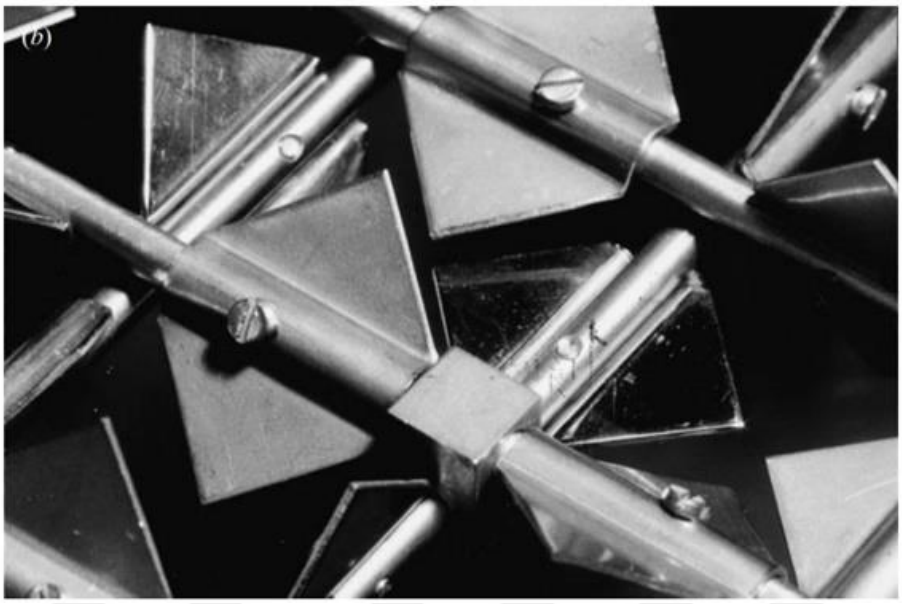


Figure 1.9: Active grid application consisting of adjacent flaps placed perpendicular to each other

General information on wind tunnels in which active grid systems are used in the literature is presented in the Table 1.3. Sytsma and Ukeiley (2013) used an active grid system controlled by stepper motors in a suction-type wind tunnel with a cross-section of 1 m x 1 m and a test section length of 3 m, with a turbulence intensity ranging from 12% to 30% and an isotropy ratio ranging from 1-1.3%. They have succeeded in producing turbulent flows with the maximum length scale they have achieved of the order of 0.25 m. Due to the limited length of the test section, measurements were carried out at a maximum distance of 20M (M stands for grid mesh size).

Table 1.3: Wind Tunnel test section areas and background freestream turbulence intensity values in the literature where active grids are used

Reference	**Wind Tunnel type**	**Free stream Turbulence Intensity**	**Test Section [m^2]**
Makita and Sassa (1991)	Blowing, open loop	<0.04 %	0.70 × 0.70
Mydlarski and Warhaft (1996)	Blowing, open loop, vertical	N/A	0.40 × 0.40
Kang and Meneveau (2008)	Closed loop	N/A	1.22 × 0.91
Hearst and Lavoie (2015)	Closed loop	<0.06 %	1.20 × 0.80
Cekli and van de Water (2010)	Closed loop	N/A	1.00 × 0.70
Larssen & Devenport (2011)	Closed loop	<0.5 %	1.8 × 1.8
Sytsma and Ukeiley (2011)	Suction, Closed loop	<0.22 %	1.03 × 1.03
Kröger et al. (2018)	Closed loop, open and closed test section	N/A	3 × 3

1.2 Objectives and Thesis Layout

The goal of this research is to design and integrate an active grid system into an open-loop suction-type wind tunnel and investigate the gust flow characteristics of the flow field of the near wake of the active grid using experiments. To investigate the gust characteristics, the flow field of the near wake region of the two-vane gust generator under oscillatory sinusoidal motion at various phase angles is examined using the particle image velocimetry method. Gust generator device is designed and integrated into a tunnel as a preliminary study of an active grid system design for METU RÜZGEM which is supported by the Scientific and Technological Research Council of Turkey (TÜBITAK) under a project named "Design and application of an integrated wind tunnel-active grid system to generate highly turbulent and gusty flows in wind tunnel tests". To investigate the gusty flows, the vanes of the gust generator oscillate at varying frequencies and phase angles. Two vanes oscillated with and without a 180° phase angle difference for varying reduced frequencies and varying amplitudes. The first chapter provides an overview of the literature on gust generators and active grids. The second chapter will detail the design process of the gust generator and active grid, as well as experimental setup and measurement methodologies, and the third chapter will present the findings of the study. Finally, in the fourth chapter, there will be a discussion and suggestions will be provided for future works.

CHAPTER 2

EXPERIMENTAL SETUP AND MEASUREMENT METHODS

2.1 Active Grid Design

In this section, an active grid is designed to generate gust in RÜZGEM C3 wind tunnel. The design process of the active grid is explained after wind tunnel facility is introduced. Motor sizing process of the active grid and motion controller architecture is mentioned at the end.

2.1.1 Wind Tunnel

The wind tunnel to be used for the active grid is an open circuit suction-type wind tunnel with a 1.0 m × 1.0 m closed test section cross-sectional area and a length of 8 m (Figure 2.1). It consists of a settling chamber section, a contraction with a contraction ratio of 1:5, and a transparent test section with Plexi-glass walls. It is powered by a 45 – kW speed-controlled electrical motor and it drives a 1.2 m diameter axial fan. To ensure optimum flow quality inside the test section, the settling chamber includes a honeycomb and a screen. The maximum test section freestream flow velocity that can be reached in the empty tunnel is about 25 m/s, and the average inlet turbulence intensity level is around 0.35%.



Figure 2.1: RÜZGEM C3 open-loop suction type wind tunnel

2.1.2 Conceptual Design of the Active Grid Frame

First of all, a conceptual design of the active grid system is carried out. After conceptual design is done, a more detailed design is carried out. The active grid design is considered as a classical Makita style grid. Mydlarski (2017) stated that M=W/10 (W stands for test section width) ratio is the basic rule for choosing the number of flaps for cases where the homogeneity level of the flow is critical in homogeneous isotropic turbulent flows in Makita type active grid applications. In this context, a total of 20 bars, 10 horizontal and 10 vertical, for the wind tunnel with a 1.0 × 1.0 m^2 closed test section cross-sectional area, where the active grid system of the project will be integrated, and 20 motors and 20 motor drivers that will enable each bar to be controlled independently. As the flap geometry, diamond-type solid surface flaps were chosen, which have been shown to work smoothly in the applications made so far. In the first stage, a rough concept design was made, and nine full and two half flaps at the beginning and end of the rigid bar were placed on the rigid bar. These bars will be mounted to an outer frame.

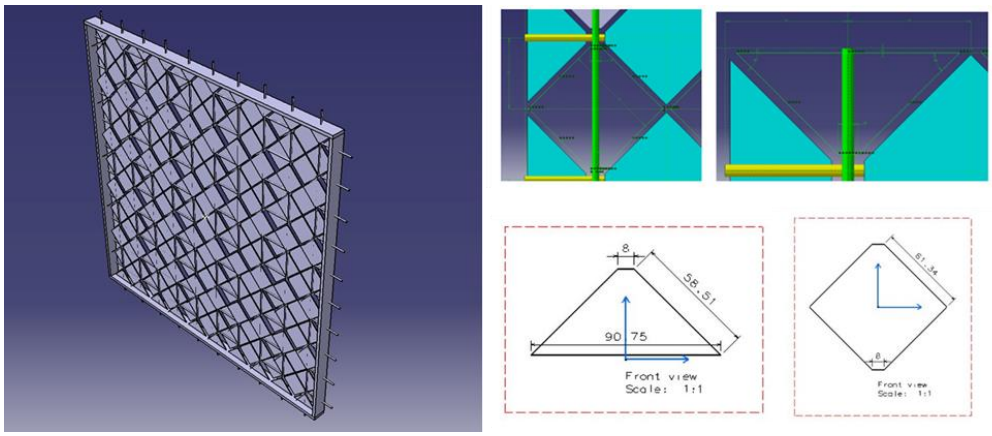


Figure 2.2: Preliminary conceptual design of the Active Grid

Three different active grid frame design is considered (Figure 2.3). Considering the lower budget of the last design with sigma profiles structure is chosen. In the active grid outer frame design (Figure 2.3 (c)), the construction of the chassis from aluminum sigma profiles and aluminum plates is based on placing a wheeled carrier structure, which will also consist of sigma profiles, under the chassis. Sigma profiles are fixed to the flanges of the tunnel on the constriction cone side and the aluminum profiles on the test section side with bolts. In this design, the frame structure of the chassis is formed from 6-channel aluminum sigma profiles with 45 mm x 45 mm cross-section dimensions. The inner surfaces of the active grid system are 15 mm thick 5000 or 6000 series aluminum plates. These two aluminum series are both suitable for laser cutter machinability and strength.

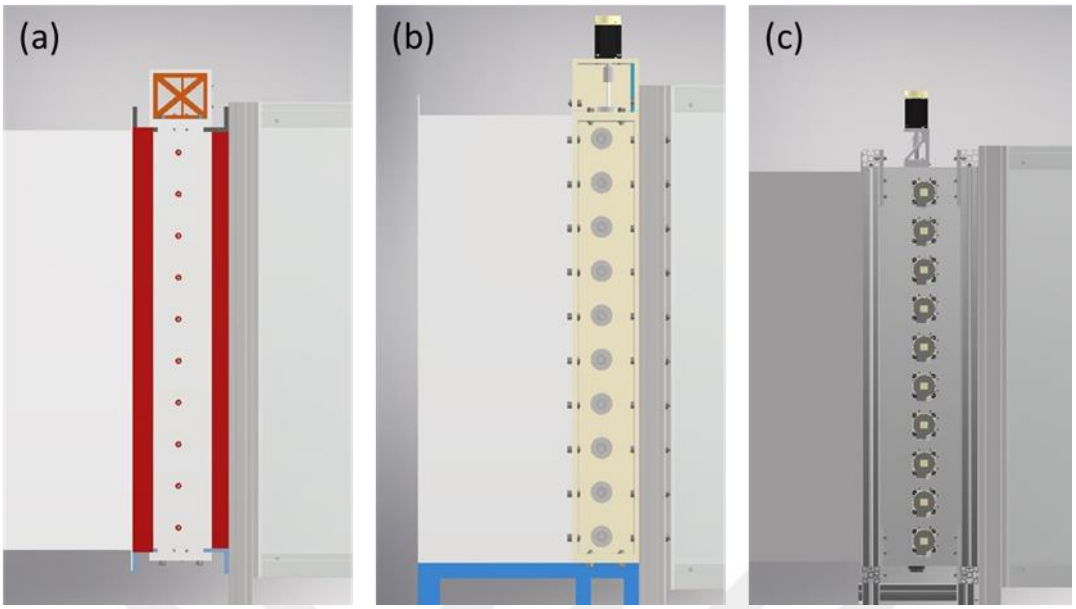


Figure 2.3: Active grid system chassis designs: (a) Initial design based on the slide system; (b) the second design connected to the fixed cross-section duct; (c) final design with frame of sigma profiles

As explained in the conceptual design section, it was decided to create a 10 × 10 mesh grid structure within the tunnel test section. Two parameters were particularly effective in determining the properties of the flaps to fit into these meshes and the rods to carry these flaps:

- Blockage rate created by the active grid: It is aimed that the tunnel blockage that will occur when the active grid blades are fully open, is as small as possible and that the blockage that will occur in the fully closed state is as large as possible. In this way, it will be possible to produce turbulent and higher magnitude torrential flows with higher turbulence intensity.
- Withstand aerodynamic loads during operation: The flaps and flap bars must undergo minimal deformation during operation.

The minimum blockage created by the active grid is determined by the cross-sectional area of the flap bars and the thickness of the blades and half blades. On the other hand, the surface area of the flaps and the cross-sectional area of the bars are

decisive for the largest blockage to occur. In addition to these, to prevent deformation and vibration-induced contact during the operation, it was found appropriate to leave a 3 mm gap between the flap edges and the bars, and a 3 mm gap between the edges of the half flaps and the side surfaces (Figure 2.4). The distance between the vertical and horizontal bars was determined as 10 mm (Figure 2.5).

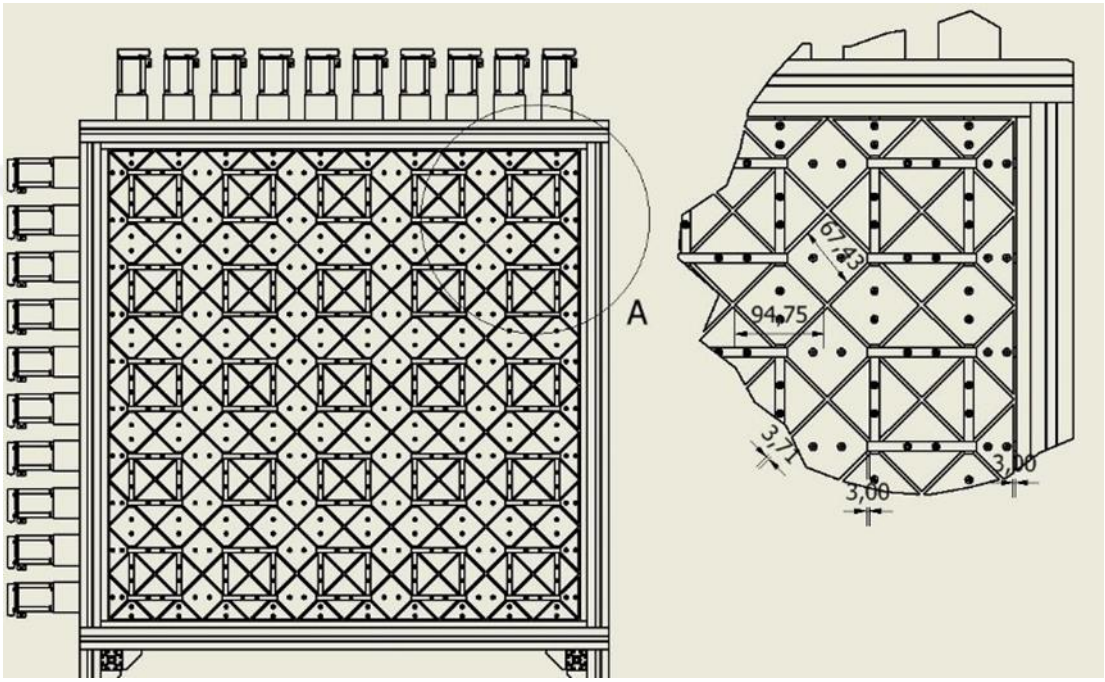


Figure 2.4: Active grid detailed design flap dimensions and clearance amounts

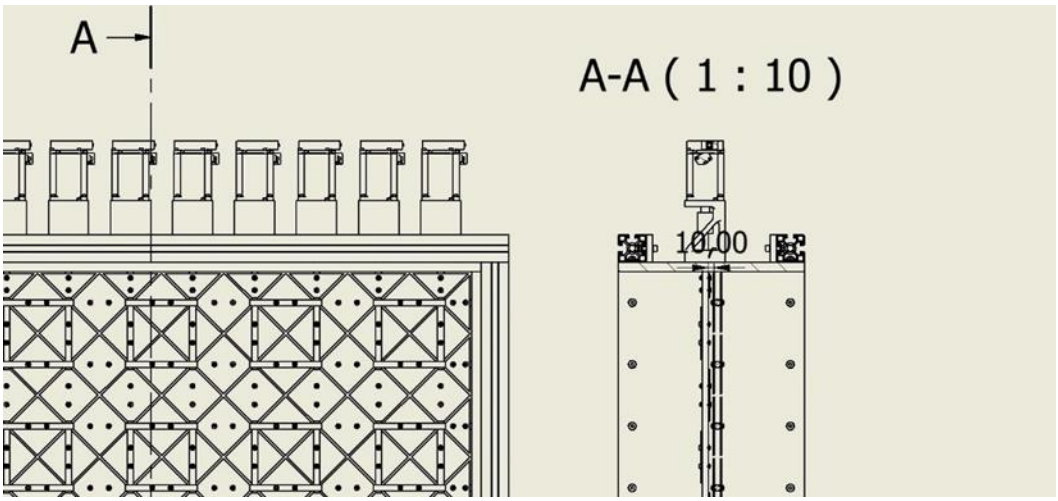


Figure 2.5: Active grid detailed design placement of horizontal and vertical bars

The minimum blockage (when all flaps are open) is 21% and the maximum blockage (when all blades are closed) is 89%, as a result of flap and rod sizing studies. The minimum and maximum blockage levels that can be achieved in the Oldenburg University active grid system (Reinke et al., 2017), which is one of the applications referenced in the project, are 21% and 92%. As can be seen, in this sense, values compatible with the literature have been reached.

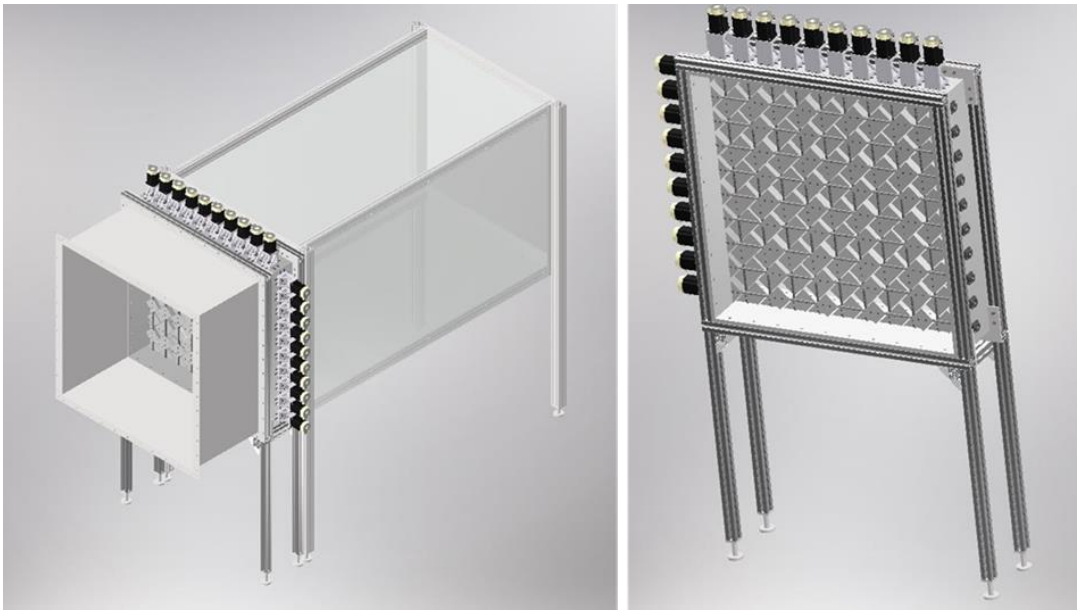


Figure 2.6: 3-D CAD sketch of the detailed design of the active grid

Table 2.1: Some important dimensions of active grid design

Rod cross-section diameter [mm]	10
Rod length dimension [mm]	1000
Material of the rod	1.2210 steel
Thickness of the flap [mm]	2
Mesh length of the flap [mm]	94.75
Material of the flap [mm]	Aluminum (5000 series)
Distance between the vertical and horizontal bars [mm]	10
Active grid outer frame length [mm]	1120
Depth of the active grid frame [mm]	300
Thickness of the aluminum plate [mm]	15
Material of the active grid frame [mm]	Aluminum (5000 series)
Dimensions of the sigma profiles [mm x mm]	45 x 45
Minimum blockage ratio [-]	%21
Maximum blockage ratio [-]	%89

2.1.3 Motor Sizing of the Active Grid

One of the most crucial elements of active grid design is motor sizing. Because high-speed rotation is required during flow, the weights on the rods carrying the flaps to which the motors are attached must be appropriately estimated, and motors with sufficient torque (continuous torque) should be chosen. The static load to which the blades are momentarily exposed, as well as the torque value required to accelerate the blades from zero, should be taken into account during this computation. First and foremost, the maximum load that the motors will be subjected to at any given time has been calculated.



$$N = \frac{1}{2}\rho U^2 2\pi \sin(\alpha) A \cos(\alpha)$$

$\tau_{max} = N * l * 10 \cong 0.195\ N.m$ $\tau_{max} = N * l * 10 \cong 0.58\ N.m$

Figure 2.7: Blade orientation and force/torque values used in the motor sizing study

While the black line shown in the figure above represents the flap, the circle in the middle represents the rod to which the flaps are attached, and the green line between the center of the force and the axis of rotation represents the moment arm. It is expected that the flow velocity of the wind tunnel can increase to a maximum of 18 m/s at maximum fan rotation speed under active grid blockage. The flat plate assumption is used to calculate the forces on the flap. To keep within the safe margin, the normal force perpendicular to the flap is derived using the lift force will be created under 1.08 kg/m3 air density at 45° angle of attack and 18 m/s flow speed. The greatest moment value that might occur with the normal force produced was computed, with the center of pressure specified as the tip of the flap. The torque obtained is multiplied by the total number of flaps, which is 10 in this case. The torque is determined to be 0.58 Nm in this example. The inertial torque of the system must also be estimated in addition to the torque value from the flow. The formula for inertia torque is provided below.

$$\tau = \sum J\,\ddot{\theta}$$

While the variable J in this formula corresponds to the moment of inertia of the system, $\ddot{\theta}$ represents the second derivative of the angular position concerning time,

in other words, the angular acceleration of the system. In this system, rods and flaps can be considered as two main components for the calculation of inertia. Rod and flap moment of inertia values were calculated using the following formulas, respectively.

$$J_{rod} = \frac{1}{8} m_{rod} d^2$$

$$J_{rod} = 10 \times \frac{1}{12} m_{rod} x^2$$

In the above equations, m_{rod} is the rod mass, d is the rod diameter, m_{flap} is the flap mass and x is the flap edge length. At this point, the rod weight is 0.75 kg and the flap weight is 0.02 kg for the case where the flaps are selected from aluminum and, the rods from 1.2210 steel material and the rod diameter is determined as 10 mm. The angular acceleration to be used when calculating the inertia torque is based on a high-frequency sine motion. Accordingly, the highest acceleration value to be reached is calculated by taking the second derivative of a time-dependent sinusoidal motion profile in the range of ±16°, whose equation is given below.

$$\theta = \bar{\theta} sin(\omega t)$$

$$\dot{\theta} = \bar{\theta} \omega cos(\omega t)$$

$$\ddot{\theta} = \bar{\theta} \omega^2 sin(\omega t)$$

The angular frequency is represented by the variable ω in the above equations, while the maximum pitching amplitude is represented by the variable $\bar{\theta}$. The acceleration value multiplied by the load inertia in the inertia torque was chosen because the term Aw^2 in the angular acceleration equation expresses the maximum acceleration value in the sinusoidal motion profile. The angular frequency value in the expression used here is known as $2\pi f$. The f value here was evaluated as 20 Hz, which is one of the highest frequency values in the literature, and converted to angular acceleration. As a result of the calculations, the maximum angular acceleration value was found to be

4405.3 m/s2. The inertia value for the rod was calculated as 9.24×10-6 kgm2, for 10 flaps the total inertia value was calculated as 9.06×10-5 kgm2, in addition to these inertia values, the engine inertia was selected as 0.277×10-4 kgm2 using the motor information used in similar applications, the total load inertia was evaluated as 10×10-5 kgm2. By multiplying the angular acceleration and load inertia values, the inertia torque of the system was calculated as 0.56 Nm.

Another parameter that is effective in motor sizing for active grids is the flap rotation frequency required to create an isotropic turbulent flow. Roadman and Mohseni (2009) showed that for an isotropic turbulent flow the dimensionless tip velocity ratio, whose equation is given below, should be close to one:

$$\lambda = \frac{Wf}{U_\infty}$$

In this equation, f is the flap rotation frequency and U is the free stream flow velocity. The aim here is to force the ratio of the length of the eddies to the width of the tunnel to be one. For example, in the calculation made using 18 m/s, which is the highest speed that the wind tunnel to be used in this study (RUZGEM C3) can reach, and 1.0 m, which is the width of the test section, the necessity for the flap rotation frequency to reach 18 Hz emerges.

As a result of the market research, it has been seen that the servo motors in the market, which may be sufficient for this application, have rated output powers of 200 W, and 400 W, and these output powers correspond to continuous torque values of 0.64 and 1.27 Nm, respectively. In addition to the torque calculation made at the beginning, it was concluded that servo motors with a nominal torque of 1.27 Nm would be sufficient for an active grid application of this size to stay on the safe side, considering the relatively small frictions caused by parts such as bearings and couplings.

2.1.4 Motion Controller Architecture Design

Since the automatic control system with fixed velocity and fixed Reynolds number options of the RUZGEM C3 wind tunnel is built by a LabVIEW code and National Instruments (NI) CompactRIO controller hardware, the motion controller system of the servo motors of the active grid is decided to be the NI cRIO-9047. The controller supports the EtherCAT communication protocol. The EtherCAT communication protocol is based on the "Ethernet on the fly" principle, which is an important factor for fast cycle times in industrial automation applications. Hence, it has been decided to use the EtherCAT communication protocol as the communication protocol of the servo motors that drive their systems in the gust generator system and the active grid. The EtherCAT communication protocol was chosen because it is intended to operate 20 motors at very high rates and simultaneously, which necessitates data transfer at a very high speed. In this protocol, the cRIO-9047 controller is used as a master, while the servo drives are treated as a slave. The process data (Process Data Objects, PDOs) sent by an EtherCAT slave during each cycle are user data that the application expects to be updated cyclically or that is supplied to the slave. To do this, the EtherCAT master (cRIO-9047) defines which process data (size in bits/bytes, source location, transmission type) it wishes to send to or from each EtherCAT slave during the initial stage.

The main servo motor motion protocol used for the active grid characterization is sinusoidal motion at a constant frequency with a fixed amplitude. To do that, certain frequency and amplitude values are defined initially in the flowchart of the active grid control software illustrated in Figure 2.8. Then, position information was sent to both motor drivers as a separate command in a real-time loop updated every 2 milliseconds, and it was operated in position control mode. As input to the sinusoidal function used in this loop, frequency information can be defined in Hz and maximum amplitude information in degrees. Again, within the same loop, to be able to obtain data under phase-locked PIV, at certain angles, the 5 Volt Transistor-Transistor Logic (TTL) signal is applied to the Digital Input/Output module attached to the

cRIO controller as phase triggering, and therefore to the PIV laser, so that the flow field is captured only when the motors are at a certain angle.

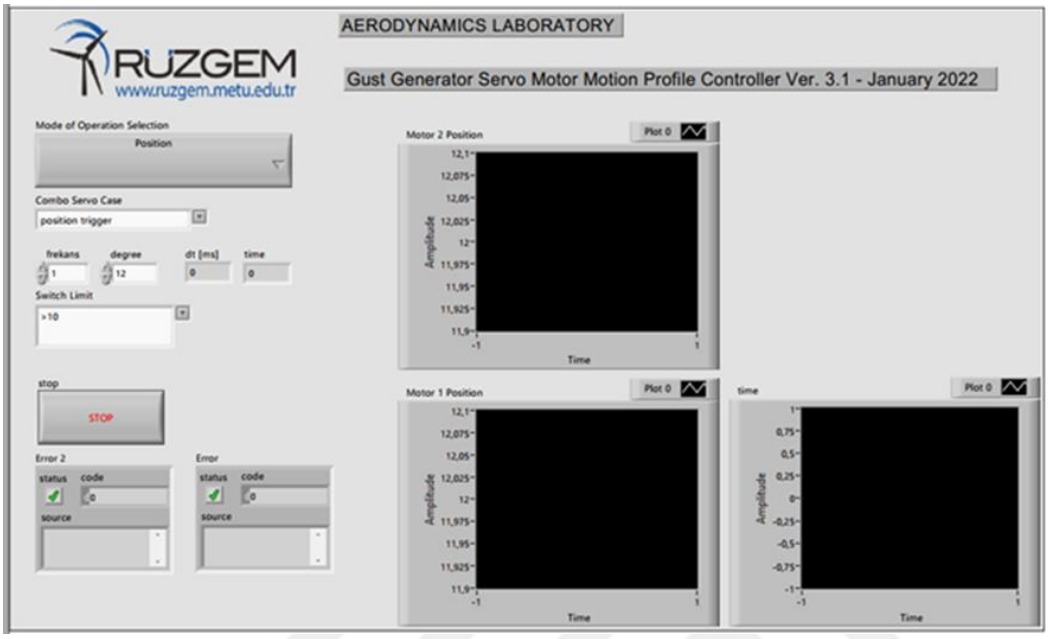


Figure 2.8: Servo motor motion controller GUI for the active grid written in LABVIEW software

The active grid motor control system was used to ensure sinusoidal pitching motions of 10 Hz and 12° amplitudes of the two blades as a baseline case, and the position information obtained from the motor encoders was used to compare how well the motors followed the given motion kinematics with the analytical equation for the in-phase case. Servo motors, as seen in Figure 2.9, accurately follow the set position kinematics. The amount of error was found to be less than 1% of the entire amplitude when compared to the analytical function.

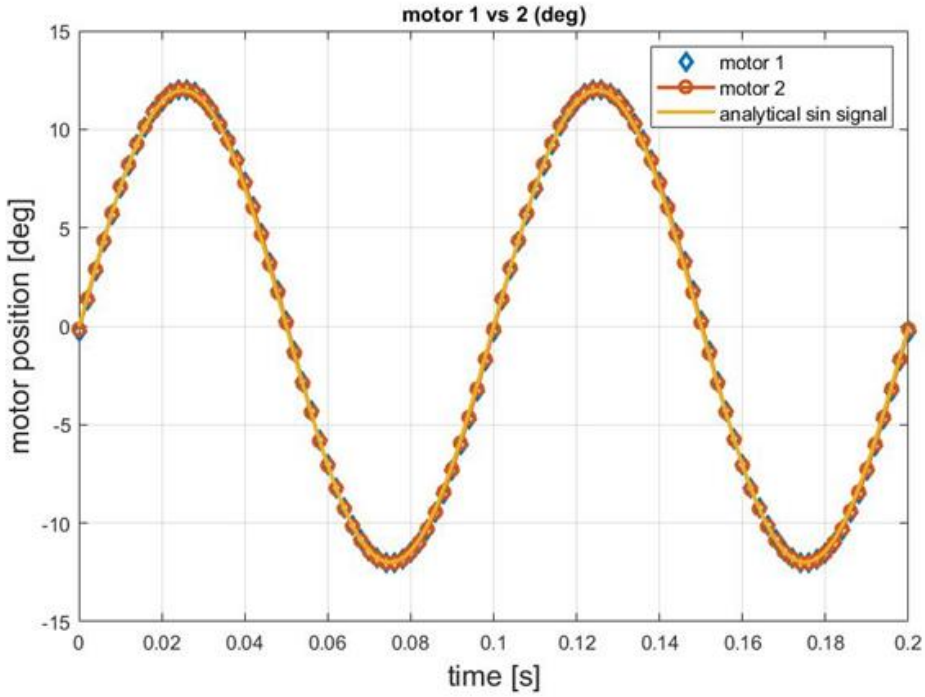


Figure 2.9: Variation of the position information received from the motors performing a sinusoidal pitching motion with a frequency of 10 Hz and an amplitude of 12° for 2 periods

2.2 2D Active Grid System

2D two-wing active grid or a gust generator is used to examine the effect of the gust produced by the flapping wing on the wake region in a smaller wind tunnel (RÜZGEM C1) as a preliminary study for the 3-D active grid in RÜZGEM C3 wind tunnel.

2.2.1 Wind Tunnel and Gust Generator

Gust generator measurements are carried out in an open-circuit suction type RÜZGEM C1 wind tunnel. Figure 2.10 depicts the tunnel's schematics. Before reaching the test section, the incoming airflow travels through a honeycomb, a screen, and a 1.0-meter long settling chamber, before entering a 9:1 contraction. The

turbulence-generator-grids are mounted at the front section of the test section, which is built of 10mm thick transparent Plexiglas with dimensions of 340 x 340 x 1000 mm^3. The flow is then diffused through a diffuser that is 2.0 meters long. To avoid an undesirable pressure gradient, the divergence angle is 2.43°. To attach to the fan case, a 1.7 m long adapter turns the square cross-section into a circular one. The fan is powered by a 4.0 kW electric motor. A fan and a 4 kW electric motor drive the flow in the wind tunnel. The flow speed is determined by the Pitot-static tube placed at the end of the constriction cone. The two-dimensional gust generator is mounted in between the end of the contraction cone and the entrance to the test section. The details of the gust generator design will be explained in the next chapter.

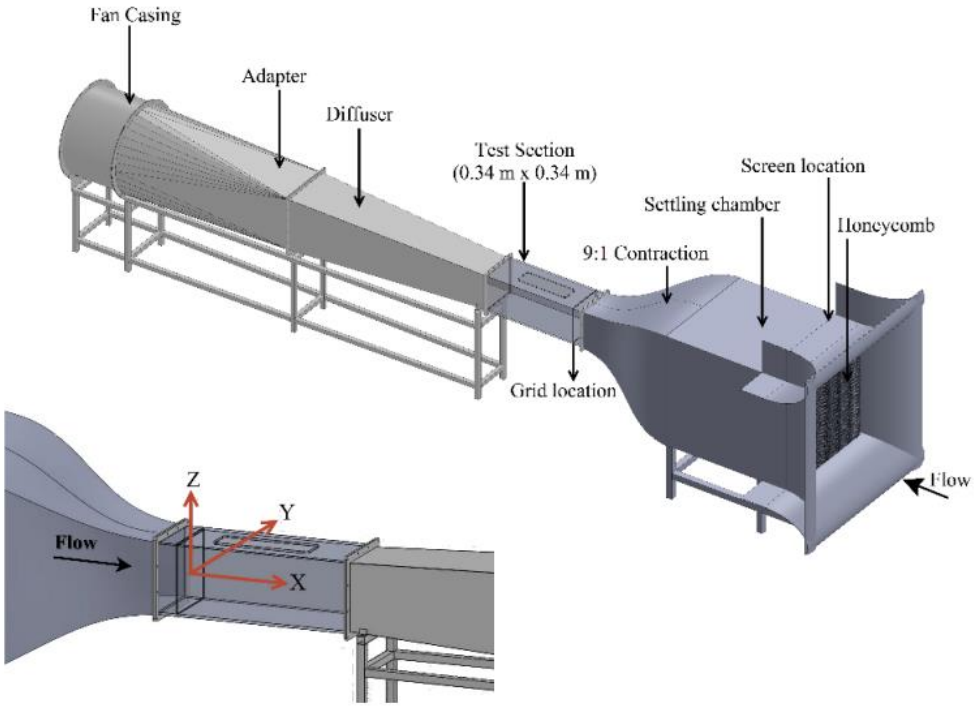


Figure 2.10: RUZGEM C1 open-loop wind tunnel's schematics and coordinate system.

The gust generator consists of two separate blades with NACA0015 airfoil, 80 mm chord length, and 330 mm wingspan. Blades are 3D printed using PLA+ material. The two blades are independently driven by two servo motors with 400 W power

and 1.27 Nm nominal torque. The nominal speed of the servo motor is 3000 rpm. The details of the motor selection process will be explained under the active grid design section. The distance between the blades is adjustable from one to three-chord, allowing for the creation of a variety of gust flows. In this study, the distance between two vanes is selected as one chord length of the airfoil to be able to replicate the case in 3D active grid. The blockage ratio is the main limitation for the gust generator considering the small dimension of the tunnel test section. Considering the two vanes at the maximum angle of attack of the vanes at 16° causes a 12% blockage ratio number of the vanes is limited to two vanes.

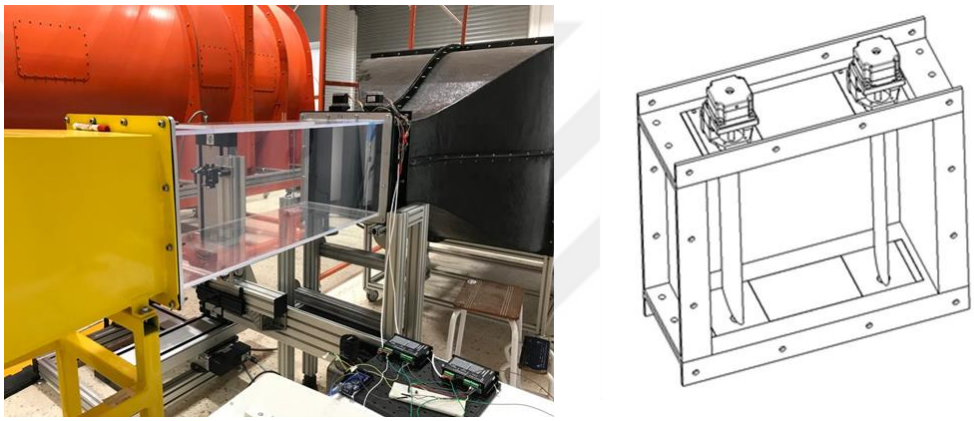


Figure 2.11: RÜZGEM C1 open-circuit wind tunnel and integrated two-dimensional gust generator (left), a three-dimensional CAD drawing of two-dimensional gust generator (right)

2.2.2 PIV Setup

Figure 2.12 shows the experimental setup of the 2D2V PIV experimental setup on the gust generator integrated wind tunnel facility. Free stream velocity is measured using pitot-static tube placed a distance of one chord behind of the vanes at the end of the contraction of the wind tunnel. The total and static pressure data is recorded by miniature intelligent 64-channel Ethernet pressure scanner. The pressure scanner accuracy is 0.20 % of full-scale range for 4 inH_2O. Moreover, barometric pressure and temperature values of the room is recorded during the pressure data is taken. Free stream velocity is then calculated from the average of the collected pressure

data by using ideal gas law. Servo motors are connected to the gust vanes by couplings and are placed to the gust generator frame from the top section. While the motors are rotated sinusoidally in position mode, laser is triggered at certain angles using digital I/O module connected to the cRIO and a synchronizer. Nd: YAG type laser, camera and the lenses with mirrors are placed to a traverse mechanism which can move in three axes. After PIV images is taken for field of view of the first window, traverse mechanism is moved 150 mm downstream to be able to capture field of view of the second window. Later, the same procedure is followed for the field of view of the third window. The Laser head emits a 532 Nm (green light) beam. This beam is reflected upwards (+Z direction) to the required height using Mirror 1. Then, mirror 2 directs the beam in a +Y direction into a series of spherical and cylindrical lenses. The first lens concentrates the beam on the measurement area, while the second transforms it into a laser sheet. At this location, the calibration image is captured, yielding a PIV field of 166 x 256 mm^2 (in X and Y directions, respectively). Table 2.2 and Table 2.3 shows the details of the experimental setup parameters.

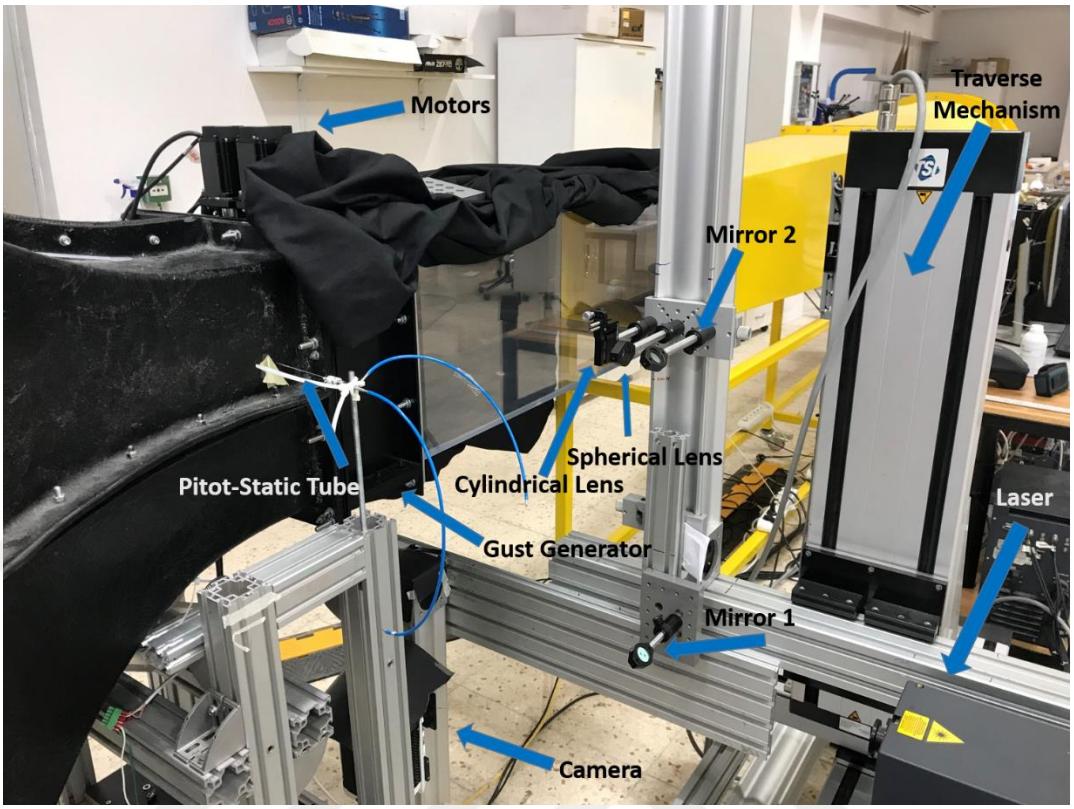


Figure 2.12: 2D2C PIV experiment setup configuration with the gust generator system

Table 2.2: 2D2C PIV Experimental Setup parameters (I)

Seeding	Type	Fog Droplets
	Nominal Diameter	$\approx 1\mu m$
	Seeding Generator	Safex fog generator
Laser Sheet	Laser Type	Nd: YAG
	Manufacturer	New Wave research
	Model	Solo 120XT
	Maximum Energy	120 mJ/pulse
	Wavelength	532 nm
	Thickness	$\approx 2mm$
	Maximum Repetition rate	21 Hz
Optics	Mirrors	Dielectric Mirror, 532 nm
	Spherical Lens	Plano-convex, 500mm FL
	Cylindrical Lens	Plano-concave, -6.4mm FL

Table 2.3: 2D2C PIV Experimental Setup Parameters (II)

Camera	Sensor Type	CMOS
	Sensor resolution	2560 x 1600 pixel^2
	Sensor size	25.6 x 16.0 mm^2
	Pixel pitch (size)	10 μm
	Depth	12 bit
	Repetition rate	1400 fps @ Full resolution 2500 fps @ 1920 x 1080
	Internal memory buffer	16 GB
Camera Lens	Manufacturer	Nikon
	Focal length	60 mm
	f #	5.6
Imaging	Image magnification	0.195
	Field of view (FOV)	166 x 256 mm^2
	Camera-object distance	650 mm
	Time between pulses (Δt)	76 μs
	Scale Factor	10.41 pixel/mm
PIV analysis	Correlation method	Adaptive-correlation
	Interrogation area (IA)	32 x 32 pixel^2
	Overlap between IAs	50%
	Post-processing	Universal Outlier Detection
	Vector spacing	≈ 1.28 mm

2.2.2.1 Particle Image Velocimetry Measurements

In the near-wake field of the gust generator, phase-locked two-dimensional two-component (2D2C) particle image velocimetry (PIV) measurement is performed. The origin coordinate (0,0) of the PIV field of view is selected as between the two vane in y direction and the trailing edge of the gust vanes in x direction. Since the gust generator vanes are in front of the test section, the first window of the PIV FOV

begins from x/c=0.52 chord downstream of the trailing edge of the gust generator vanes and extends to x/c=6.2 chord distance. Three distinct image windows are taken with the traverse mechanism moved 150 mm to get this range for each window. Since the models will be testes mostly placed in between 4 chord and 6 chord distance of the test section 6.2 chord distance is chosen as the maximum PIV field of view for this study. The coordinate system is normalized around the chord length of the gust vanes which is 80 mm. The overlap zones and the field of views of the windows are shown in the PIV measurement domain with the NACA 0015 gust vanes is shown in Figure 2.13. The PIV data is recorded and analyzed using the commercial software DynamicStudio®. The next section goes over the components of the 2D2C PIV experiment.

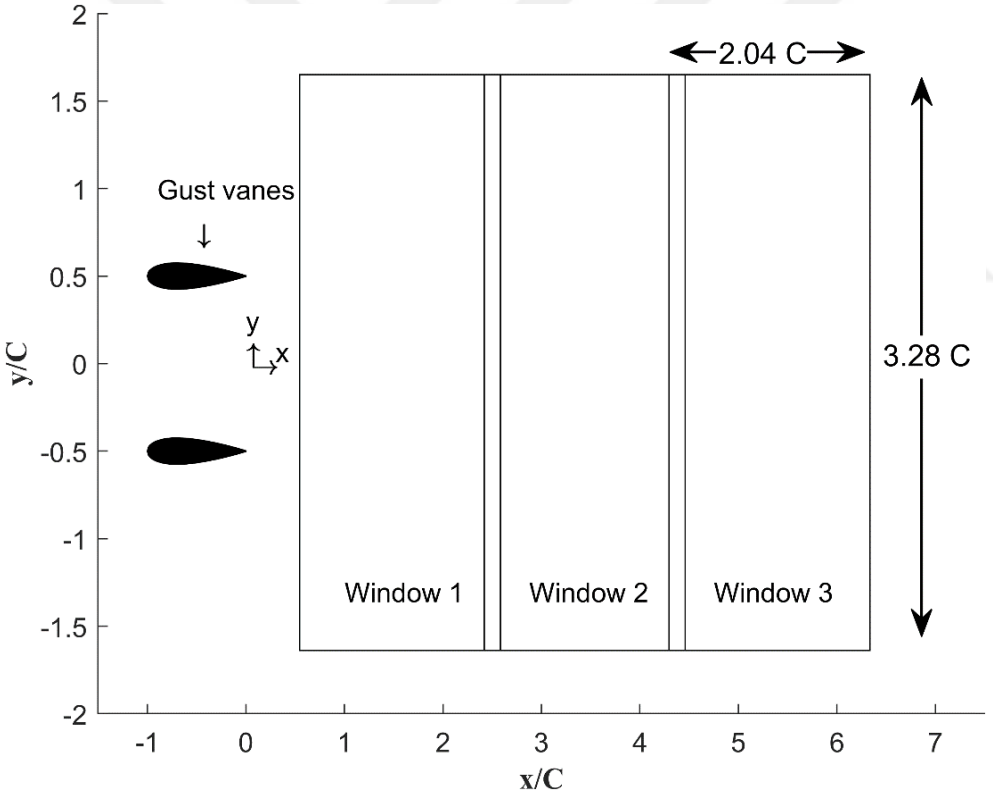


Figure 2.13: The overlap zones and the field of views are shown in the PIV measurement domain with the NACA 0015 gust vanes

2.2.2.2 Gust Measurement Setup

As a preliminary study, to characterize the flow field induced by the gust generator, phase-locked two-dimensional two-component (2D2C) particle image velocimetry (PIV) measurements are performed. PIV measurements are taken for the 2-D gust generator in the RUZGEM suction type wind tunnel test section. The distance between two vanes of the 2-D gust generator is selected as one chord to compare the gust characteristics with the active grid because the distance between two rods that carries the flaps on the active grid is one chord. The wind tunnel free stream velocity is kept constant at 10 m/s. Wind tunnel velocity is measured by a pitot-static tube which is placed in front of the gust vanes. Two different types of sinusoidal motion are applied to the servo motors. First, a sinusoidal flapping motion is applied to the two blades without any phase angle difference between each other, namely, the sinusoidal motion of the vanes is synchronous. This type of motion will be called the in-phase motion case. Three different frequencies (f = 5 Hz, 7.5 Hz, and 10 Hz, corresponding reduced frequencies k = 0.13, 0.19, and 0.25) at a 12-degree maximum deflection angle ($\bar{\theta}$) are applied to investigate the effect of the varying reduced frequency and three different maximum deflection angles ($\bar{\theta} = 8^{\circ}, 12^{\circ}, 16^{\circ}$) at a fixed frequency f =10 Hz or k = 0.25 are applied to investigate the effect of the changing amplitude of the gust generator vanes at constant free-stream wind speed for the in-phase case. The range of the reduced frequency is chosen between 0.13 and 0.25 because it is in limits of the range mostly studied in the literature and upper limit of the frequency is limited physically because of the inertia of the gust vanes. The lower limit of the pitching amplitude is chosen as 8° because lower amplitudes would not be able to generate strong gusts. Upper limit of the pitching amplitude is chosen as 16° because it is static stall angle for the NACA0015 type airfoils. Also, reaching higher angles at high frequencies such as 10 Hz is difficult due to the inertia of the gust vanes. Secondly, a sinusoidal flapping motion is applied to the two blades with a 180° phase angle difference between each other, in other words, an out-of-phase case, and the measurements are taken under the same changing frequency and

changing amplitude values in the in-phase case. For all cases, the phase-locked 2D2C PIV is applied at every 4° to investigate the flow field characteristics in a period of motion. The difference between in-phase and out-of-phase motion motor data at k = 0.25 and $\bar{\theta}$ =12° is shown in Figure 2.14.

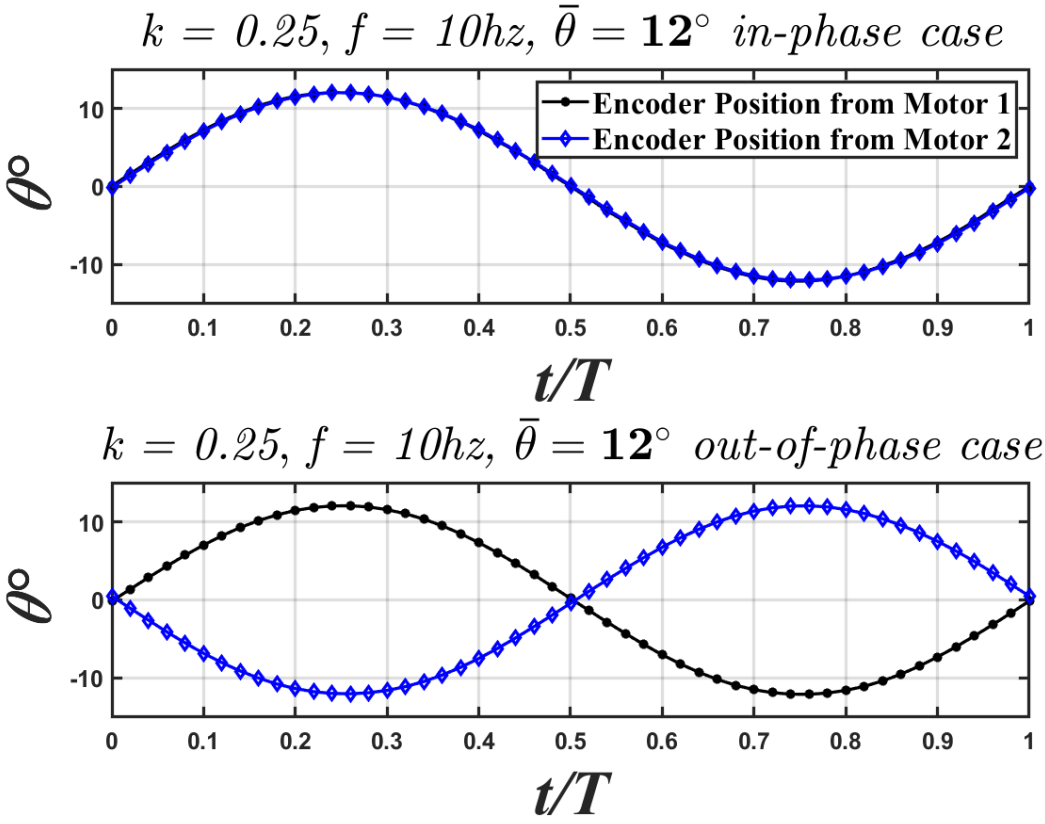


Figure 2.14: Comparison of the vane position data for the in-phase and the out-of-phase cases at k=0.25 and at $\bar{\theta}$ =12° for a period.

The angles where the phase-locked PIV method is applied in a period is presented in Figure 2.15 and Figure 2.16. The first figure shows the phase-locked angles with increasing frequency and the second figure shoes the phase-locked angles with increasing pitching amplitude. While the motor position data is presented by black and blue lines, the phase-phase locked angles are presented by red dots. The test matrix is also presented as a table format in Table 2.4 and Table 2.5.

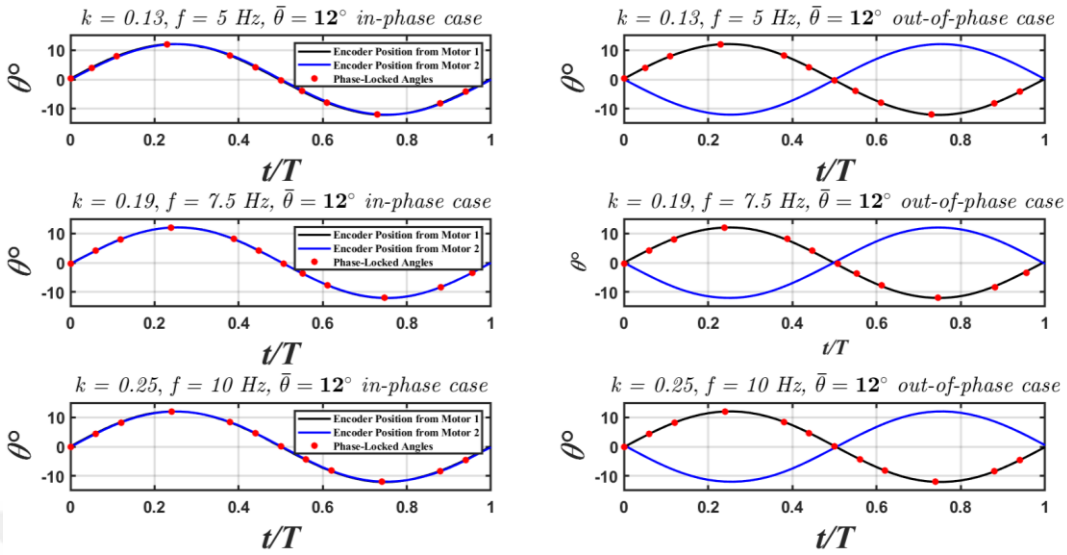


Figure 2.15: Representation of the phase-locked PIV angles in a period for three different frequency test cases at a fixed pitching amplitude for out-of-phase and in-phase motions (motor position data is presented by black and blue lines, the phase-phase locked angles are presented by red dots.)

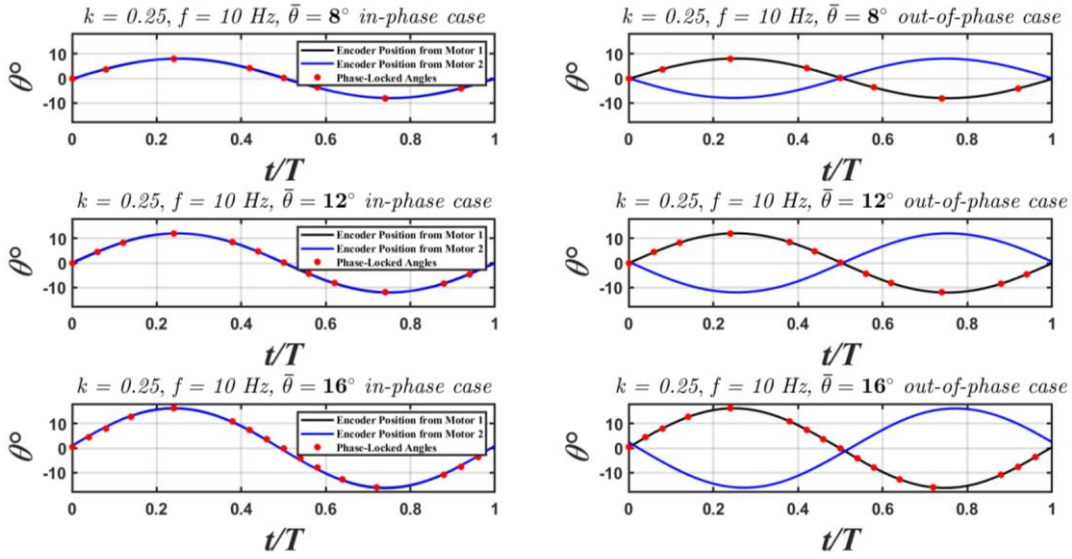


Figure 2.16: Representation of the phase-locked PIV angles in a period for three different pitching amplitude test cases at a fixed reduced frequency for out-of-phase and in-phase motions (motor position data is presented by black and blue lines, the phase-phase locked angles are presented by red dots.)

Table 2.4: Phase Locked 2D2C PIV triggered angle values of a single period for different reduced frequencies

Triggered Angle	$k = 0.13$ $\bar{\theta} = 12^{\circ}$	$k = 0.19$ $\bar{\theta} = 12^{\circ}$	$k = 0.25$ $\bar{\theta} = 12^{\circ}$
0°	✓	✓	✓
4°	✓	✓	✓
8°	✓	✓	✓
12°	✓	✓	✓
8°	✓	✓	✓
4°	✓	✓	✓
0°	✓	✓	✓
-4°	✓	✓	✓
-8°	✓	✓	✓
-12°	✓	✓	✓
-8°	✓	✓	✓
-4°	✓	✓	✓

Table 2.5: Phase Locked 2D2C PIV triggered angle values of a single period for different amplitudes

Triggered Angle	$k = 0.25$ $\bar{\theta} = 8^{\circ}$	$k = 0.25$ $\bar{\theta} = 16^{\circ}$
0°	✓	✓
4°	✓	✓
8°	✓	✓
12°	○	✓
16°	○	✓
12°	○	✓
8°	○	✓
4°	✓	✓
0°	✓	✓
-4°	✓	✓
-8°	✓	✓
-12°	○	✓
-16°	○	✓
-12°	○	✓
-8°	○	✓
-4°	✓	✓

Longitudinal and lateral gust ratios of the gust produced near the wake region of the gust generator blades from (x/C=0.52 to x/C=6.2) for sinusoidal motion are investigated for the test cases above.

2.2.3 Data Processing Techniques

DynamicStudio software is used to analyze PIV images. Raw images are subjected to pre-processing to improve contrast and reduce background noise by subtracting the lowest quality background image from each raw image. The adaptive correlation between each two image pairs with an interrogation window size of 32 x 32 $pixel^2$ is then performed. A resolved field of view of around 166 x 256 mm^2 with a vector resolution of about 1.28 mm, i.e. 99 x 159 vectors, is obtained using a %50 overlap for the interrogation windows. As for post-processing, universal outlier detection on the resultant vector maps in a 3x3 neighborhood is applied. The instantaneous vector flow fields (x, y, U, and V) were saved as data files to be analyzed in MATLAB for further study.

2.2.4 Analysis of the Measurement Errors

2.2.4.1 Uncertainty of the Velocity Vectors

By dividing the particle displacement between consecutive images by the time between the images, the PIV technique calculates velocity vectors. The size of the particle image, the amount of noise, the velocity gradients, and the size of the interrogation window are some of the elements that influence the calculation of the particle displacements and, consequently, the uncertainty. The literature reports that there is typically a 0.05–0.1 pixel range of error for pixel displacement (Brossard et al., 2015). The pixel value was chosen as 0.1 to calculate uncertainty and the time increment between two pulses was 76 μs, in the current study. Following is the calculation:

$$U = \frac{\Delta x}{\Delta t}$$

$$\varepsilon_U = \sqrt{\left(\frac{\partial U}{\partial \Delta t}\varepsilon_{\Delta t}\right)^2 + \left(\frac{\partial U}{\partial \Delta x}\varepsilon_{\Delta x}\right)^2} = \sqrt{\left(-\frac{\Delta x}{\Delta t^2}\varepsilon_{\Delta t}\right)^2 + \left(\frac{1}{\Delta t}\varepsilon_{\Delta x}\right)^2}$$

$$= \frac{1}{\Delta t}\sqrt{(U\varepsilon_{\Delta t})^2 + (\varepsilon_{\Delta x})^2} = \frac{\varepsilon_{\Delta x}}{\Delta t}$$

$$\frac{\varepsilon_{\Delta x}}{\Delta t} = \frac{0.1 \text{ pixel}}{76\text{x}10^{-6}\text{sec}} = 1315.8 \text{ pixel/sec}$$

$$\varepsilon_U = \frac{1315.8 \text{ pixel/sec}}{10.41 \text{ pixel/mm}} = 126.40 \frac{\text{mm}}{\text{sec}} = 0.1264 \frac{\text{m}}{\text{sec}}$$

The uncertainty of the terminal velocity becomes:

$$\frac{\varepsilon_U}{U} = \sqrt{\frac{1}{\Delta t^2}\left[\varepsilon_{\Delta t}^2 + \frac{\varepsilon_{\Delta x}^2}{U^2}\right]} = \sqrt{\left(\frac{\varepsilon_{\Delta t}}{\Delta t}\right)^2 + \left(\frac{\varepsilon_{\Delta x}}{\Delta x}\right)^2} = \frac{0.1264 \text{ m/sec}}{10 \text{ m/sec}} = 0.01264$$

$$100 \text{ x } \frac{\varepsilon_U}{U} = 1.26 \text{ \%}$$

2.2.4.2 Uncertainty of the Angle of Incidence

For calculation of uncertainty in the angle of incidence, first, the angle of incidence at a certain location for in-phase motion in one of the phase angles of the baseline case is calculated. Then the standard deviation of 100 samples is computed. The calculation is as follows:

Measured standard deviation, $\sigma = \left[\frac{1}{N}\sum_{i=1}^{N}(\Phi_i - \Phi)^2\right]^{½} = 0.0431$

$Uncertainty\ (u) = \frac{k\sigma}{\sqrt{N}}$ where k is the coverage factor and N is the number of samples which is equal to 100 in this study. The k is 1.96 for 95% confidence level, therefore:

$$Uncertainty\ (u) = \frac{1.96 \text{ x } 0.0431}{\sqrt{100}} = 0.0085\ °$$

Percent uncertainty of the angle of incidence becomes, $\frac{0.0085}{2.409}$x$100 = 0.35\%$

2.2.4.3 Uncertainty of the Stream-wise Gust Ratio

The uncertainty calculation procedure of the stream-wise gust ratio is the same as the angle of incidence uncertainty calculation procedure.

Measured standard deviation, $\sigma = \left[\frac{1}{N}\sum_{i=1}^{N}(\mathrm{u/U_i} - \mathrm{u/U})^2\right]^{½} = 0.0028$

$Uncertainty\ (u) = \frac{k\sigma}{\sqrt{N}}$ where k is the coverage factor and N is the number of samples that is equal to 100 in this study. The k is 1.96 for a 95% confidence level, therefore:

$$Uncertainty\ (u) = \frac{1.96 \text{ x } 0.0028}{\sqrt{100}} = 0.000549\ °$$

Percent uncertainty of the angle of incidence becomes, $\frac{0.000549}{0.9773}$x$100 = 0.056\%$

2.2.4.4 Uncertainty of the Transverse Gust Ratio

The uncertainty calculation procedure of the transverse gust ratio is the same as the angle of incidence uncertainty calculation procedure.

Measured standard deviation, $\sigma = \left[\frac{1}{N}\sum_{i=1}^{N}(\mathrm{v/U_i} - \mathrm{v/U})^2\right]^{½} = 0.000659$

$Uncertainty\ (u) = \frac{k\sigma}{\sqrt{N}}$ where k is the coverage factor and N is the number of samples that is equal to 100 in this study. The k is 1.96 for a 95% confidence level, therefore:

$$Uncertainty\ (u) = \frac{1.96 \text{ x } 0.000659}{\sqrt{100}} = 0.000129\ ^\circ$$

Percent uncertainty of the angle of incidence becomes, $\frac{0.0085}{0.0395}\text{x}100 = 0.327\%$

2.2.4.5 Uncertainty of the Initial Position of the Gust Vanes

Adjusting the initial position of the gust vanes at zero angle of attack before starting the experiments has also an error due to it is done manually. To adjust the zero angle of attack of the gust vanes a ruler is used based on the distance between the tunnel wall and trailing edge of the vanes. Later the distance between the two vanes is fine tuned to one chord distance. Considering that the uncertainty of the ruler is 1 mm and the vanes are rotated around the quarter chord, the angular uncertainty of the vanes becomes less than 5.9% for pitching motion of $\pm 8°$, less than 3.9% for pitching motion of $\pm 12°$ and less than 2.9% for pitching motion of $\pm 16°$. Due to the high uncertainty error margin of the zero angle of attack alignment, asymmetrical flow structures can be observed in the flow field especially for the out-of-phase motion of the vanes.

CHAPTER 3

RESULTS AND DISCUSSION

The results of the study are discussed in this chapter in terms of temporal and spatial variations in the flow field. In the first section, temporal results of the angle of incidence and stream-wise and transverse gust ratio parameters are presented from flow field obtained by PIV measurements at fixed downstream positions in the mid-plane of the gust vanes to investigate the near and far wake relations. In the second section, the contour plots of a number of flow properties at different reduced frequencies and different pitching amplitudes are presented at various phases of the vane motion. The baseline case is selected as a frequency of the vane is 10 Hz, corresponding reduced frequency, *k*, of 0.25, at free-stream velocity of 10 m/s, and a pitching amplitude of 12°. When the reduced frequency of the baseline case is fixed, the pitching amplitude is varied and when the pitching amplitude of the baseline case is fixed, the reduced frequency is varied for the other cases in the study. The contour plots of all the test cases are listed in Appendices chapter.

3.1 Temporal Results

To investigate the effect of the sinusoidal motion of two gust vanes with and without phase difference, the change of the angle of incidence, stream-wise and transverse gust ratio parameters are examined in a single period of the sinusoidal motion of the blades. The angle of incidence (AoI, ϕ°) is defined as the ratio of the vertical velocity component v to the stream-wise velocity component u of the flow velocity $\phi = \tan^{-1}(v/u)$. The variation of the AoI at the 0.6 chord length downstream position from the trailing edge of the vanes at different reduced frequency and the deflection angle values is shown in Figure 3.1. The stream-wise position of x/C=0.6 is selected to monitor the velocity variations because it is in the near wake, where

this study aims to explore the flow dynamics, and it is the nearest position to the gust vanes where reliable PIV data is collected. When the vanes are operated in an out-of-phase motion (i.e., 180° phase lag between their sinusoidal pitching motion kinematics), there is no significant variation in the incidence angle during the period of the motion. The angle of incidence is almost insensitive to both reduced frequency and angular amplitude variations in the case of the out-of-phase motion. On the other hand, the in-phase motion of the gust vanes (no phase lag between the sinusoidal pitching motion kinematics of the gust vanes) produces a sinusoidal profile with an amplitude of $5^{\circ} - 10^{\circ}$. The increasing reduced frequency slightly increases the amplitude of the incidence angle in the flow, whereas the increasing maximum deflection angle at a given reduced frequency significantly increases the amplitude of the angle of incidence.

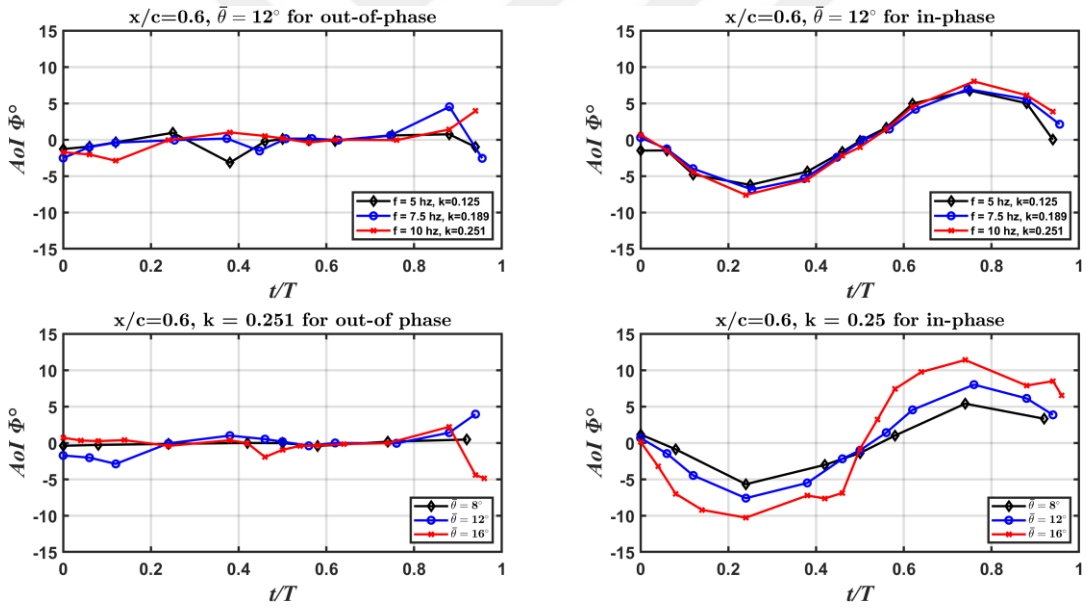


Figure 3.1: Comparison of the angle of incidence (ϕ°) for different frequencies and different amplitudes of a sinusoidal period for both in and out-of-phase cases at x/c=0.6 and y/c=0 location

Transverse gust ratio v/U_∞ is investigated in Figure 3.2 for all cases. The behavior of the motion is similar to the angle of incidence suggesting that the stream-wise component of the velocity at a given position stays rather constant. It is also clear that the in-phase motion of the gust vanes generates continuous sinusoidal gust with a well-defined profile even in the near wake of the gust vanes.

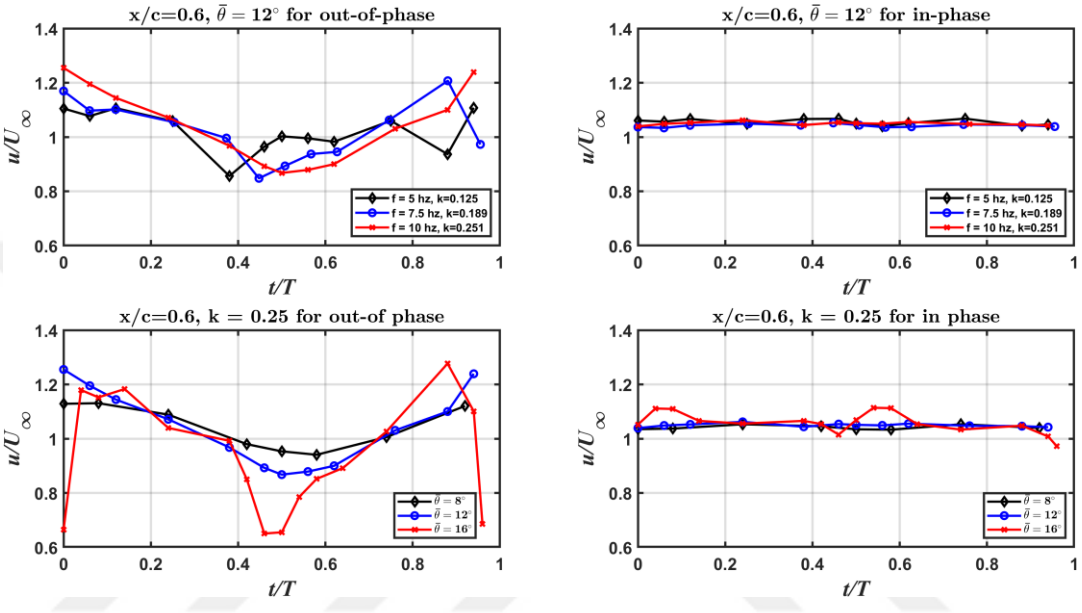


Figure 3.2: Comparison of the normalized transverse gust ratio v/U_∞ for different frequencies and different amplitudes of a sinusoidal period for both in and out-of-phase cases at x/c=0.6 and y/c=0 location

The stream-wise gust ratio does not show any variations in the case of the in-phase motion as shown in Figure 3.3. Regardless of the pitching amplitude and reduced frequency, the in-phase motion of the gust vanes yields a more-or-less constant stream-wise velocity in the near wake, which is slightly higher than the free-stream velocity. This difference is due to the acceleration of the flow caused by the blockage of the gust vanes. The out-of-phase motion of the vanes, on the other hand, yields prominent variations in the stream-wise gust ratio.

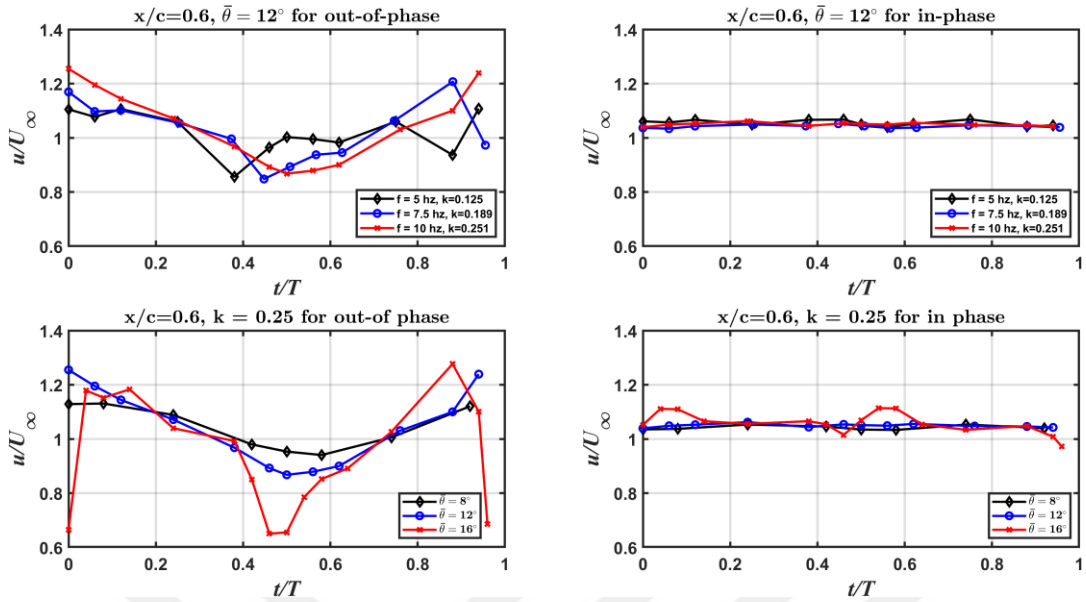


Figure 3.3: Comparison of the normalized stream-wise gust ratio u/U_{∞} for different frequencies and different amplitudes of a sinusoidal period for both in and out-of-phase cases at x/c=0.6 and y/c=0 location

Figure 3.4 shows the comparison of the angle of incidence gust characteristics at the near wake (x/c=0.6) and far wake (x/c=4 and x/c=6) at three different reduced frequency values at k = 0.13, k = 0.19 and k = 0.25 and pitching amplitude of 12°. There is an obvious phase lag between the near wake x/c=0.6 and the far wake x/c=6 flow characteristics for in-phase motion. The development of the phase lag can be observed at x/c=4 location as well. Figure 3.5 investigates the same conditions for the transverse gust ratio property. Similar trend is observed in transverse gust ratio with the angle of incidence. In addition, the magnitudes of the AoI and the gust ratio decrease moving in the stream-wise direction. While the phase lag can be observed in AoI and transverse gust ratio for the in-phase case, the stream-wise gust ratio remains stable around the normalized value.

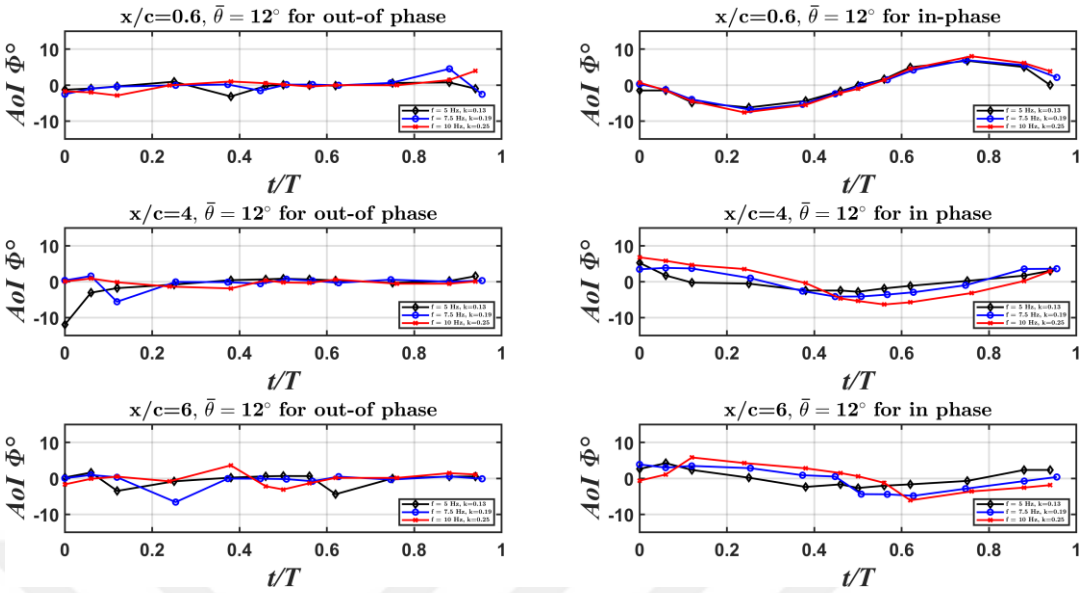


Figure 3.4: Comparison of AoI variations at near and far wake regions (x/c=0.6, x/c=4 and x/c=6) for three different reduced frequencies k=0.13, f =5 Hz (black) k=0.19 , f =7.5 Hz (blue) k=0.25 , f =10 Hz (red) at y/c=0 and at U_{∞}=10 m/s

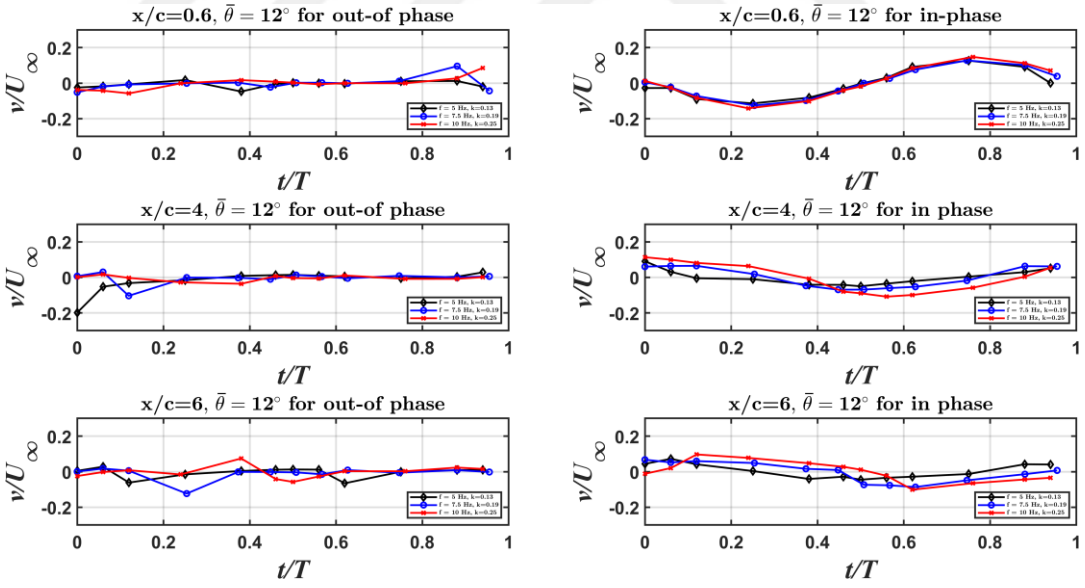


Figure 3.5: Comparison of transverse gust ratio variations at near and far wake regions (x/c=0.6, x/c=4 and x/c=6) for three different reduced frequencies k=0.13, f =5 Hz (black) k=0.19 , f =7.5 Hz (blue) k=0.25 , f =10 Hz (red) at y/c=0 and at U_{∞}=10 m/s

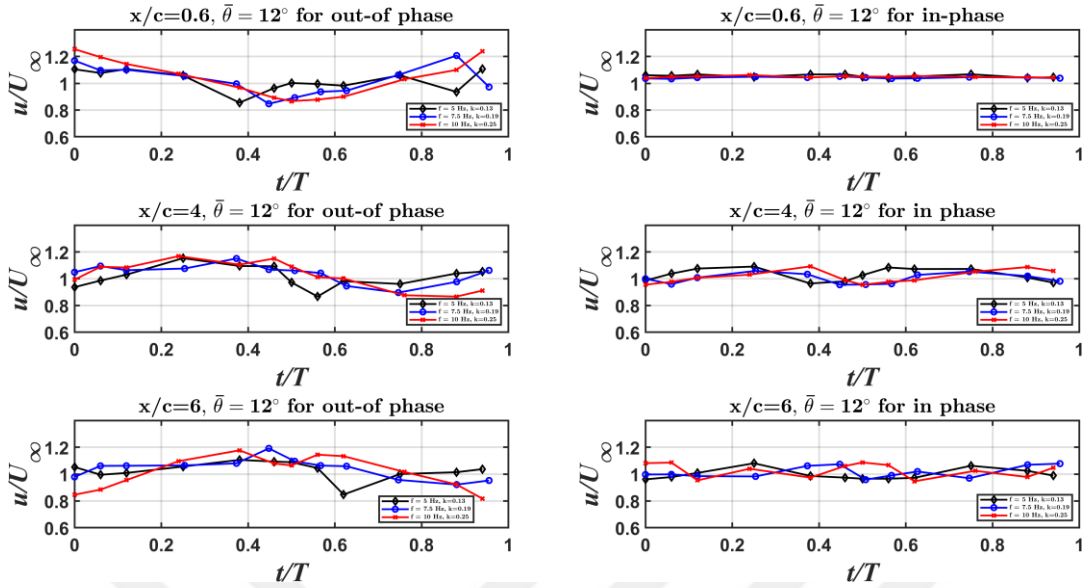


Figure 3.6: Comparison of stream-wise gust ratio variations at near and far wake regions (x/c=0.6, x/c=4 and x/c=6) for three different reduced frequencies k=0.13, f =5 Hz (black) k=0.19 , f =7.5 Hz (blue) k=0.25 , f =10 Hz (red) at y/c=0 and at U_{∞}=10 m/s

Figure 3.6 shows the comparison of the stream-wise gust ratio characteristics at the near wake (x/c=0.6) and far wake (x/c=4 and x/c=6) at three different reduced frequency values at k = 0.13, k = 0.19 and k = 0.25 and pitching amplitude of 12°. For the out-of-phase case, the phase lag between near wake and far wake is observed in the stream-wise gust ratio rather than the transverse gust ratio. The development of the phase lag between near wake and far wake can be observed at x/c=4 location as well. It can be observed that the effect of increasing reduced frequency is stronger in the near wake region, since the maximum amplitude of streamwise gust ratio at x/c=0.6 is higher than the maximum amplitude of streamwise gust ratio at x/c=6 location. Figure 3.7 shows the comparison of the angle of incidence gust characteristics at the near wake (x/c=0.6) and far wake (x/c=4 and x/c=6) at three different pitching amplitude values at $\bar{\theta} = 8°$, $\bar{\theta} = 12°$ and $\bar{\theta} = 16°$ and reduced frequency of k = 0.25. Unlike the reduced frequency case, the sinusoidal profile is disrupted with increasing amplitude as it approaches the far wake region in the increasing pitching amplitude plots for in-phase motion case. Sudden changes in the sinusoidal period of the AoI can be observed especially for the $\bar{\theta} = 16°$. Also, there

is an obvious phase lag between the near wake x/c=0.6 and the far wake x/c=6 flow characteristics for in-phase motion. The development of the phase lag can be observed at x/c=4 location as well.

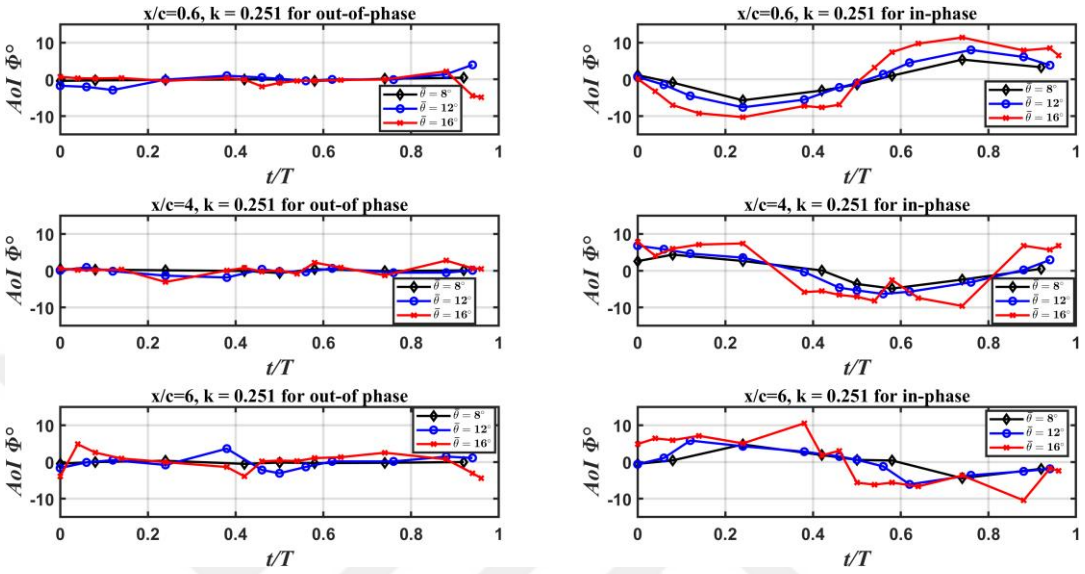


Figure 3.7: Comparison of AoI variations at near and far wake regions (x/c=0.6, x/c=4 and x/c=6) for three different pitching amplitude $\bar{\theta} = 8°$ (black) , $\bar{\theta} = 12°$ (blue), $\bar{\theta} = 16°$ (red) at y/c=0, at a fixed frequency k=0.25 and at U_∞=10 m/s

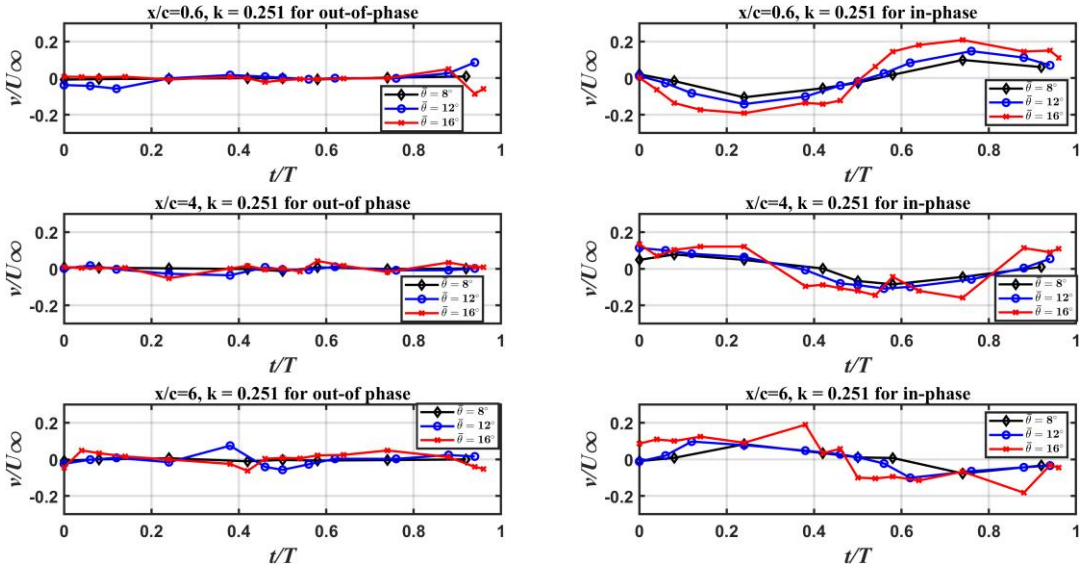


Figure 3.8: Comparison of transverse gust ratio variations at near and far wake regions (x/c=0.6, x/c=4 and x/c=6) for three different pitching amplitude $\bar{\theta} = 8°$ (black) , $\bar{\theta} = 12°$ (blue), $\bar{\theta} = 16°$ (red) at y/c=0, at a fixed frequency k=0.25 and at U_∞=10 m/s

Figure 3.8 investigates the same conditions for the transverse gust ratio characteristics. Similar trend is observed in transverse gust ratio with the angle of incidence. In addition, the magnitudes of the AoI and the gust ratio decrease moving in the stream-wise direction. Figure 3.9 shows the comparison of the stream-wise gust ratio characteristics at the near wake (x/c=0.6) and far wake (x/c=4 and x/c=6) at three different pitching amplitude values at $\bar{\theta} = 8°$, $\bar{\theta} = 12°$ and $\bar{\theta} = 16°$ and reduced frequency of $k = 0.25$. For the in-phase motion case, the phase lag between the near wake and far wake is observed in the stream-wise gust ratio rather than the transverse gust ratio.

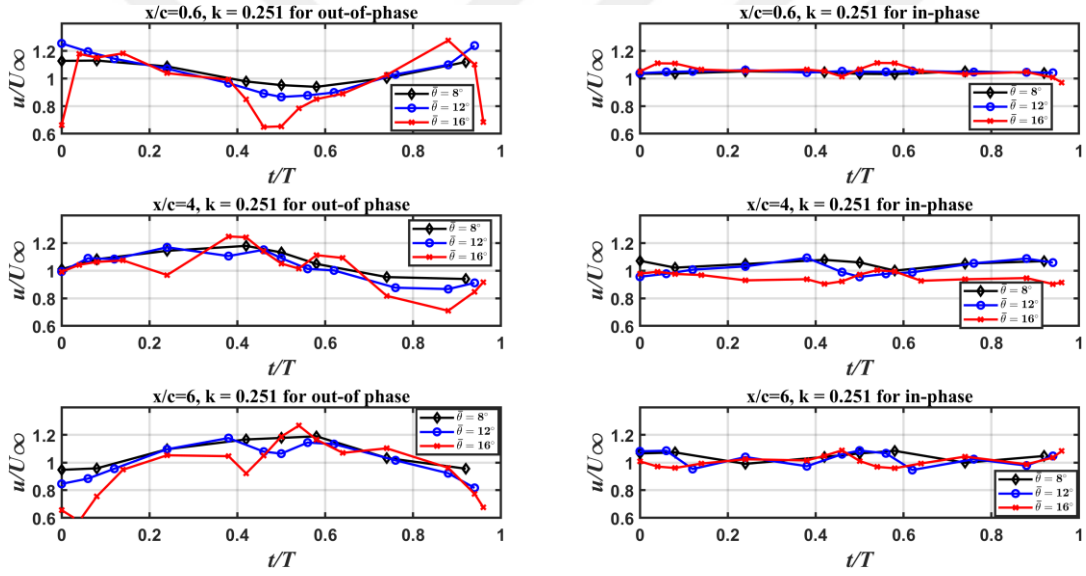


Figure 3.9: Comparison of stream-wise gust ratio variations at near and far wake regions (x/c=0.6, x/c=4 and x/c=6) for three different pitching amplitude $\bar{\theta} = 8°$ (black) , $\bar{\theta} = 12°$ (blue), $\bar{\theta} = 16°$ (red) at y/c=0, at a fixed frequency $k=0.25$ and at U_∞=10 m/s

In the next section, the findings from the stream-wise and the transverse gust ratios and the out-of-plane vorticity contour plots in the flow fields behind the gust generator vanes will be presented.

3.2 Spatial Results

In this section, gust parameters are investigated by means of the results of the phase-locked PIV measurements. Synchronous in-phase and out-of-phase cases, with a pitching amplitude of 12 degrees and a reduced frequency of 0.25, are defined as baseline cases (between Figure 3.10 and Figure 3.15). To investigate the effects of the frequency and the amplitude of the sinusoidal pitching motion on the generated gust profiles, the stream-wise and transverse gust ratios and vorticity fields, respectively, are shown in the figures below. Later, the effects of the pitching amplitude on the flow field are compared for three different deflection angles (between Figure 3.16 and Figure 3.19). At the end, the effects of the reduced frequency on the flow fields are explored by comparing three different reduced frequency cases at the same maximum and minimum deflection angle of the vanes (between Figure 3.20 and Figure 3.23).

In accordance with the temporal results, at vertical coordinates (y/c) corresponding to the region between the two vanes, an almost constant stream-wise gust ratio is attained as shown in Figure 3.10. Patches of relatively high-speed stream-wise flow appear in the regions between the vanes and the tunnel walls, which form due to varying blockage ratio and thus changing flow passage area during the pitching motion of the vanes. In this respect, the effective area in which a model can be placed to explore its aerodynamic response to a transverse gust is rather limited. On the other hand, the vertical velocity component display more homogeneous distributions during the course of the vane pitching motion (see Figure 3.11). Accordingly, a sinusoidal transverse gust profile is achieved between the vanes as also shown in Figure 3.2. Coherent fluid regions with non-zero vertical velocity advect downstream without a significant variation in their topology, which explains the phase lag between the gust ratio profiles of the x/c=0.6 and x/c=6.0 positions as observed in Figure 3.5. Contour of out-of-plane vorticity presented in Figure 3.12 reveals that there is no direct interaction between the wake vorticity layers of the two

vanes. However, it is clear that one should pay attention while placing the model in the test section to avoid interaction with the shear layers of the vanes.

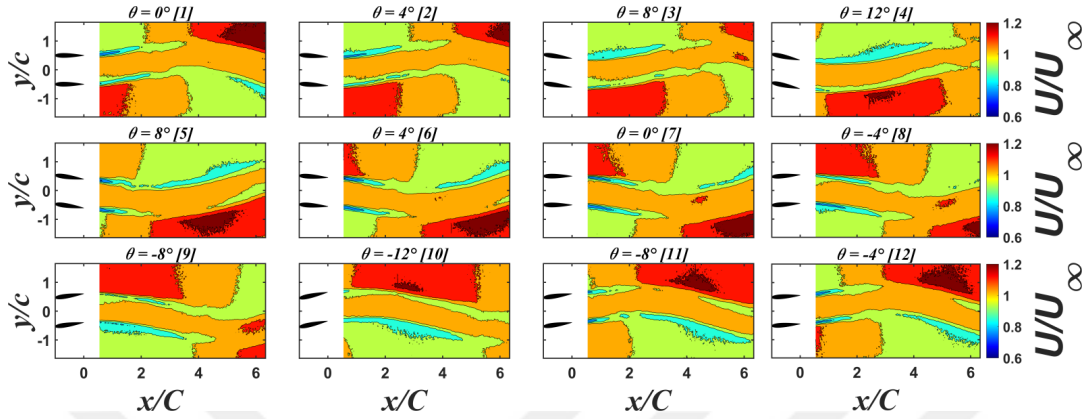


Figure 3.10: Stream-wise gust ratio contour plots of FOV for reduced frequency k = 0.25 and with a maximum amplitude of $\bar{\theta} = 12^{\circ}$ in-phase case at different phase angles

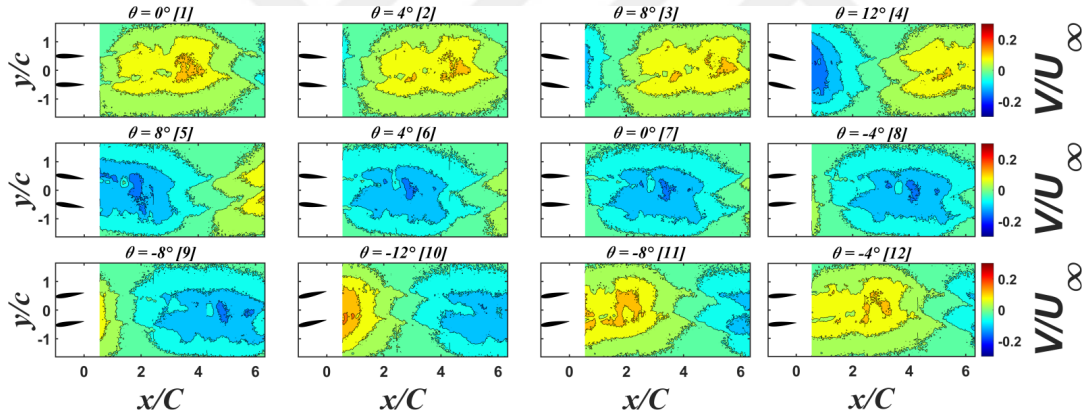


Figure 3.11: Transverse gust ratio contour plots of FOV for reduced frequency k =0.25 and with a maximum amplitude of $\bar{\theta} = 12^{\circ}$ in-phase case at different phase angles

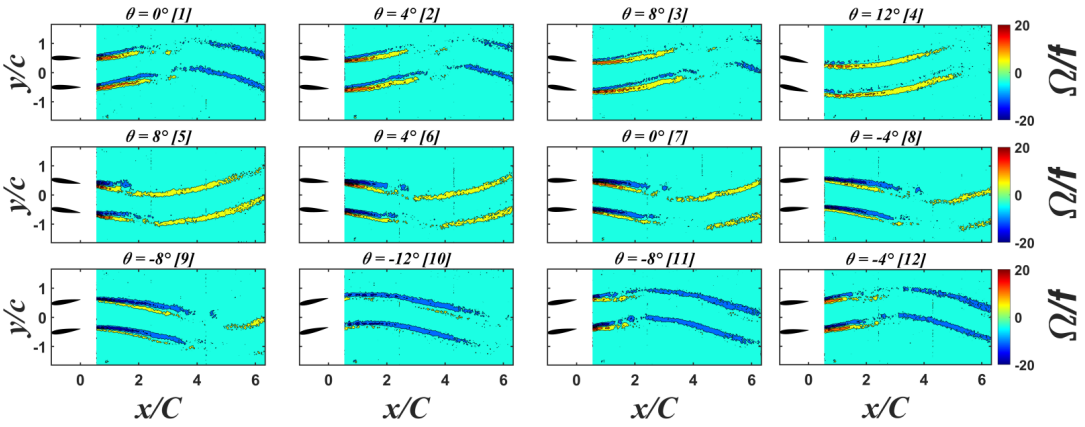


Figure 3.12: Contours of out-of-plane vorticity at the reduced frequency of $k = 0.25$ and the pitching amplitude of $\bar{\theta} = 12^{\circ}$ for in-phase case at different phase angles

Figure 3.13 shows the contours of the stream-wise gust ratio for the out-of-phase motion of the gust vanes during a period. In this case, the vane motion results in a prominent variation in the stream-wise velocity values in the center of the test section. While the trailing edges of the vanes approaching each other (while the vanes are performing a sort of clapping motion), a positive stream-wise velocity pattern emerges in the wake. The opposite occurs in the other half of the stroke, which leads to alternating pattern in the stream-wise gust ratio, as shown in Figure 3.3. The contours of the transverse gust ratio reveal almost constant vertical velocity values along the center of the test section (y/c=0), which can also be inferred from Figure 3.2. However, slightly above or below the centerline, non-zero vertical velocity contours are present. This is due to the fact that induced velocities of the bound circulations and trailing edge vortices of the upper and lower vanes cancels each other out in the vertical direction along the centerline. However, non-zero vertical velocity values are achieved at slightly off-centerline vertical positions. Contours of the out-of-plane vorticity in Figure 3.15 display starting vortex pairs of the upper and lower vanes, which are formed during the stroke reversals. The induced velocities of these vortex pairs have either constructive or destructive effect in terms of the stream-wise gust ratio. For instance, the vortex pair at θ=-12 [10] induces a negative stream-wise velocity, decreasing the free-stream velocity along

the centerline, as can be inferred from Figure 3.15. An opposite behaviour is observed at θ=-12 [4] such that the induced velocity of the vortices adds to the free-stream velocity component. A small asymmetrical behaviour can also be observed in out-of-plane motion contour plots of the flow field. This is due to the misalignment of the zero angle of attack at the initial position caused by the uncertainty of the ruler. Any small difference of the initial angle of attack alignment of the two gust vanes could cause asymmetrical motion of the vanes which effects the flow field.

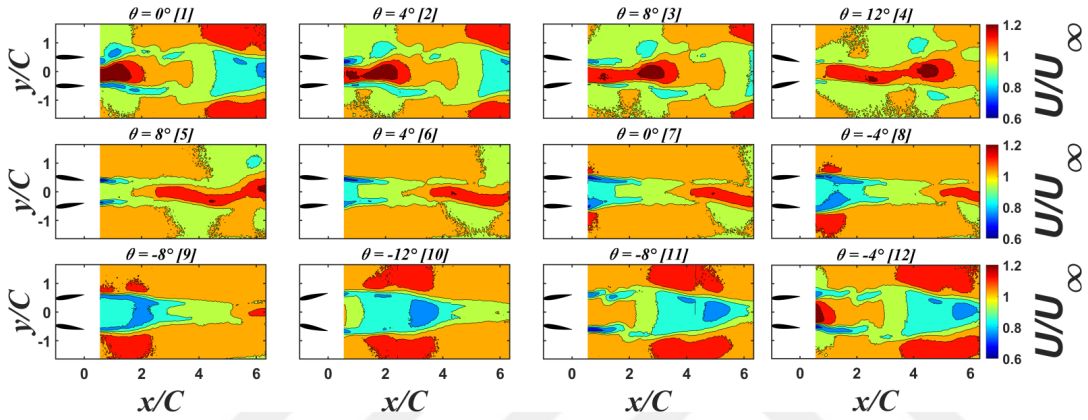


Figure 3.13: Stream-wise gust ratio contour plots of FOV for reduced frequency k = 0.25 and with a maximum amplitude of $\bar{\theta} = 12^{\circ}$ out-of-phase case at different phase angles

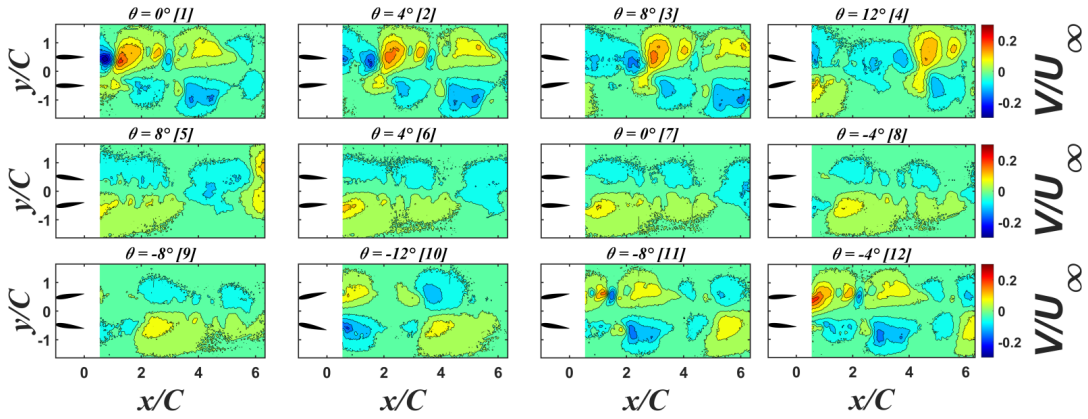


Figure 3.14: Transverse gust ratio contour plots of FOV for reduced frequency k = 0.25 and with a maximum amplitude of $\bar{\theta} = 12^{\circ}$ out-of-phase case at different phase angles

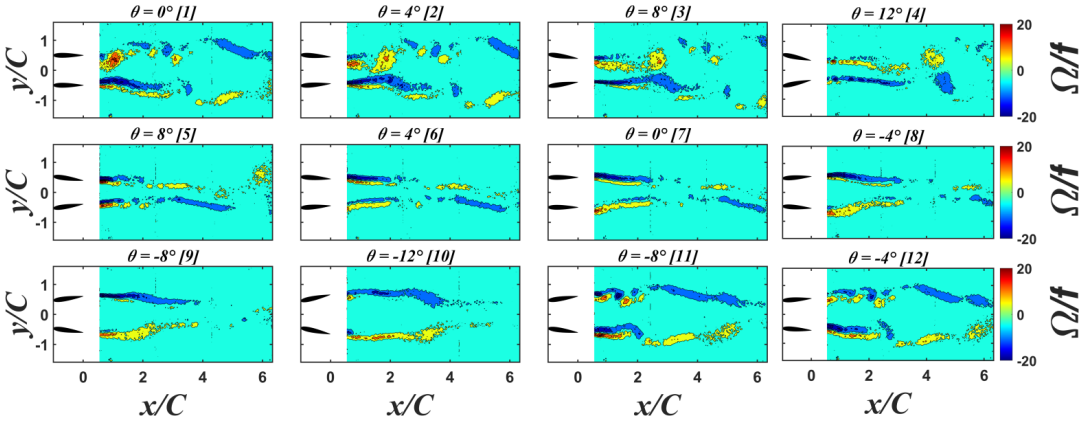


Figure 3.15: Contours of out-of-plane vorticity at the reduced frequency of $k = 0.25$ and the pitching amplitude of $\bar{\theta} = 12^{\circ}$ out-of-phase case at different phase angles

3.2.1 Effect of Increasing Amplitude on the Gust Parameters

In order to investigate the effect of the pitching amplitude on the generated gust profiles, contours of stream-wise gust ratio, transverse gust ratio and the out-of-plane vorticity are presented at the phases corresponding to the maximum deflection angles of the cases with the pitching amplitudes 8°, 12° and 16°. Increasing the pitching amplitude to 16° leads to the separation of the flow on the NACA0015 vanes. As a result of the flow separation, more coherent vortical patterns emerge in the wake of the vanes both in the cases of the in-phase and out-of-phase motions. For the in-phase cases, increasing the pitching amplitude results in an increase of the transverse gust ratio, as also shown in Figure 3.2. However, the symmetry and homogeneity of the transverse gust patterns breaks down for the case of 16° pitching amplitude, which most probably stems from the flow separation and associated wake vorticity region. The out-of-phase motion of the vanes at a larger pitching amplitude increases the stream-wise gust ratio in the wake yet with the drawback of flow separation and number of coherent vortices shed into the wake. On the other hand, at the smallest pitching amplitude case, a more regular and uniform stream-wise gust patterns are observed. The amount of vorticity shed into the wake is also much less at the small pitching amplitude case, which can be considered more convenient in terms of studying the gust response of an aerodynamic model in the test section.

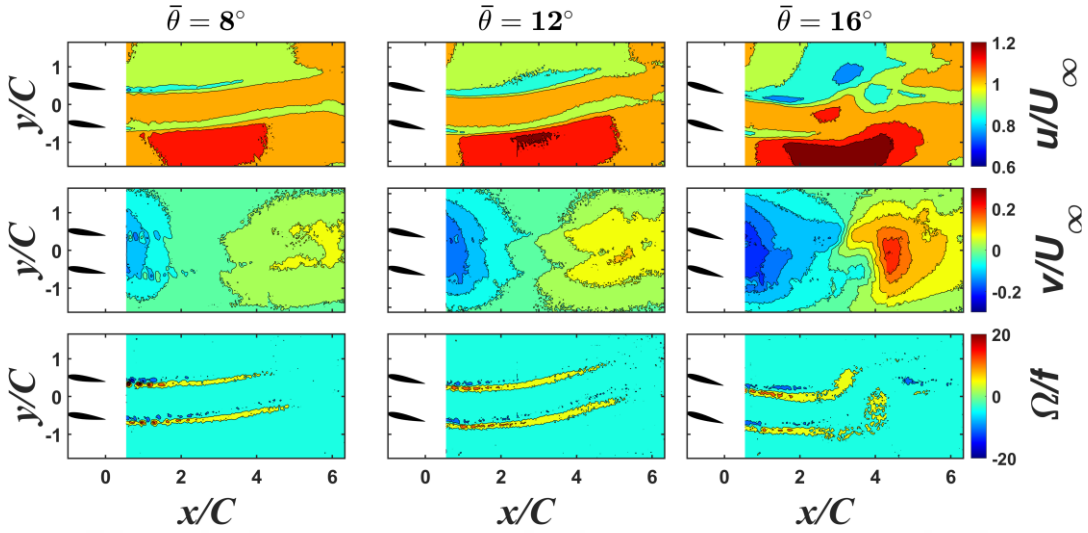


Figure 3.16: Comparison of the stream-wise and transverse gust ratio and vorticity for different maximum deflection angles for their maximum amplitudes (8°, 12°, 16°) at *k*=0.25 for in-phase case

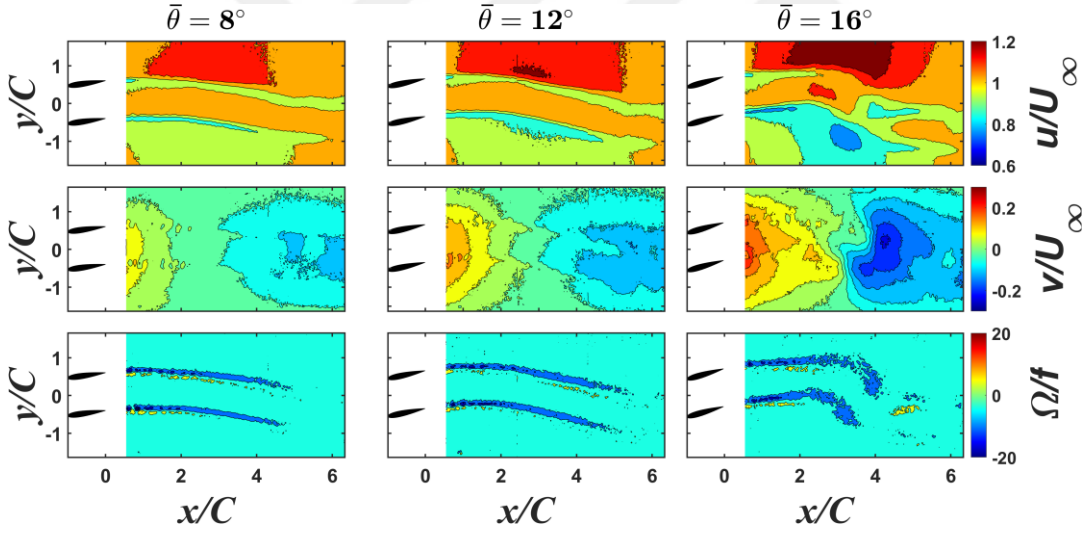


Figure 3.17: Comparison of the stream-wise and transverse gust ratio and vorticity for different maximum deflection angles for their maximum amplitudes (-8°, -12°, -16°) at *k*=0.25 for in-phase case

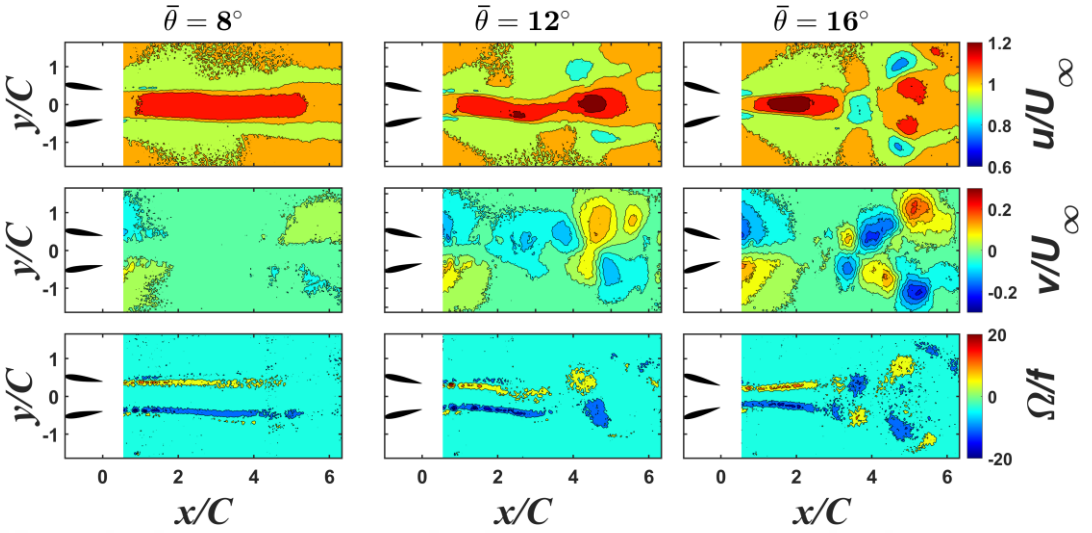


Figure 3.18: Comparison of the stream-wise and transverse gust ratio and vorticity for different maximum deflection angles for their maximum amplitudes (8°, 12°, 16°) at *k*=0.25 for out-of-phase case

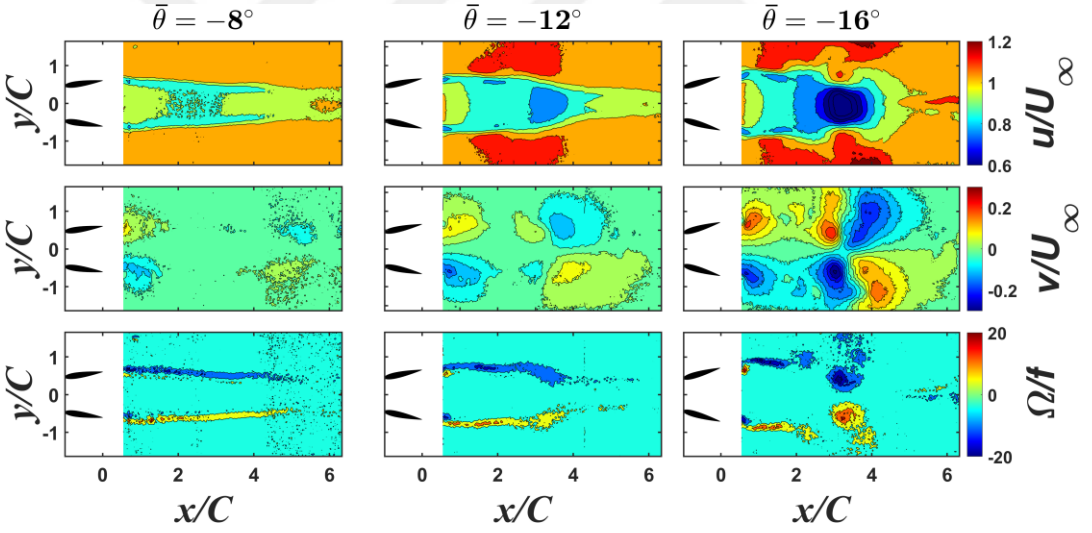


Figure 3.19: Comparison of the stream-wise and transverse gust ratio and vorticity for different maximum deflection angles for their maximum amplitudes (-8°, -12°, -16°) at *k*=0.25 for out-of-phase case

3.2.2 Effect of Increasing Reduced Frequency on the Gust Parameters

In order to investigate the effect of the reduced frequency on the generated gust profiles, contours of stream-wise gust ratio, transverse gust ratio and the out-of-plane vorticity are presented at the phases corresponding to the reduced frequency values of the cases with the reduced frequencies, k = 0.13, 0.19 and 0.25 at a fixed pitching amplitude of 12°. It is stated that the in-phase motion of the gust vanes produces a sinusoidal profile angle of incidence with an amplitude of $5^{\circ} - 10^{\circ}$ in Figure 3.1. However, in Figure 3.2, it is observed that increasing the reduced frequency while the pitching amplitude is fixed does not give a significant increase in the amplitude of the transverse gust ratio in the near-wake field. This observation appears to be invalid when examining the far wake region from the temporal results from Figure 3.4 and Figure 3.5. The finding about the far wake region obtained from the temporal results is also supported when examining the far wake region from the spatial results from Figure 3.20 and Figure 3.21. It is observed that the transverse gust ratio seems to be increased by increasing the reduced frequency when the far-field region is examined. Namely, increasing reduced frequency affects the far wake region rather than the near wake region of a gust generator for the in-phase motion of the vanes. The effect of vorticity seems to change from increasing reduced frequency in terms of the strength and the durability for phase-in cases (see Figure 3.20 and Figure 3.21). As the effect of the increasing amplitude appears on the stream-wise velocity variation at the centerline of the test section, the effect of the increasing reduced frequency also increases the stream-wise gust ratio of the flow field for the out-of-phase motion of the gust vanes (see Figure 3.22 and Figure 3.23). The effect of vorticity also increases for the out-of-phase cases as can be observed in Figure 3.22 and Figure 3.23. The out-of-phase motion of the vanes at a larger reduced frequency increases the stream-wise gust ratio in the wake however with the handicap of flow separation and number of coherent vortices shed into the wake. The amount of vorticity shed into the wake is much large at the high reduced frequency case, which can be considered as a question mark in terms of studying the gust response of an

aerodynamic model in the test section, if the one does not want any vortex interaction with its model under the stream-wise gust.

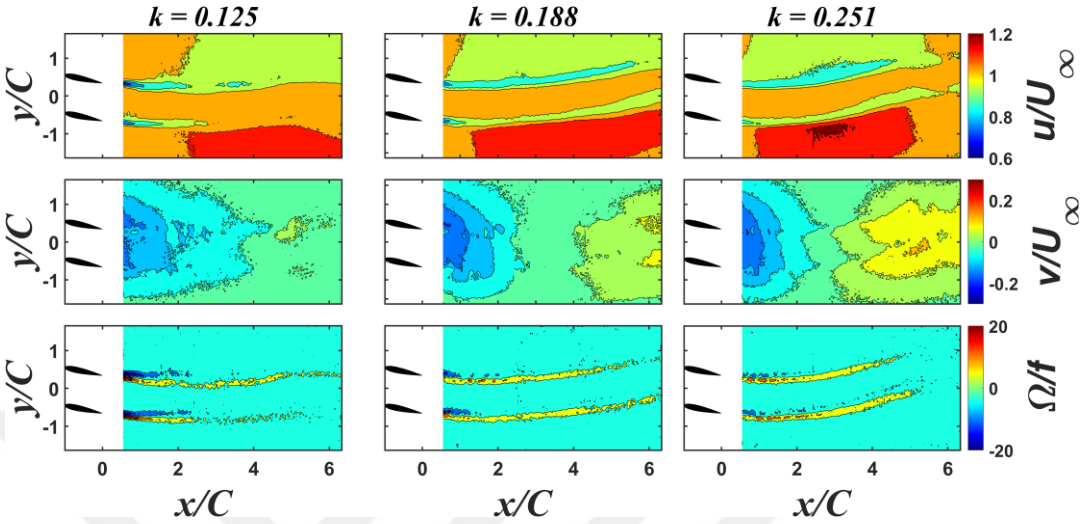


Figure 3.20: Comparison of the stream-wise and transverse gust ratio and vorticity fields for different reduced frequencies (k=0.13, k=0.19, and k=0.25) at the same deflection angle $\theta = 12°$ for in-phase case

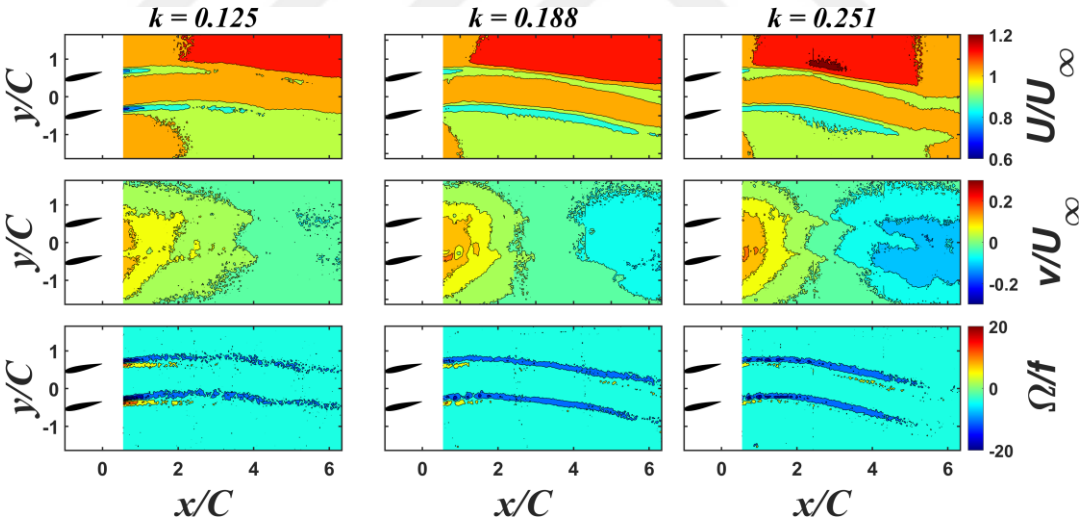


Figure 3.21: Comparison of the stream-wise and transverse gust ratio and vorticity fields for different reduced frequencies (k=0.13, k=0.19, and k=0.25) at the same deflection angle $\theta = -12°$ for in-phase case

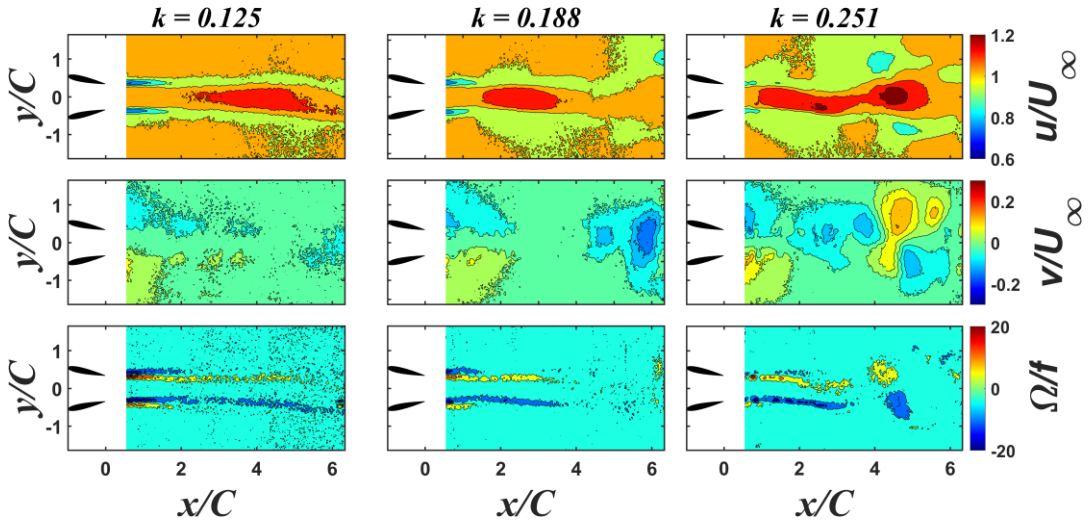


Figure 3.22: Comparison of the stream-wise and transverse gust ratio and vorticity fields for different reduced frequencies (k=0.13, k=0.19, and k=0.25) at the same deflection angle $\theta = 12°$ for out-of-phase case

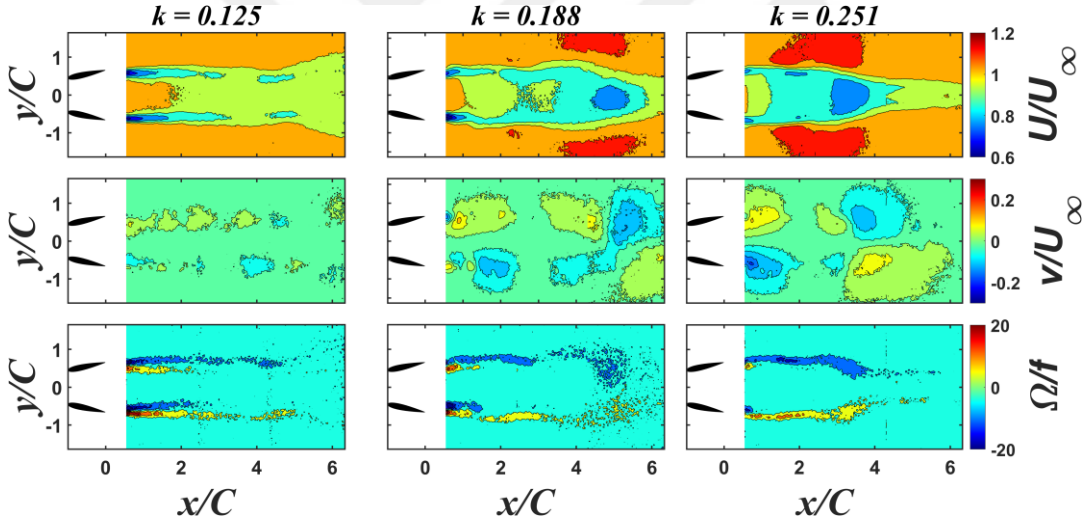


Figure 3.23: Comparison of the stream-wise and transverse gust ratio and vorticity for different reduced frequencies (k=0.125, k=0.188, and k=0.251) at the same deflection angle $\theta = -12°$ for out-of-phase case

CHAPTER 4

CONCLUSIONS AND FUTURE WORK

This thesis study summarizes the results of a near wake flow field characterization of a two vane gust generator with utilizing the experiments in a suction type wind tunnel. Firstly, a 3D active turbulence grid is designed for a suction type wind tunnel with 1.0 x 1.0 m^2 test section in RÜZGEM. Later, motor sizing for the active grid system is conducted and motion controller system is implemented. After all, a 2D active grid or so-called a gust generator with a NACA0015 airfoil type vanes is designed, manufactured and integrated to another suction type wind tunnel with 34 x 34 cm^2 test section to generate continuous sinusoidal gust experimentally. The selected motor for the 3D active grid is used in the gust generator.

The goal of the study is investigating the effects of the in-phase and out-of-phase sinusoidal motion on the gust characteristics of the two gust vanes with varying angle of deflections and reduced frequencies, in terms of angle of incidence, stream-wise gust ratio, transverse gust ratio, and vorticity for the gust generator system. Motion of the gust generator vanes is driven by encoder servo motors with a torque of 1.27 Nm. Phase-locked 2D2C PIV measurements are performed for different sinusoidal motion profiles in the wake of the gust generator vanes covering a region starting from 0.52 chords up to 6.2 chords downstream position starting from the trailing edge of the gust vanes. Phase locked PIV laser is triggered at each angle of 4° in period of each sinusoidal motion. At each phase angle, 100 number of image pair is taken. In the analysis part, effect of two different parameters is investigated on the gust characteristics of gust for in-phase and out-of-phase motions which are reduced frequency and maximum angle of deflection. To investigate the effect of increasing reduced frequencies, freestream velocity is set to 10 m/s and gust vanes is rotated at three different reduced frequencies, which are k = 0.13, 0.19 and 0.25 for maximum deflection angle of 12°. Later, to investigate the effect of increasing maximum

deflection angle, freestream velocity is set to 10 m/s and gust vanes is rotated at three different angles of deflection, which are $\theta = 8^\circ$, 12° and 16° for the reduced frequency, *k* of 0.25. In this case, maximum deflection angle of 16° is selected to see the effect of separation on the gust characteristics in terms of vorticity. To investigate the gust characteristics of the flow field parameters of angle of incidence, longitudinal and lateral gust ratios are examined at the x/c=0.6 and x/c=6 downstream locations in between the two vanes to see the near wake and the far wake gust characteristics.

The key findings of the study are listed below:

- A sinusoidal variation of the transverse gust ratio and the angle of incidence is observed by the motion of the in-phase case.
- Even in the near wake of the gust vanes, the in-phase motion of the gust vanes provides a continuous sinusoidal gust with a well-defined profile.
- The in-phase motion of the gust vanes produces a more-or-less constant stream-wise velocity in the near wake, which is slightly higher than the free-stream velocity, regardless of the pitching amplitude and reduced frequency. The difference is due to the flow being accelerated due to the blockage created by the gust vanes. The out-of-phase motion of the vanes, on the other hand, results in significant fluctuations in the stream-wise gust ratio.
- There is a dominant effect of the vorticity at the centerline of the test section due to strong vortices separating from the airfoils for both in-phase and out-of-phase cases. Especially, the separation of the flow is much stronger for the pitching amplitude of 16° which is above the stall angle for the NACA0015 airfoils. The vortices due to the separated flow causes sudden changes of the sinusoidal profile of the gust parameters in temporal results.
- There is a symmetry of the flow field observed from contour plots at negative and positive deflection angles of the vanes for the motion in the in-phase case.

- Increasing the pitching angle has a stronger effect than increasing the reduced frequency on the gust parameters in the near-wake region.
- Temporal results of the gust ratio or the angle of incidence parameters in the far wake (x/C = 6) have a phase lag compared to the near wake (x/C = 0.6) location in a period of time. Although the amplitude of the sine function of these parameters decreased slightly as it progressed in the far wake, damping of the profile is not observed in temporal results.

As a result of the study there are some recommendations for future works:

- The validation of the 3D active turbulence grid integrated into the wind tunnel can be done by using hotwire and PIV measurements.
- The effect of the same motion profiles applied to the gust generator on the gust characteristics of the wake region of the 3-D active grid can be investigated by means of gust parameters with the help of phase-locked 2D2C PIV measurements.
- To obtain high resolution results for a period of sinusoidal motion at high frequencies, high speed laser system can be used in a certain amount of time instead of phase-locked PIV system.
- Stereoscopic PIV measurements can be performed to observe the three dimensional effects on the near wake flow field of the active grid.
- The results of the active grid study can be compared with the gust generator flow field findings by PIV measurements.
- In addition to the sinusoidal motion of the gust vanes, different motion profiles can be applied to the gust generator and active grid systems such as 1-cos or $\sin^2$ profiles.
- The number of reduced frequencies can be increased and an empirical relation between the reduced frequency and angle of incidence or gust ratio can be investigated for gust generator and active grid systems.

REFERENCES

Armitt, J., Counihan, J. 1967. “The simulation of the atmospheric boundary layer in a wind tunnel”, Atmospheric Environment, 2(1), 49-71.

Buell, D. A., 1969, "An Experimental Investigation of the Velocity Fluctuations behind Oscillating Vanes," TN D-5543, NASA.

Beal TR. 1993. Digital simulation of atmospheric turbulence for Dryden and von Kármán models. J. Guid. Control Dyn. 16(1):132–38.

Cekli, H. E., van de Water, W. 2010. “Tailoring turbulence with an active grid”, Experiments in Fluids, 49(2), 409-416.

Brossard, C., Monnier, J. C., Barricau, P., Vandernoot, F. X., Le Sant, Y., Champagnat, F., & Le Besnerais, G. (2009). Principles and applications of particle image velocimetry.

Cekli, H. E. 2011. How to stir turbulence. Phd Thesis, Eindhoven Technical University.

Comte-Bellot, G., Corrsin, S. 1966. “The use of a contraction to improve the isotropy of grid-generated turbulence”, Journal of Fluid Mechanics, 25(4), 657-682.

Cook, N. J. 1973. “On simulating the lower third of the urban adiabatic boundary layer in a wind tunnel”, Atmospheric Environment (1967), 7(7), 691-705.

Cook, N. J. 1978. “Wind-tunnel simulation of the adiabatic atmospheric boundary layer by roughness, barrier and mixing-device methods”, Journal of Wind Engineering and Industrial Aerodynamics, 3(2-3), 157-176.

Counihan, J. 1973. “Simulation of an adiabatic urban boundary layer in a wind tunnel”, Atmospheric Environment (1967), 7(7), 673-689.

Gad-el-Hak, M., Corrsin, S. 1974. “Measurements of the nearly isotropic turbulence behind a uniform jet grid”, Journal of Fluid Mechanics, 62(1), 115-143.

Gan L., Krogstad P.A., Evolution of turbulence and in-plane vortices in the near field flow behind multi-scale planar grids, Phys. Fluids. 28 (2016). doi:10.1063/1.4960025.

Harold N. Murrow and Kermit G. Pratt nad John C. Houbolt. 1989. Naca/nasa research related to evolution of u.s. gust design criteria. In AIAA, ASME, ASCE, AHS, and ASC, Structures, Structural Dynamics and Materials Conference; 30th; Apr. 3-5, 1989; Mobile, AL; United States.

Irwin, H. P. A. H. 1981. “The design of spires for wind simulation”, Journal of Wind Engineering and Industrial Aerodynamics 7(3), 361-366.

Isaza, J. C., Salazar, R., Warhaft, Z. 2014. “On grid-generated turbulence in the near- and far field regions”, Journal of Fluid Mechanics, 753, 402–426.

Jones AR, Cetiner O. 2021. Overview of unsteady aerodynamic response of rigid wings in gust encounters. AIAA J. 59(2):731–36.

Knebel, P., Kittel, A., Peinke, J. 2011. “Atmospheric wind field conditions generated by active grids”, Experiments in Fluids, 51(2), 471-481.

Lancelot, P.M.G.J., Sodja, J., Richardson, Werter, N.P.M., and De Breuker, R. 2015. Design and testing of a low subsonic wind tunnel gust generator, Proceedings of IFASD 2015, International Forum on Aeroelasticity and Structural Dynamics, June 28 - July 02, 2015.

Larssen, J. V., Devenport, W. J. 2011. “On the generation of large-scale homogeneous turbulence”, Experiments in Fluids, 50(5), 1207-1223.

Ling, S. C., Wan, C. A. 1972. “Decay of isotropic turbulence generated by a mechanically agitated grid”, The Physics of Fluids, 15(8), 1363-1369.

Makita, H. 1991. “Realization of a large-scale turbulence field in a small wind tunnel”, Fluid Dynamics Research, 8(1-4), 53.

Makita, H., Sassa, K. 1991. “Active turbulence generation in a laboratory wind tunnel”. Advances in Turbulence 3. Editors: Johansson, A.V., Alfredsson, P.H. Berlin, Heidelberg: Springer.

Mydlarski, L. 2017. “A turbulent quarter century of active grids: from Makita (1991) to the present”, Fluid Dynamics Research, 49(6), 061401.

Neuhaus, L., Berger, F., Peinke, J. Hölling, M. 2021. Exploring the capabilities of active grids. Exp Fluids **62,** 130. https://doi.org/10.1007/s00348-021-03224-5

Ozono, S., Nishi, A., Miyagi, H. 2006. “Turbulence generated by a wind tunnel of multi-fan type in uniformly active and quasi-grid modes”, Journal of Wind Engineering and Industrial Aerodynamics, 94(4).

Phillip Donely. Summary of information relating to gust loads on airplanes. Technical report, NASA, 1950.

Poorte, R. E. G., Biesheuvel, A. 2002. “Experiments on the motion of gas bubbles in turbulence generated by an active grid”, Journal of Fluid Mechanics, 461, 127-154.

Quinn, D. B., Watts, A., Nagle, T., Lentink, D. 2017. “A new low-turbulence wind tunnel for animal and small vehicle flight experiments”, Royal Society Open Science, 4(3), 160960.

Raffel, M., Willert, C. E., Scarano, F., Kähler, C. J., Wereley, S. T., Kompenhans, J. 2018. “Particle image velocimetry: a practical guide”, (3rd edition) Springer.

Rakib M.I., Evans S.P., Clausen P.D. 2019. “Measured gust events in the urban environment, a comparison with the IEC standard”. J. Phys.: Conf. Ser. 1452 012086.

IEC 61400.2-2013 Wind Turbines - Design Requirements for Small Wind Turbines, 2013.

Reynolds, O. 1883a. “An experimental investigation of the circumstances which determine whether the motion of water shall be direct or sinuous, and of the law of resistance in parallel channels”, Proceedings of the Royal Society of London, 35, 84–99.

Reynolds, O. 1883b. “An experimental investigation of the circumstances which determine whether the motion of water shall be direct or sinuous, and of the law of resistance in parallel channels”, Philosophical Transactions of the Royal Society of London, 174, 935–982.

Saddoughi, S. G., Veeravalli, S. V. 1994. “Local isotropy in turbulent boundary layers at high Reynolds number”, Journal of Fluid Mechanics, 268, 333-372.

Simmons, J. M., Platzer, M.F.. 1971. “Experimental Investigation of Incompressible Flow Past Airfoils with Oscillating Jet Flaps”, Journal of Aircraft. 8(8), 587-592

Srdic, A., Fernando, H. J. S., Montenegro, L. 1996. “Generation of nearly isotropic turbulence using two oscillating grids”, Experiments in Fluids, 20(5), 395-397.

Traphan, D., Wester, T. T. B., Peinke, J. & Gülker, G. 2018 On the aerodynamic behavior of an airfoil under tailored turbulent inflow conditions. In Proceedings of the 5th International Conference on Experimental Fluid Mechanics, Munich, Germany. Universität der Bundeswehr München.

Tennekes, H., Lumley, J. L. 1972. A First Course in Turbulence (1st edition). MIT press.

Thompson, S. M., Turner, J. S. 1975. "Mixing across an interface due to turbulence generated by an oscillating grid", Journal of Fluid Mechanics, 67(2), 349-368.

Thole, K. A., Bogard, D. G., Whan-Tong, J. L. 1994. "Generating high freestream turbulence levels", Experiments in Fluids, 17(6), 375-380.

Warhaft, Z. 2009. "Why we need experiments at high Reynolds numbers", Fluid Dynamics Research, 41(2), 021401.

Wei, N.J., Kissing, J., Wester, T.T.B., Wegt, S., Schiffmann, K., Jakirlic, S., Hölling, M., Peinke, J. and Tropea, C. 2019. Insights into the periodic gust response of airfoils, J Fluid Mech, Vol 876, p: 237-263, July 2019.

Wester, T.T.B., Krauss, J., Neuhaus, L., Hölling, A., Gülker, G., Hölling, M., Peinke, J. 2022. How to Design a 2D Active Grid for Dynamic Inflow Modulation. Flow Turbulence Combust 108**,** 955–972.

Wilmer H. Reed III. Aeroelasticity matters: Some reflections on two decades of testing in the nasa langley dynamics tunnel. In Intern. Symp. on Aeroelasticity; 5-7 Oct. 1980 - 1 Oct. 1981; Nuremberg; Germany, 1981.

Yigili, I., Andirin, M.A., Kurban E., Baskan, O., Percin, M., 2021 "Design and experimental investigation of a wind tunnel gust generator". Ankara International Aerospace Conference

Yigili, I., Andirin, M.A., Akpolat M.T., Baskan, O., Percin, M., Uzol, O., 2022, Design of a gust generator and comparison of model wind turbine and porous disc wake flows in a transverse gust, J. Phys.: Conf. Ser. 2265 022108

APPENDICES

A. Contour plots for all the test cases

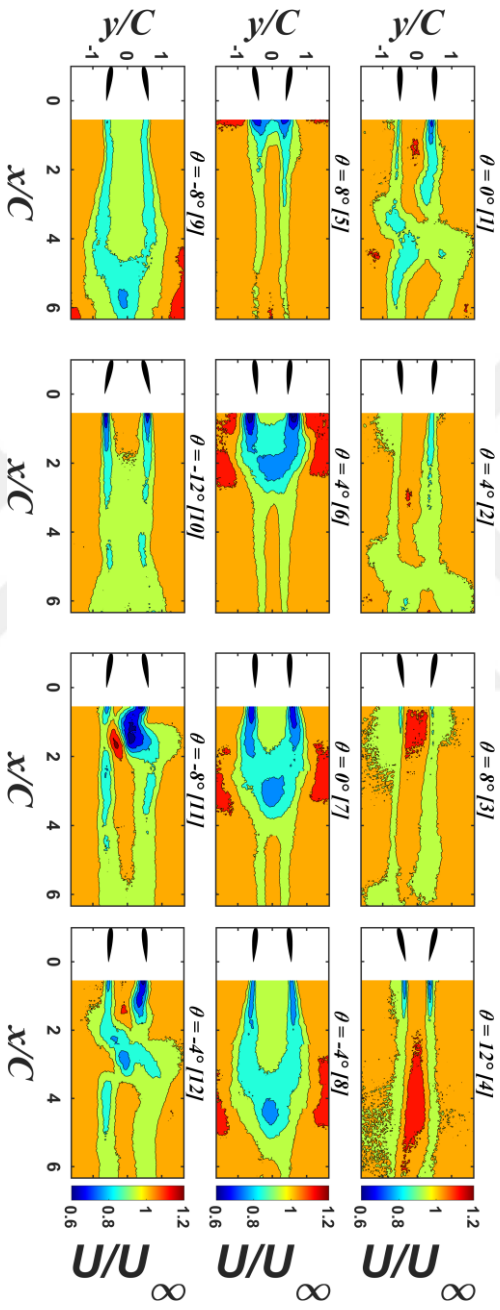


Figure A.1: Stream-wise Gust ratio contour plots of FOV for reduced frequency k = 0.125 and with a maximum amplitude of $\bar{\theta} = 12^{\circ}$ out-of-phase case at different phase angles

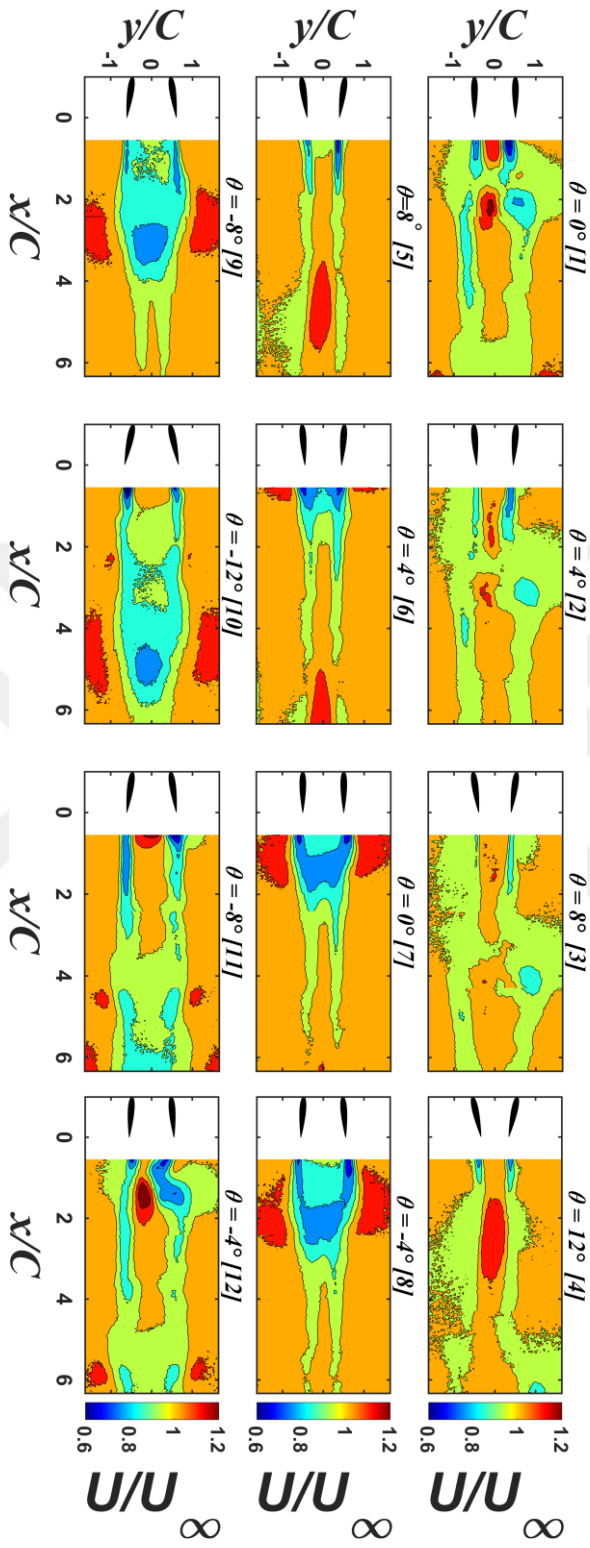


Figure A.2: Stream-wise Gust ratio contour plots of FOV for reduced frequency k = 0.188 and with a maximum amplitude of $\bar{\theta} = 12^{\circ}$ out-of-phase case at different phase angles

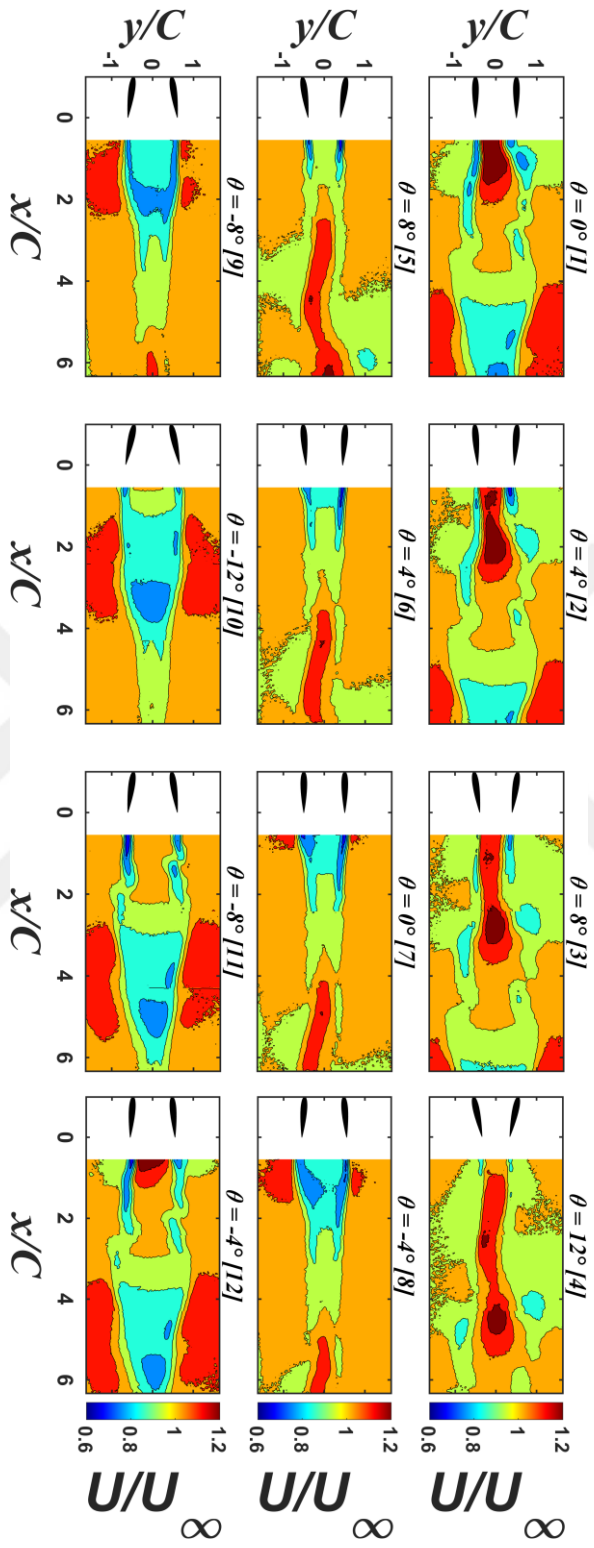


Figure A.3: Stream-wise Gust ratio contour plots of FOV for reduced frequency k = 0.251 and with a maximum amplitude of $\bar{\theta} = 12^{\circ}$ out-of-phase case at different phase angles

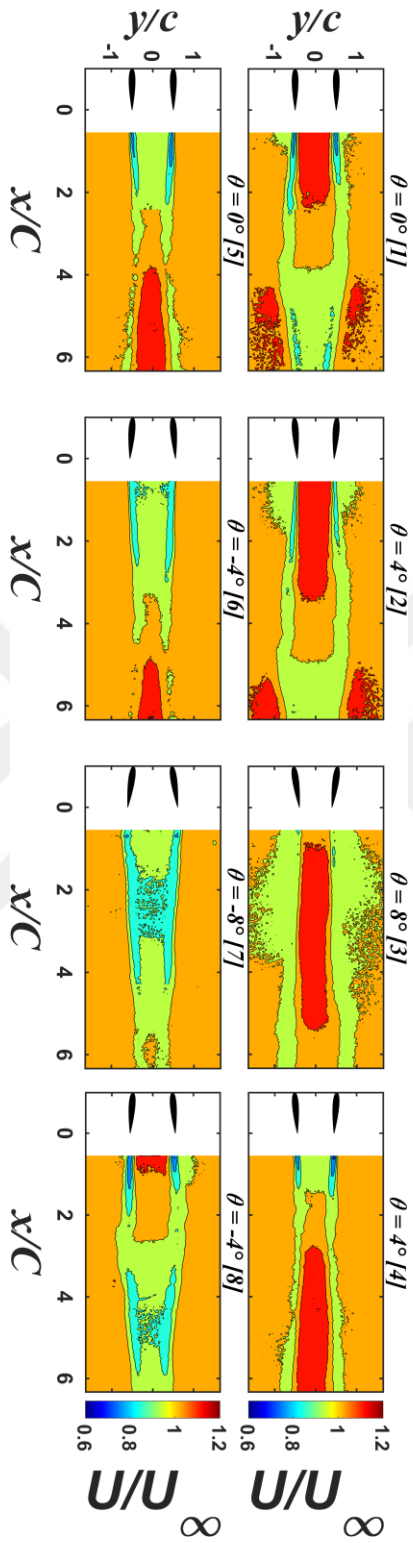


Figure A.4: Stream-wise Gust ratio contour plots of FOV for reduced frequency k = 0.251 and with a maximum amplitude of $\bar{\theta} = 8^{\circ}$ out-of-phase case at different phase angles

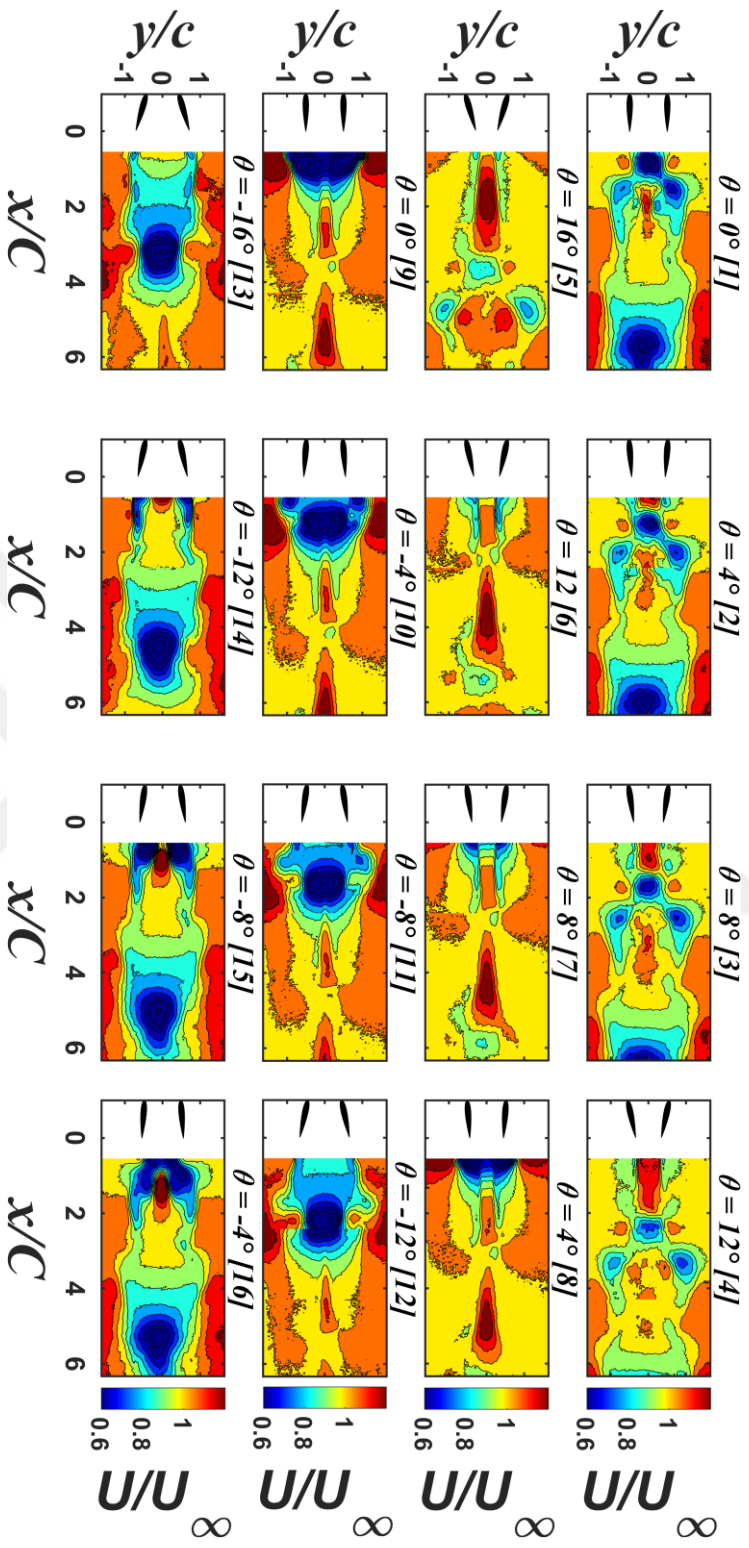


Figure A.5: Stream-wise Gust ratio contour plots of FOV for reduced frequency k = 0.251 and with a maximum amplitude of $\bar{\theta} = 16^{\circ}$ out-of-phase case at different phase angles

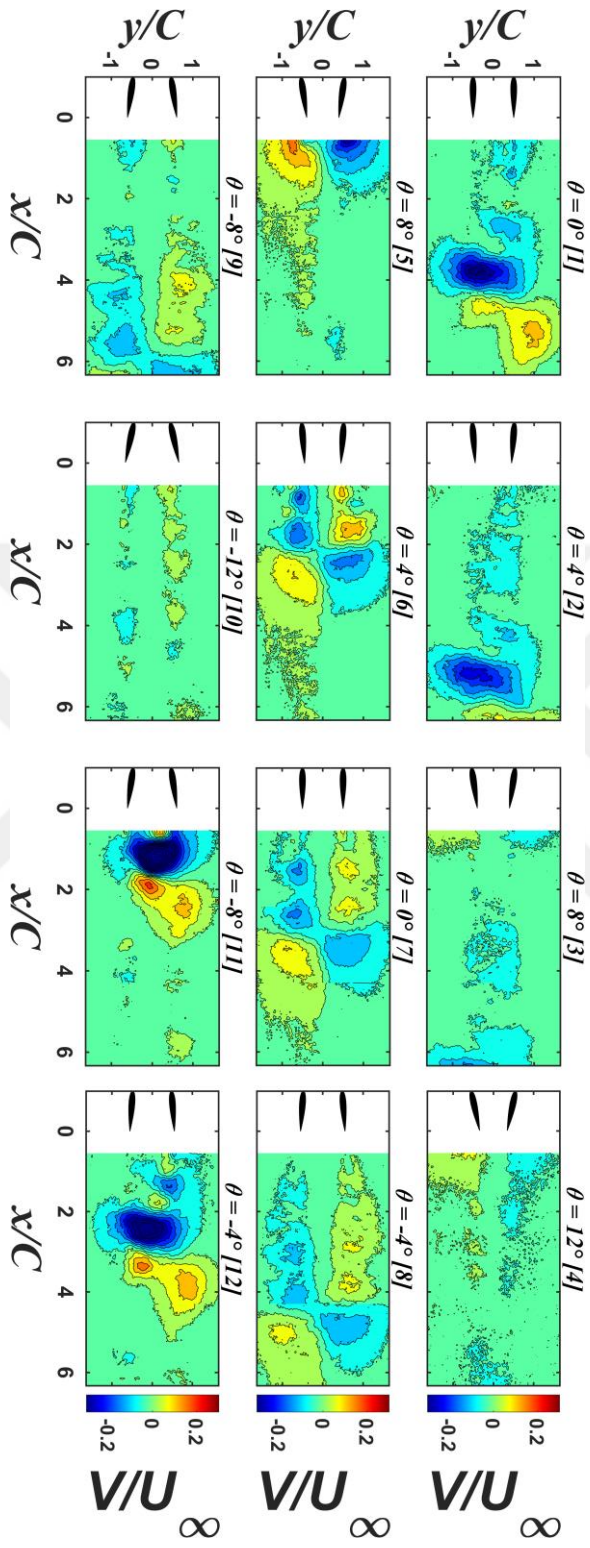


Figure A.6: Transverse Gust ratio contour plots of FOV for reduced frequency k = 0.125 and with a maximum amplitude of $\bar{\theta} = 12^{\circ}$ out-of-phase case at different phase angles

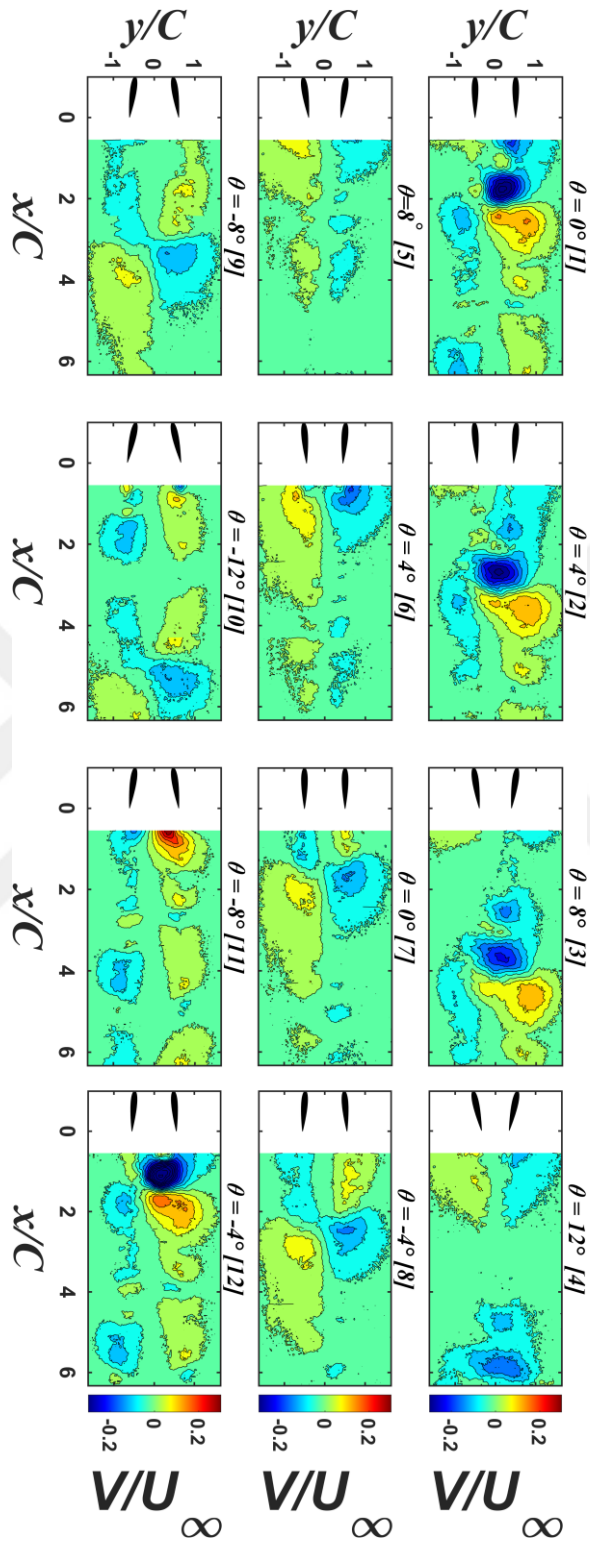


Figure A.7: Transverse Gust ratio contour plots of FOV for reduced frequency k = 0.188 and with a maximum amplitude of $\bar{\theta} = 12^{\circ}$ out-of-phase case at different phase angles

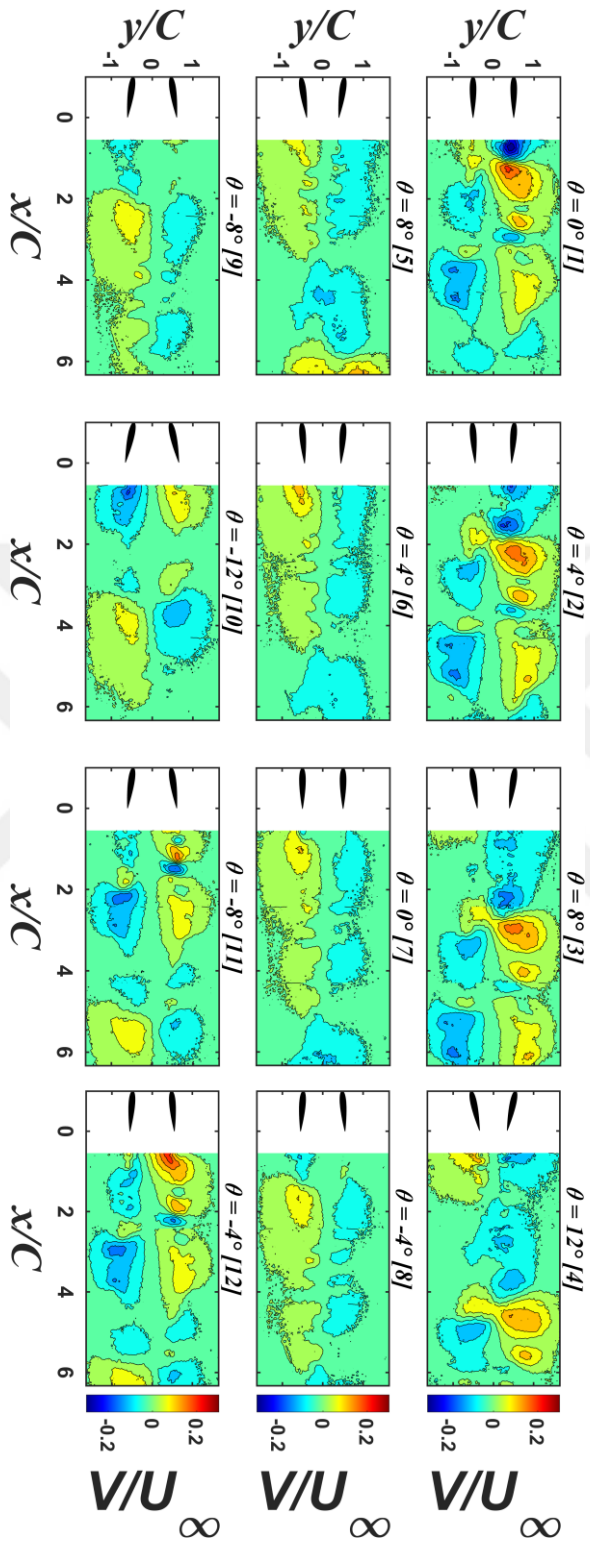


Figure A.8: Transverse Gust ratio contour plots of FOV for reduced frequency k = 0.251 and with a maximum amplitude of $\bar{\theta} = 12^{\circ}$ out-of-phase case at different phase angles

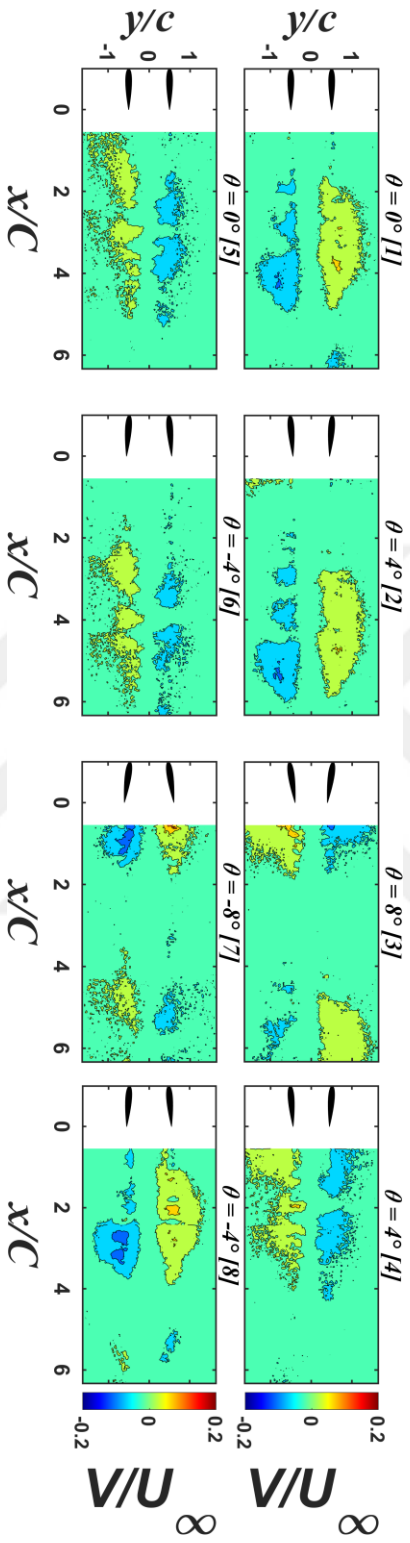


Figure A.9: Transverse Gust ratio contour plots of FOV for reduced frequency k = 0.251 and with a maximum amplitude of $\bar{\theta} = 8^{\circ}$ out-of-phase case at different phase angles

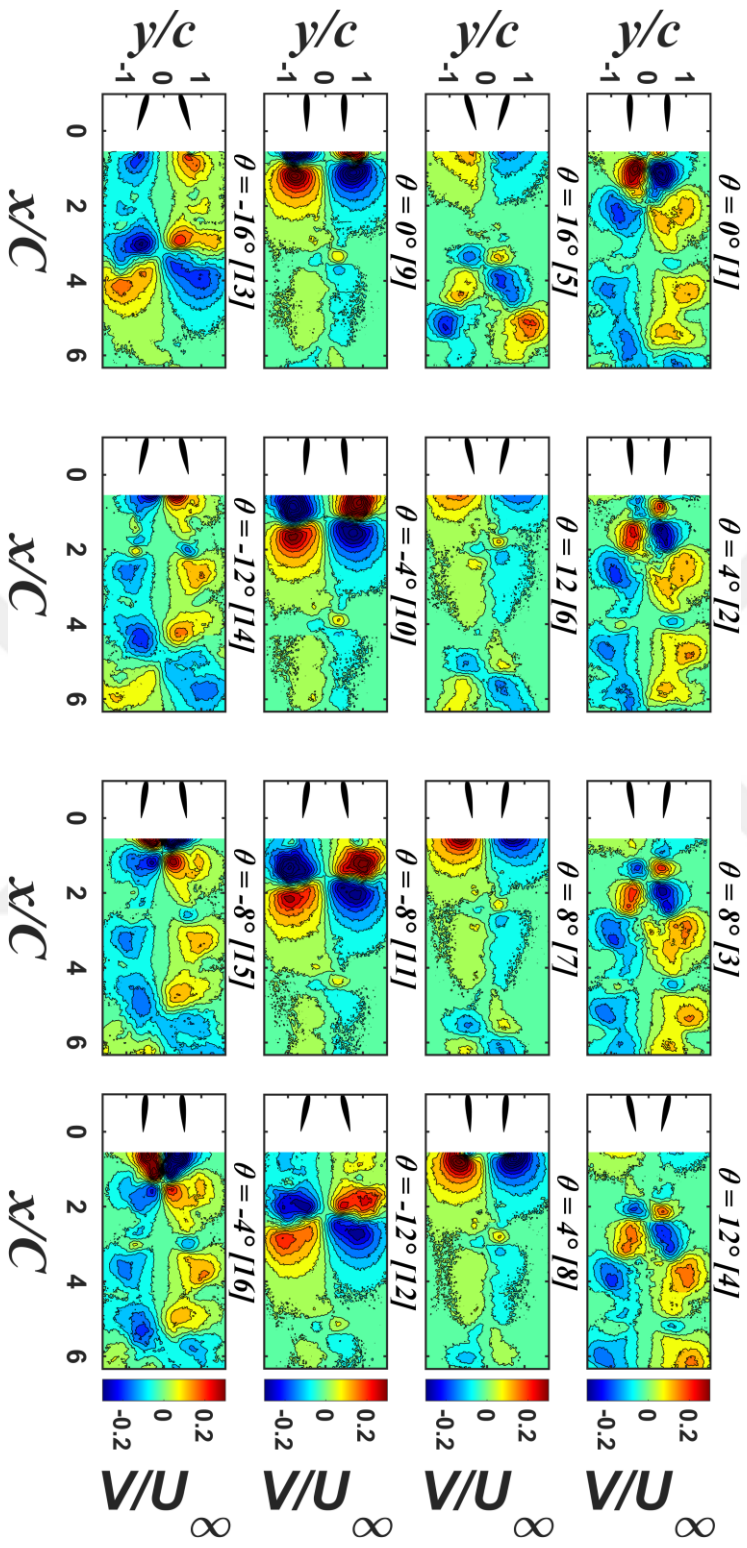


Figure A.10: Transverse Gust ratio contour plots of FOV for reduced frequency k = 0.251 and with a maximum amplitude of $\bar{\theta} = 16^{\circ}$ out-of-phase case at different phase angles

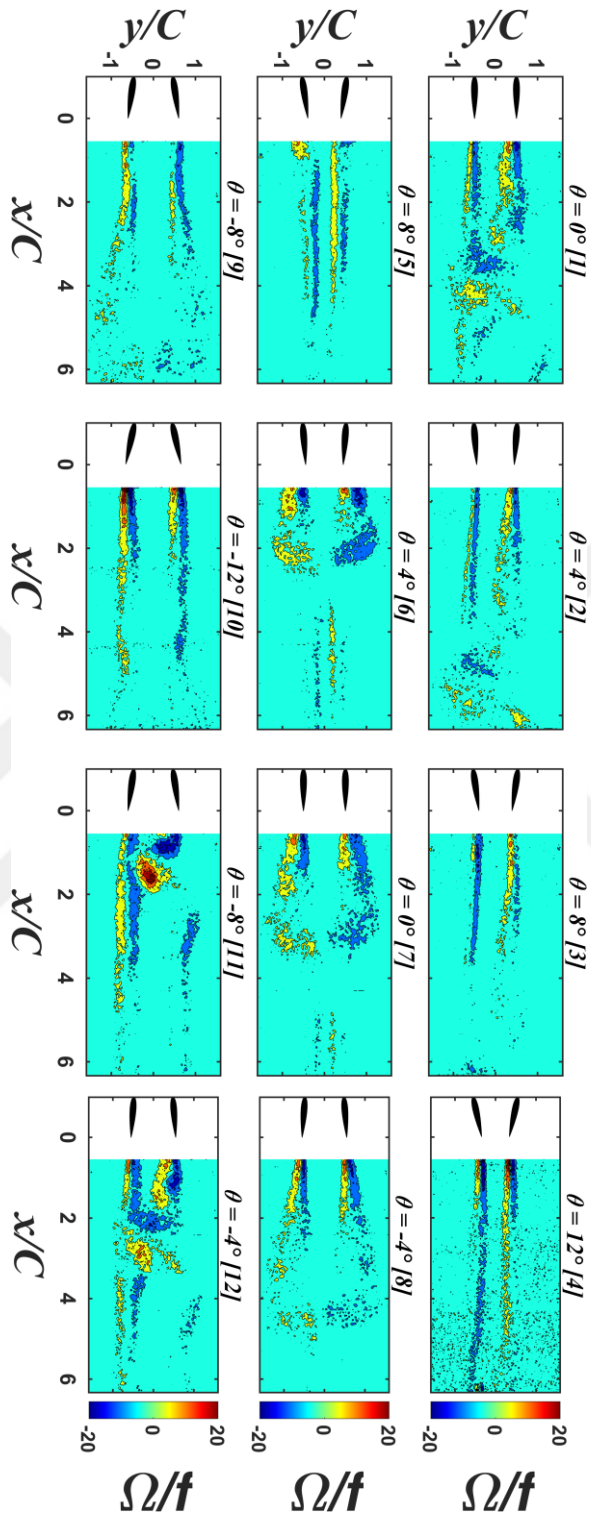


Figure A.11: Vorticity contour plots of FOV for reduced frequency $k = 0.125$ and with a maximum amplitude of $\bar{\theta} = 12^{\circ}$ out-of-phase case at different phase angles

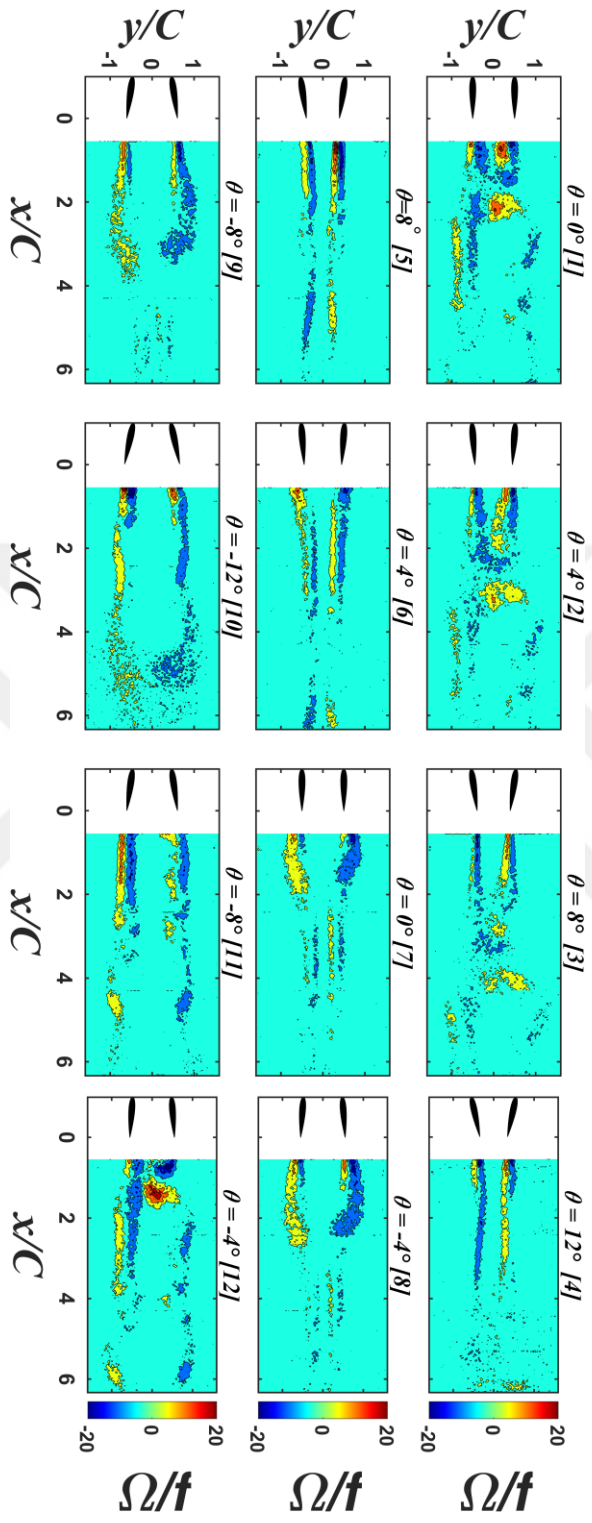


Figure A.12: Vorticity contour plots of FOV for reduced frequency $k = 0.188$ and with a maximum amplitude of $\bar{\theta} = 12^{\circ}$ out-of-phase case at different phase angles

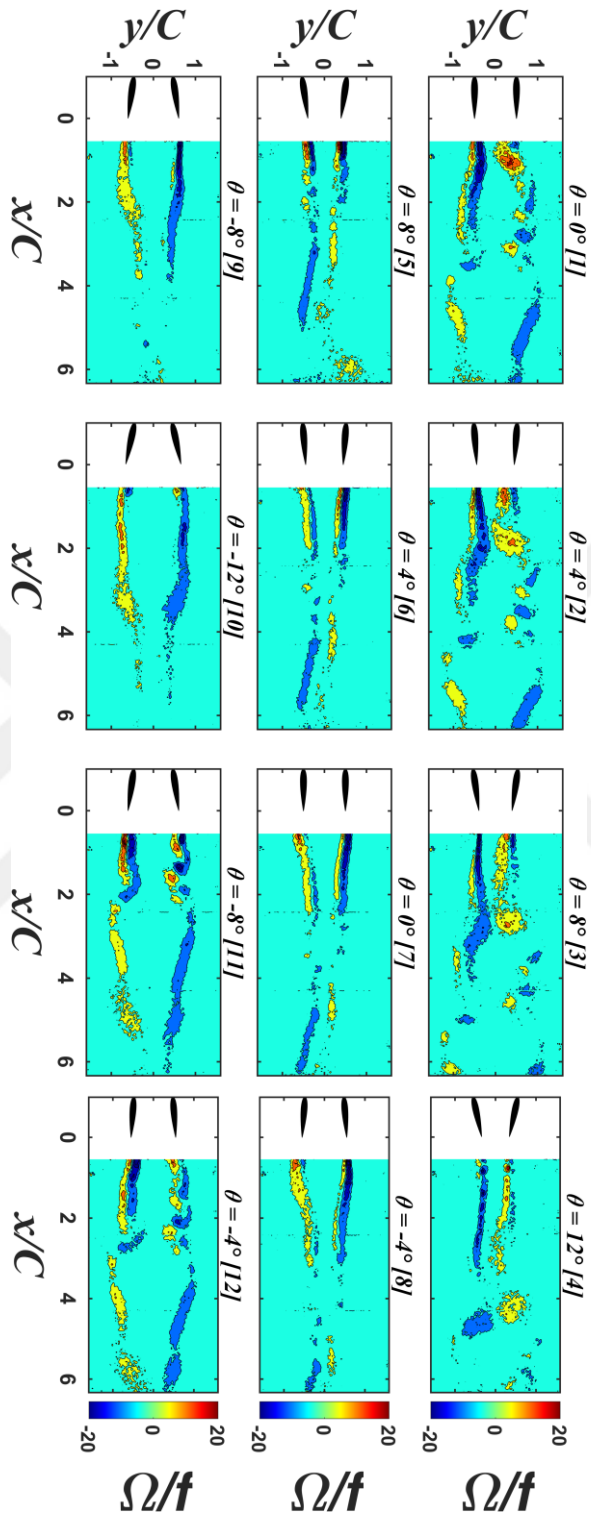


Figure A.13: Vorticity contour plots of FOV for reduced frequency $k = 0.251$ and with a maximum amplitude of $\bar{\theta} = 12^{\circ}$ out-of-phase case at different phase angles

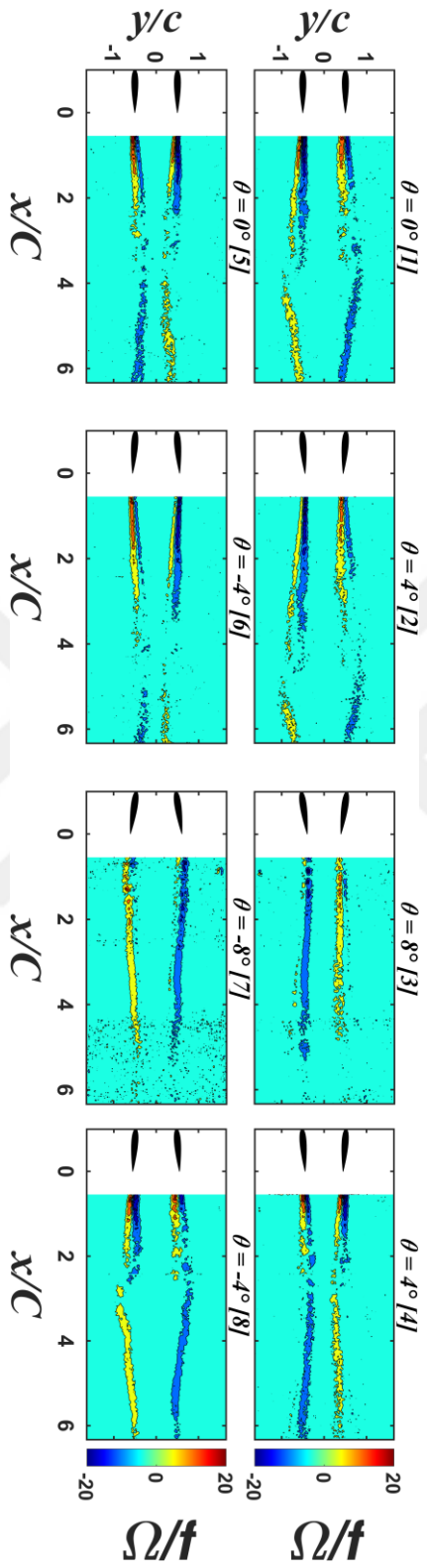


Figure A.14: Vorticity contour plots of FOV for reduced frequency k = 0.251 and with a maximum amplitude of $\bar{\theta} = 8^{\circ}$ out-of-phase case at different phase angles

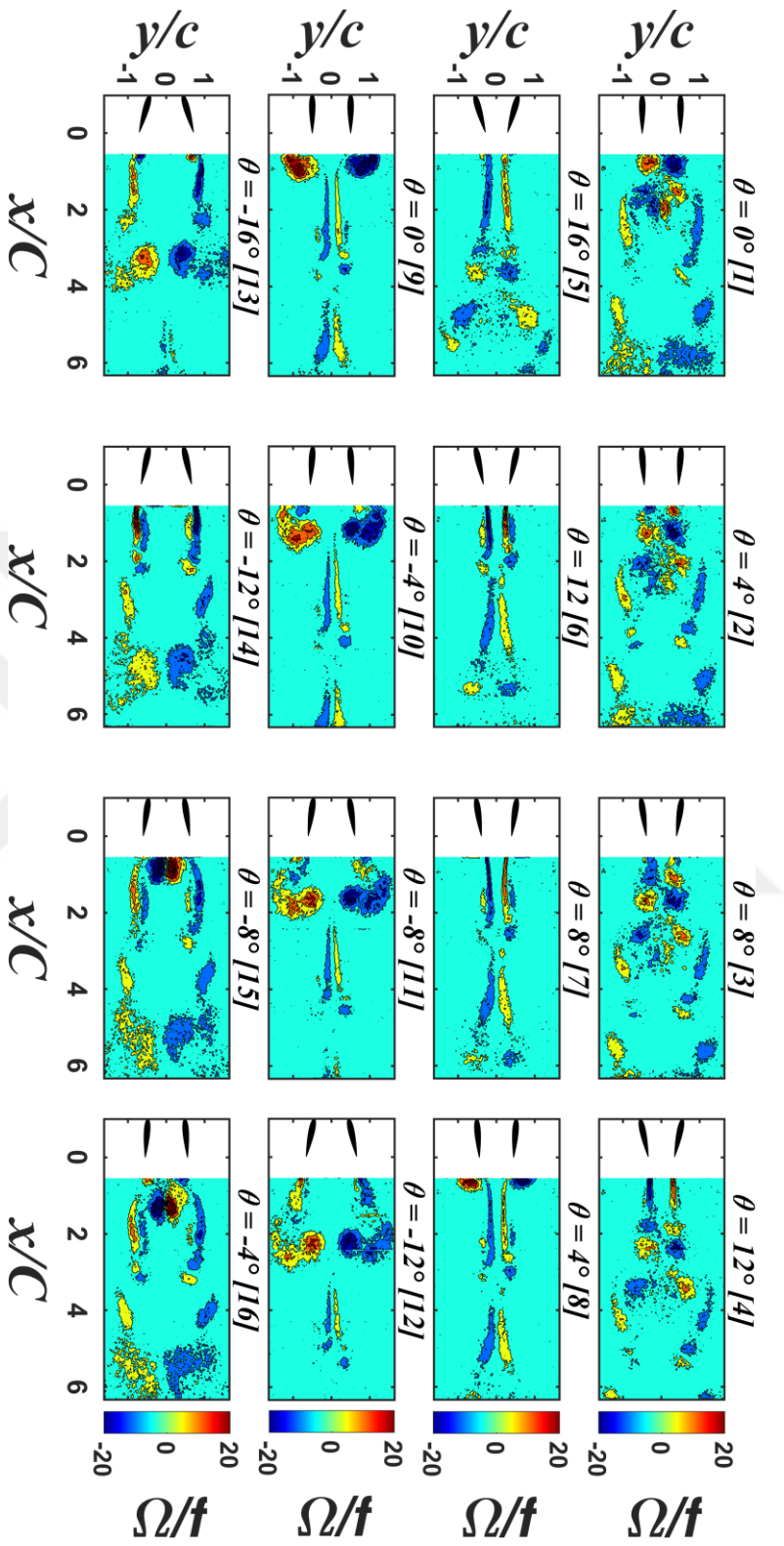


Figure A.15: Vorticity contour plots of FOV for reduced frequency k = 0.251 and with a maximum amplitude of $\bar{\theta} = 16^{\circ}$ out-of-phase case at different phase angles

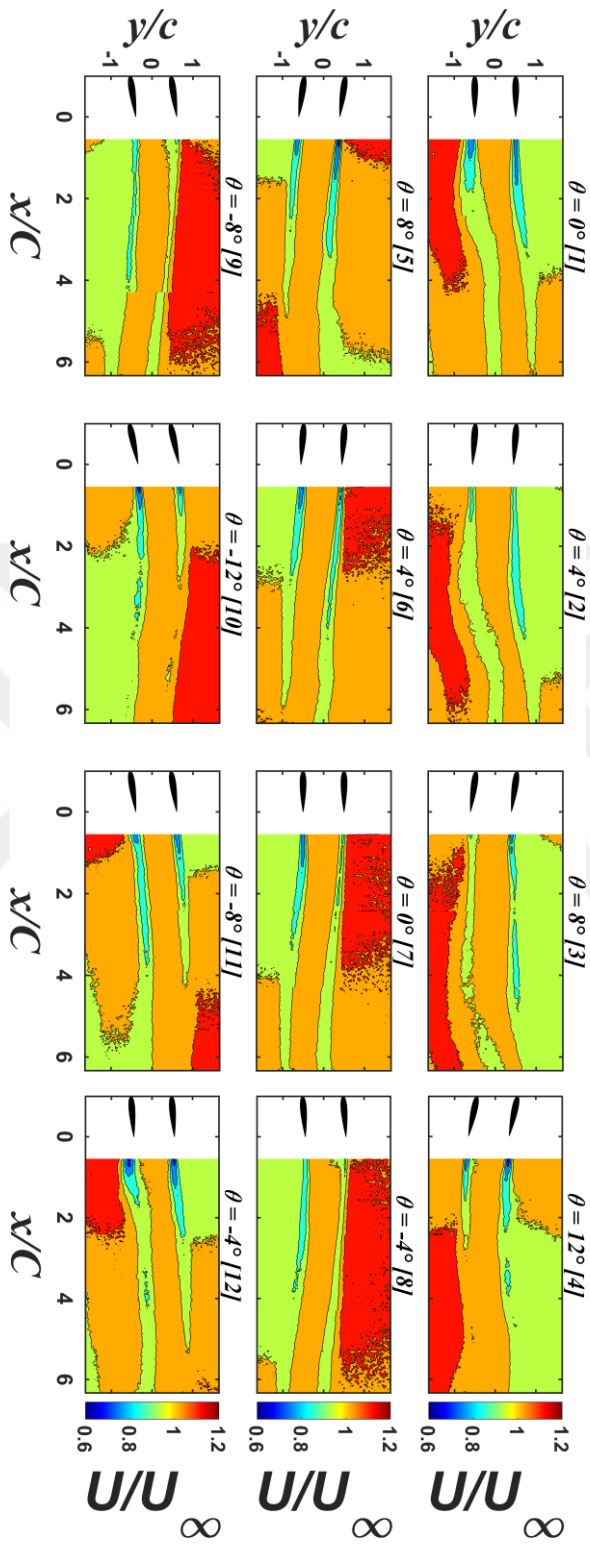


Figure A.16: Stream-wise Gust ratio contour plots of FOV for reduced frequency k = 0.125 and with a maximum amplitude of $\bar{\theta} = 12^{\circ}$ in-phase case at different phase angles

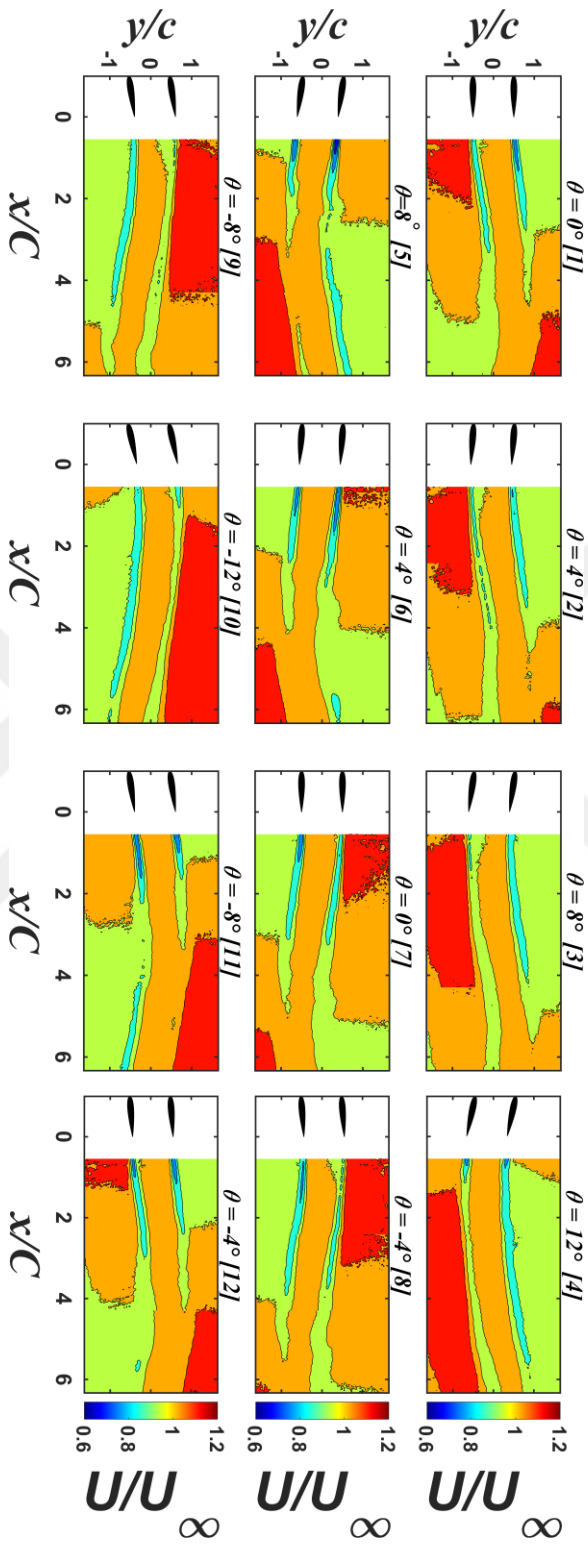


Figure A.17: Stream-wise Gust ratio contour plots of FOV for reduced frequency k = 0.188 and with a maximum amplitude of $\bar{\theta} = 12^{\circ}$ in-phase case at different phase angles

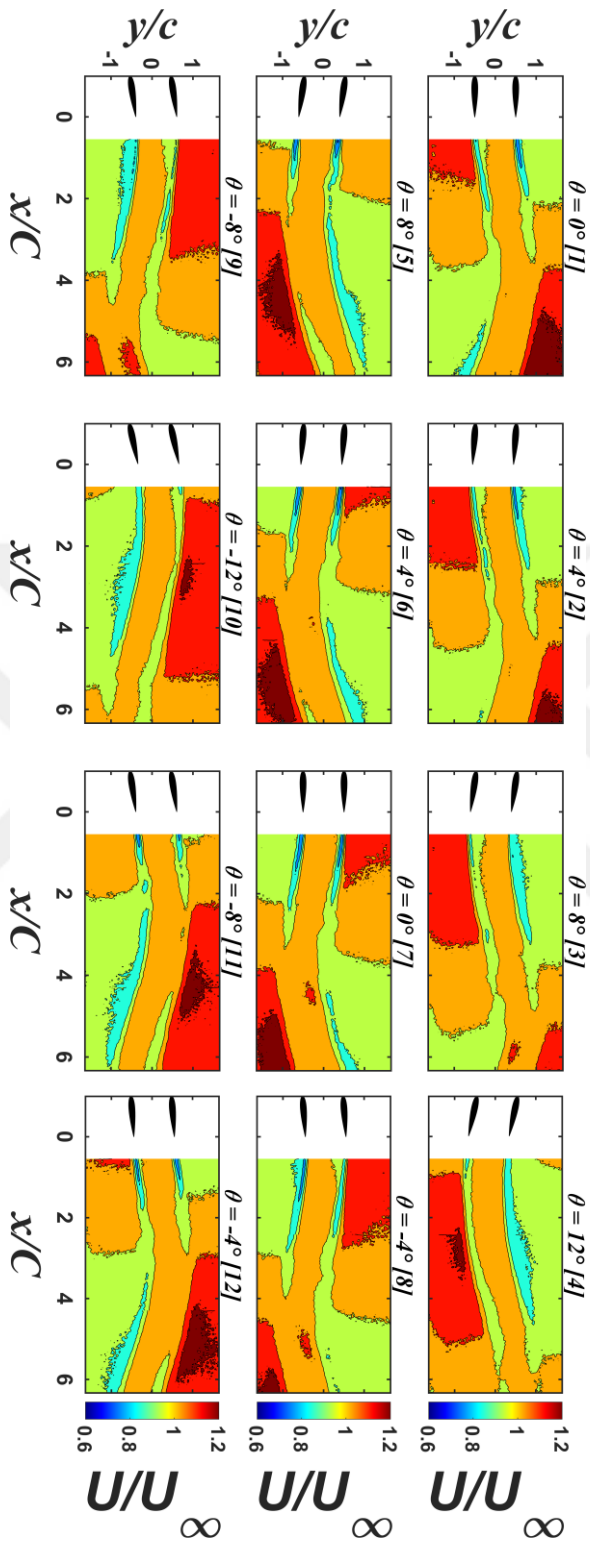


Figure A.18: Stream-wise Gust ratio contour plots of FOV for reduced frequency *k* = 0.251 and with a maximum amplitude of $\bar{\theta} = 12^{\circ}$ in-phase case at different phase angles

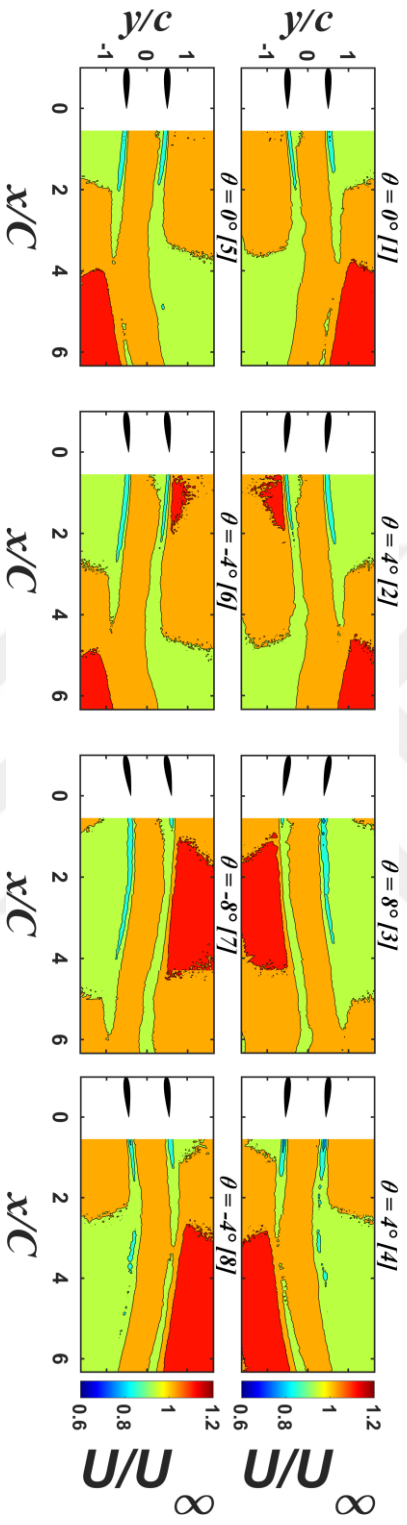


Figure A.19: Stream-wise Gust ratio contour plots of FOV for reduced frequency k = 0.251 and with a maximum amplitude of $\bar{\theta} = 8^{\circ}$ in-phase case at different phase angles

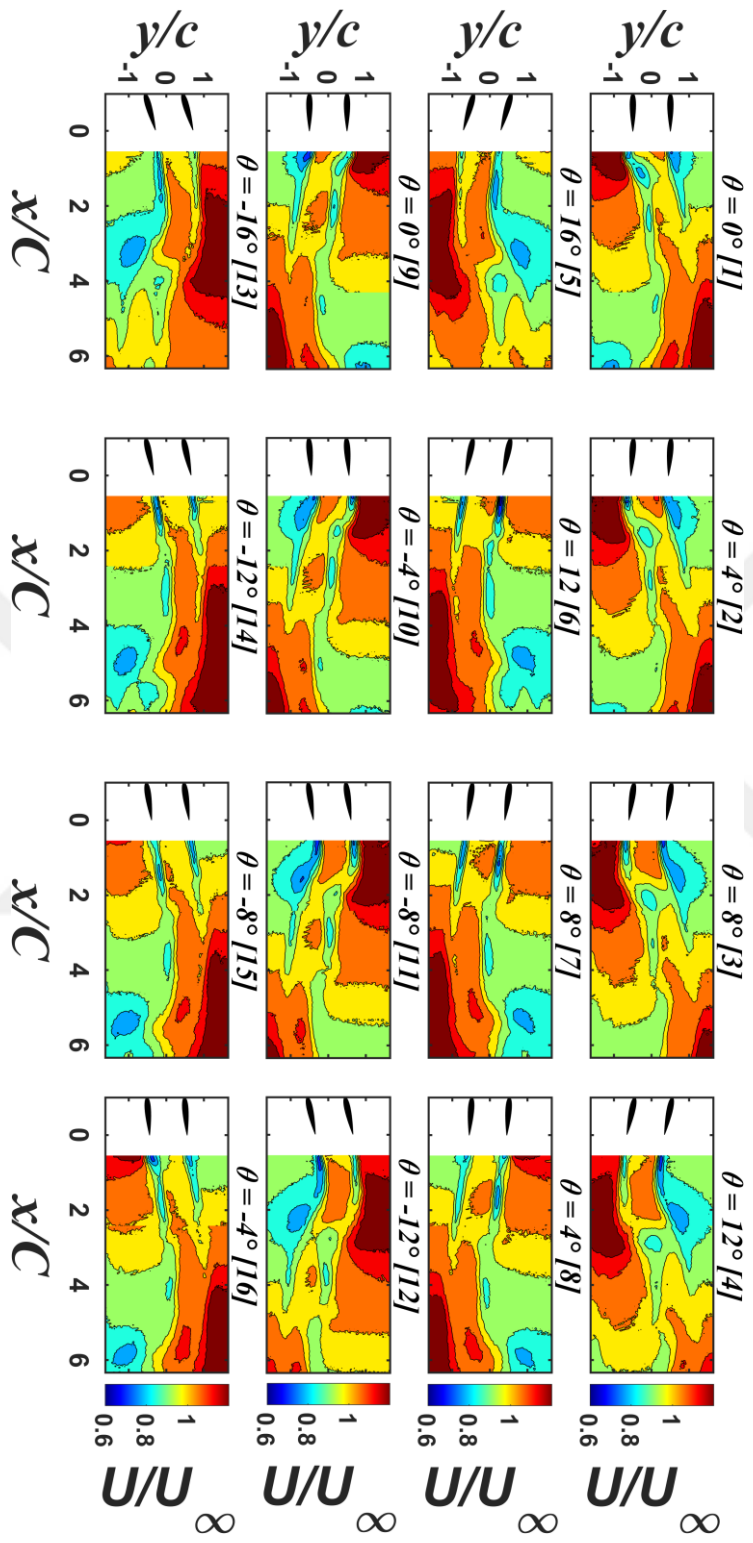


Figure A.20: Stream-wise Gust ratio contour plots of FOV for reduced frequency k = 0.251 and with a maximum amplitude of $\bar{\theta} = 16^{\circ}$ in-phase case at different phase angles

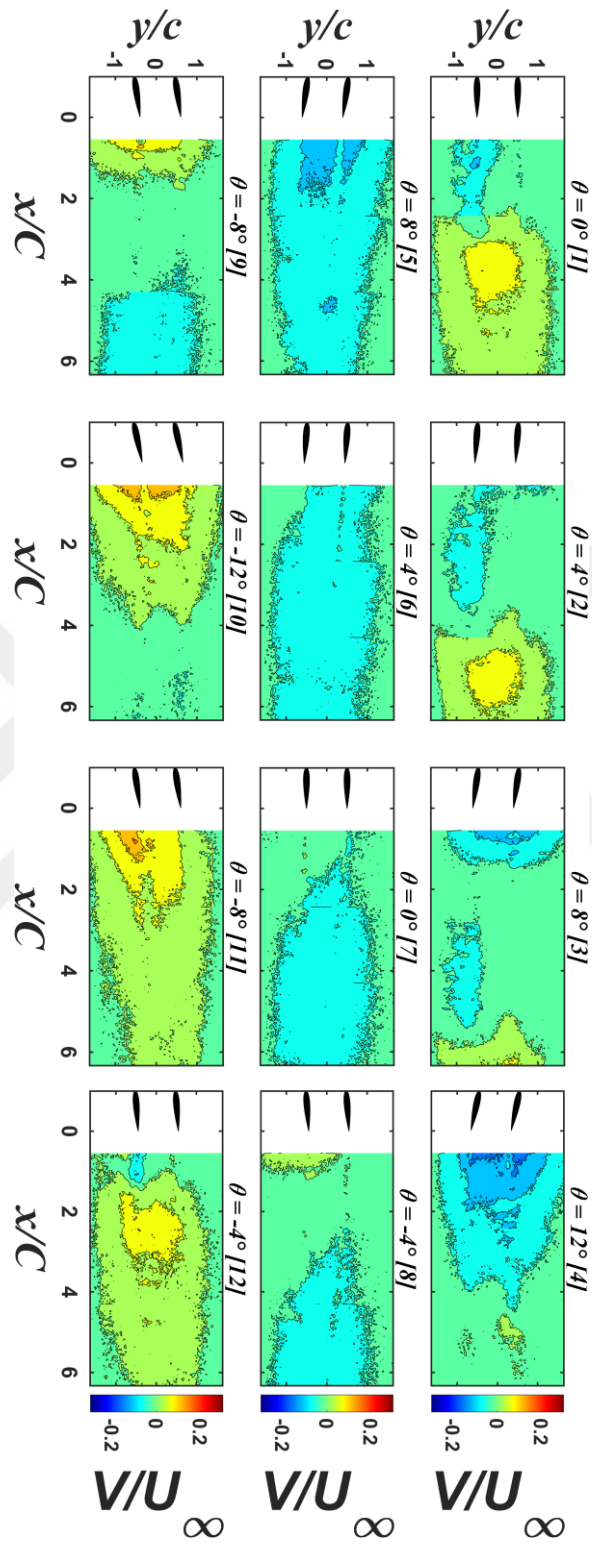


Figure A.21: Transverse Gust ratio contour plots of FOV for reduced frequency k = 0.125 and with a maximum amplitude of $\bar{\theta} = 12^{\circ}$ in-phase case at different phase angles

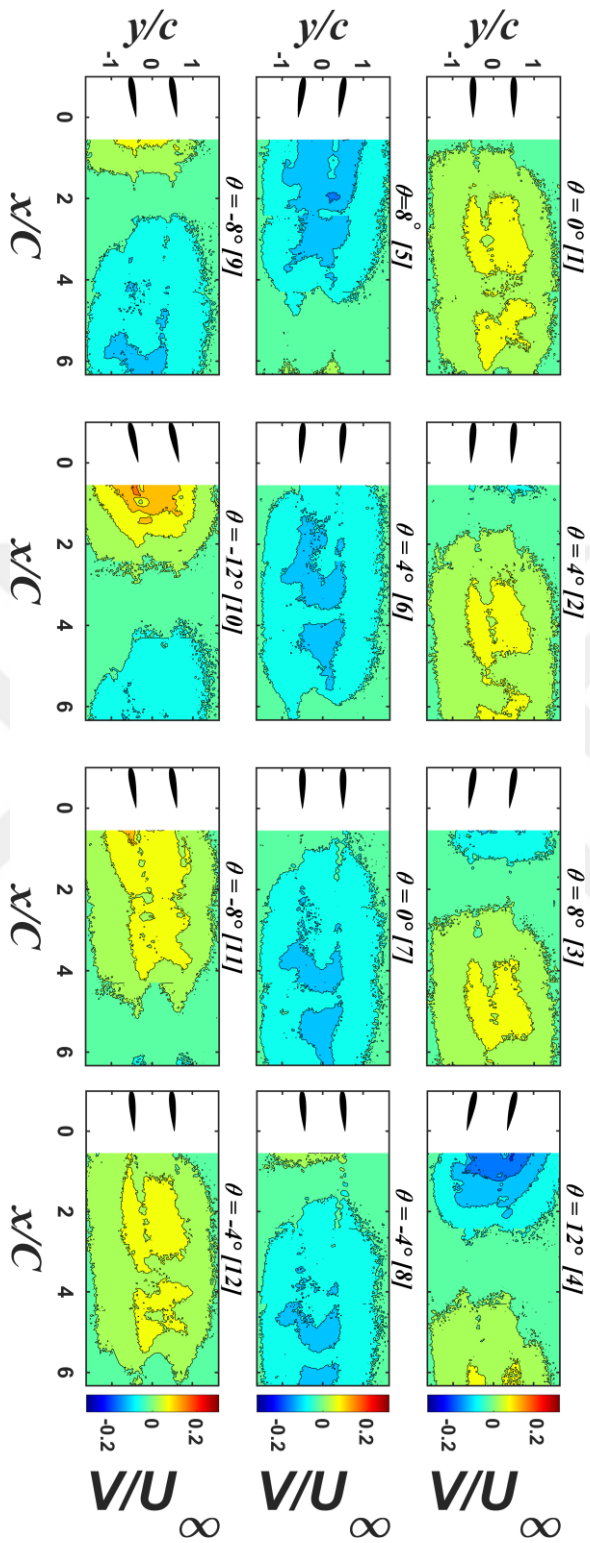


Figure A.22: Transverse Gust ratio contour plots of FOV for reduced frequency k = 0.188 and with a maximum amplitude of $\bar{\theta} = 12^{\circ}$ in-phase case at different phase angles

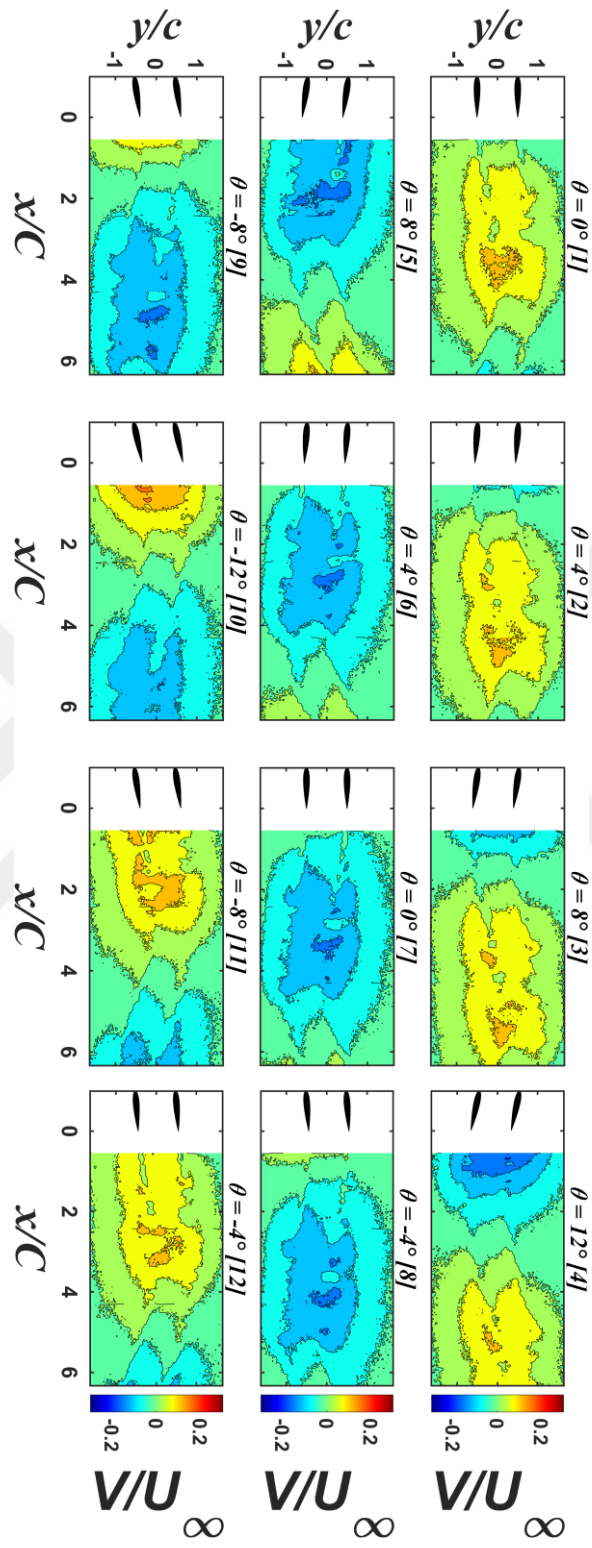


Figure A.23: Transverse Gust ratio contour plots of FOV for reduced frequency k = 0.251 and with a maximum amplitude of $\bar{\theta} = 12^{\circ}$ in-phase case at different phase angles

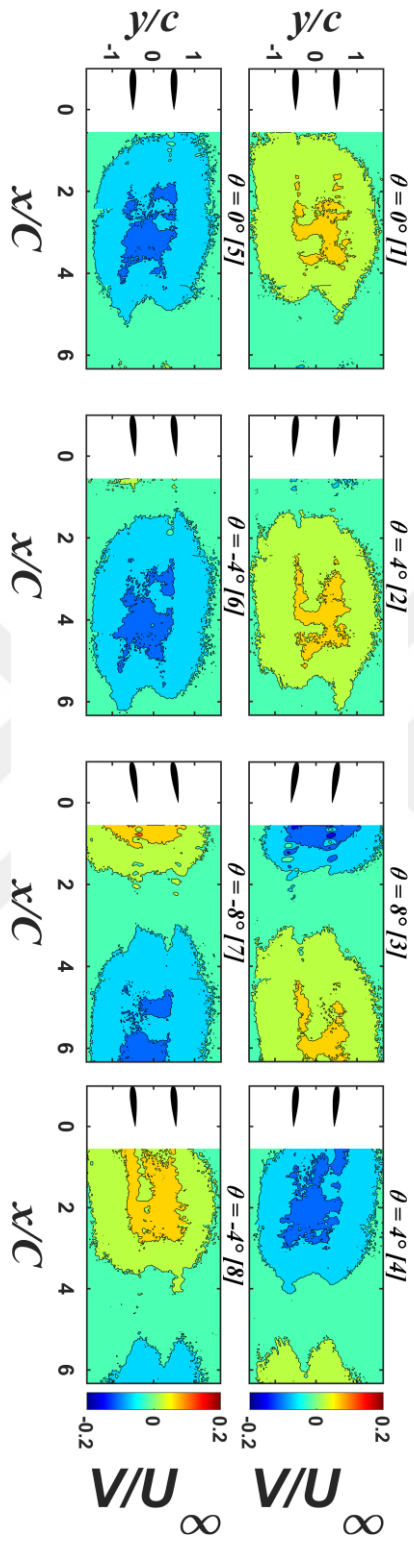


Figure A.24: Transverse Gust ratio contour plots of FOV for reduced frequency k = 0.251 and with a maximum amplitude of $\bar{\theta} = 8^{\circ}$ in-phase case at different phase angles

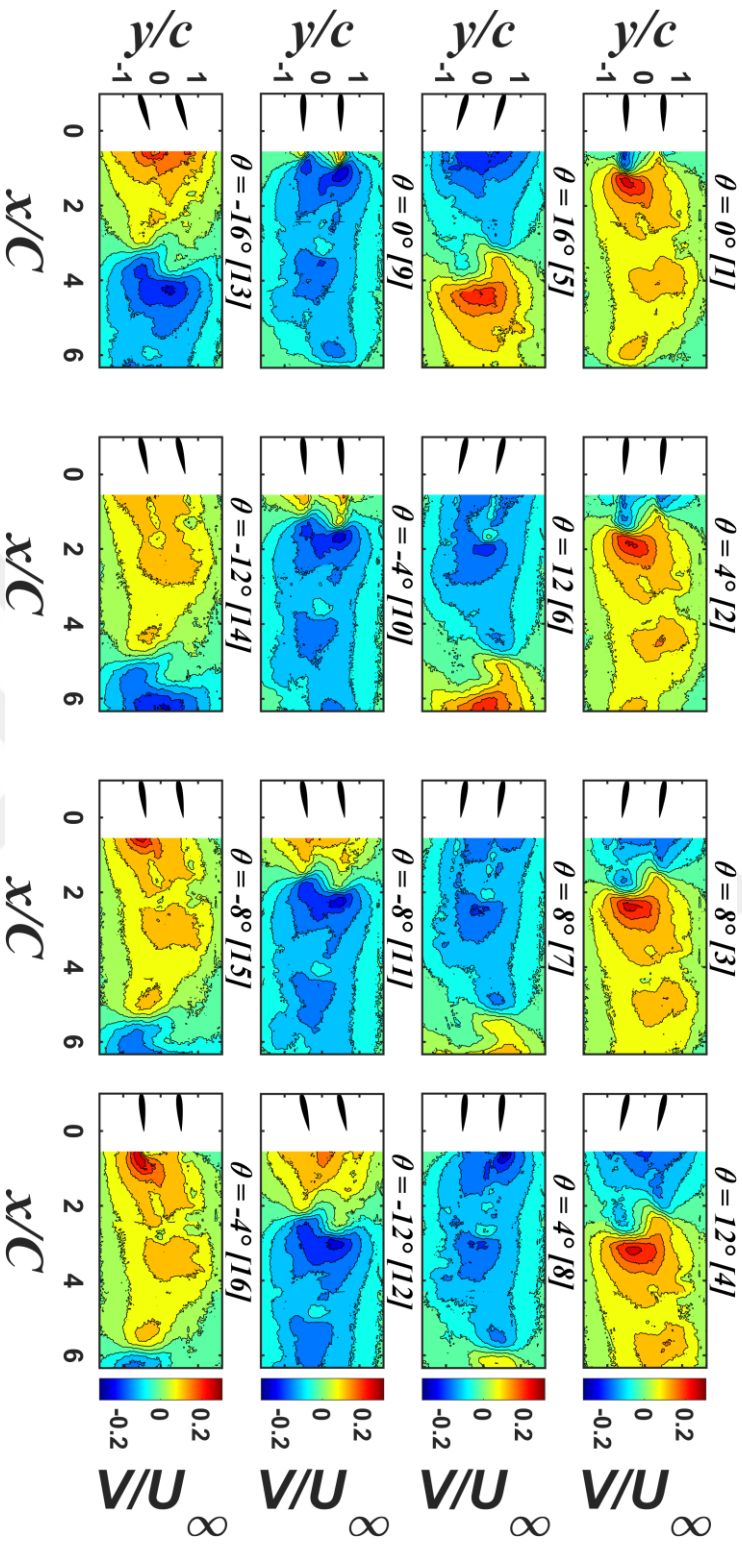


Figure A.25: Transverse Gust ratio contour plots of FOV for reduced frequency k = 0.251 and with a maximum amplitude of $\bar{\theta} = 16^{\circ}$ in-phase case at different phase angles

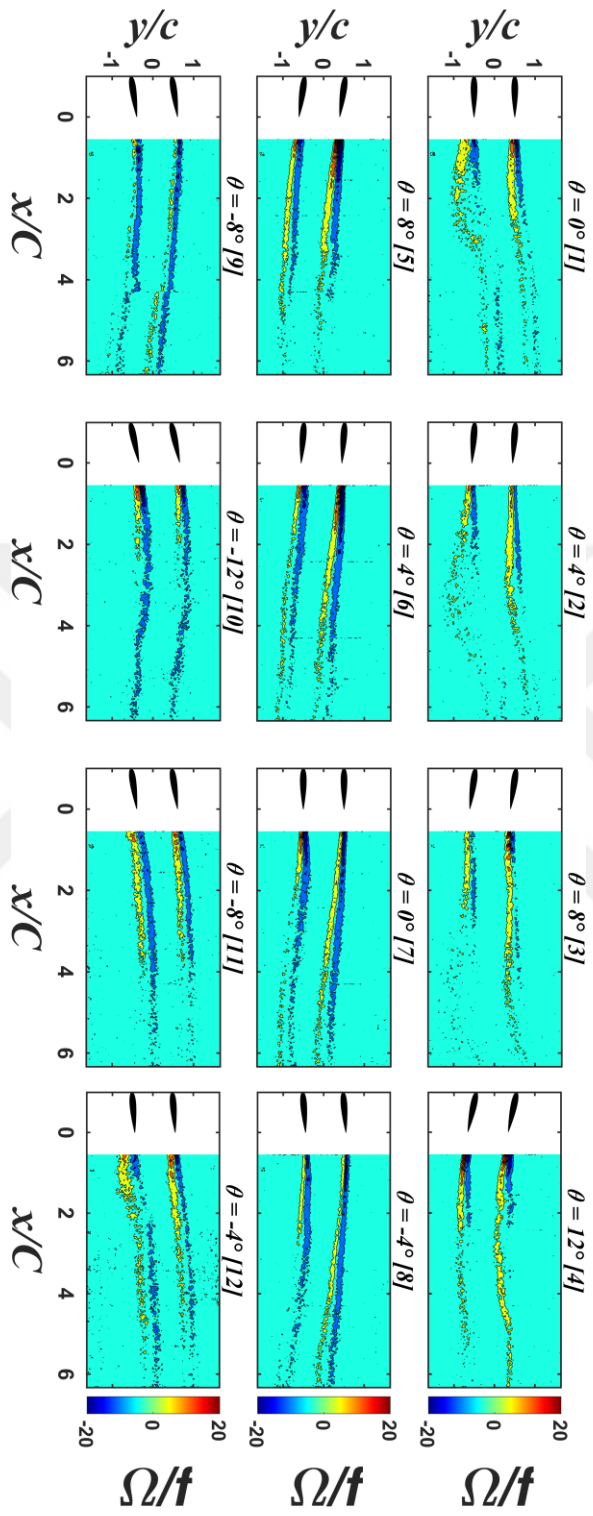


Figure A.26: Vorticity contour plots of FOV for reduced frequency k = 0.125 and with a maximum amplitude of $\bar{\theta} = 12^{\circ}$ in-phase case at different phase angles

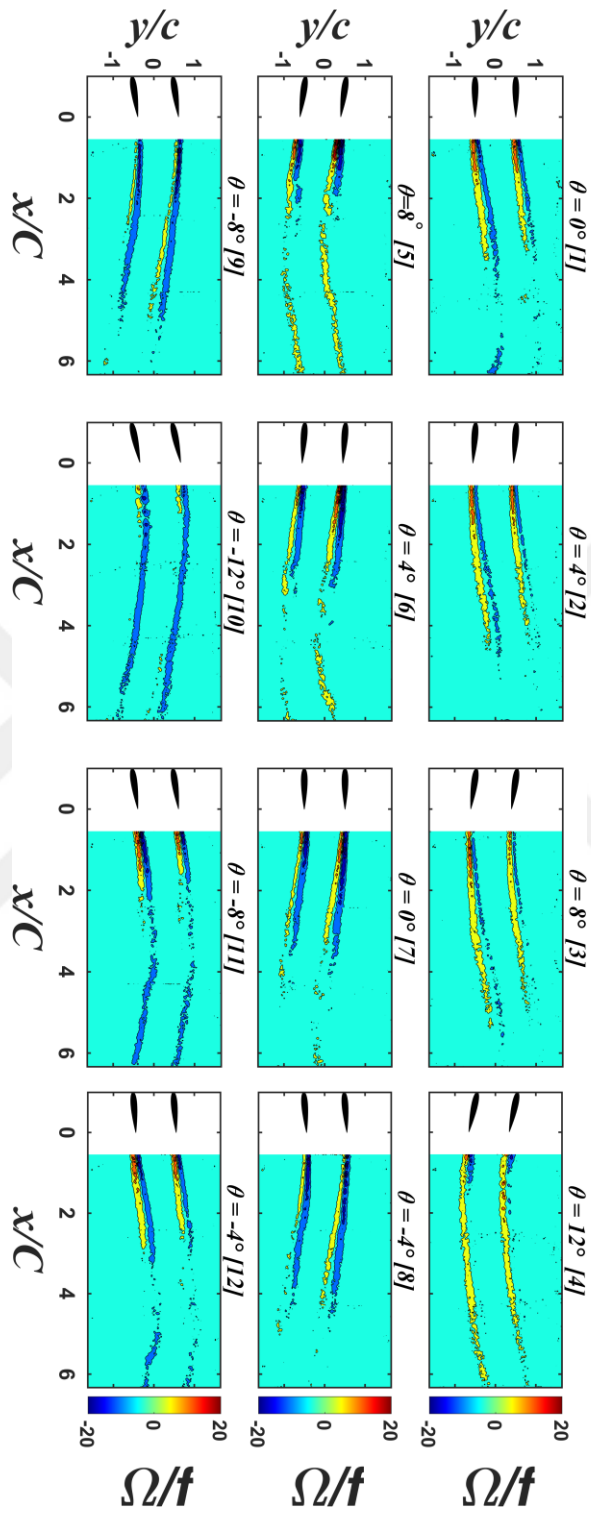


Figure A. 27: Vorticity contour plots of FOV for reduced frequency k = 0.188 and with a maximum amplitude of $\bar{\theta} = 12^{\circ}$ in-phase case at different phase angles

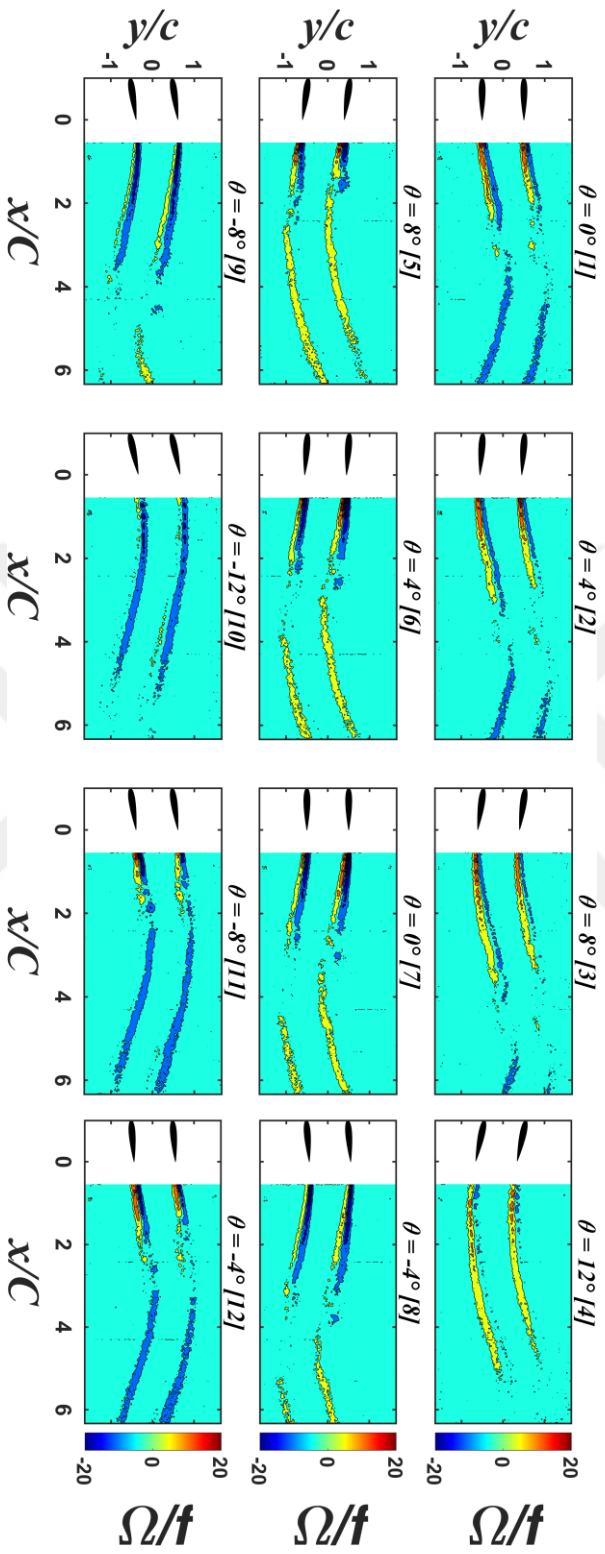


Figure A. 28: Vorticity contour plots of FOV for reduced frequency k = 0.251 and with a maximum amplitude of $\bar{\theta} = 12^{\circ}$ in-phase case at different phase angles

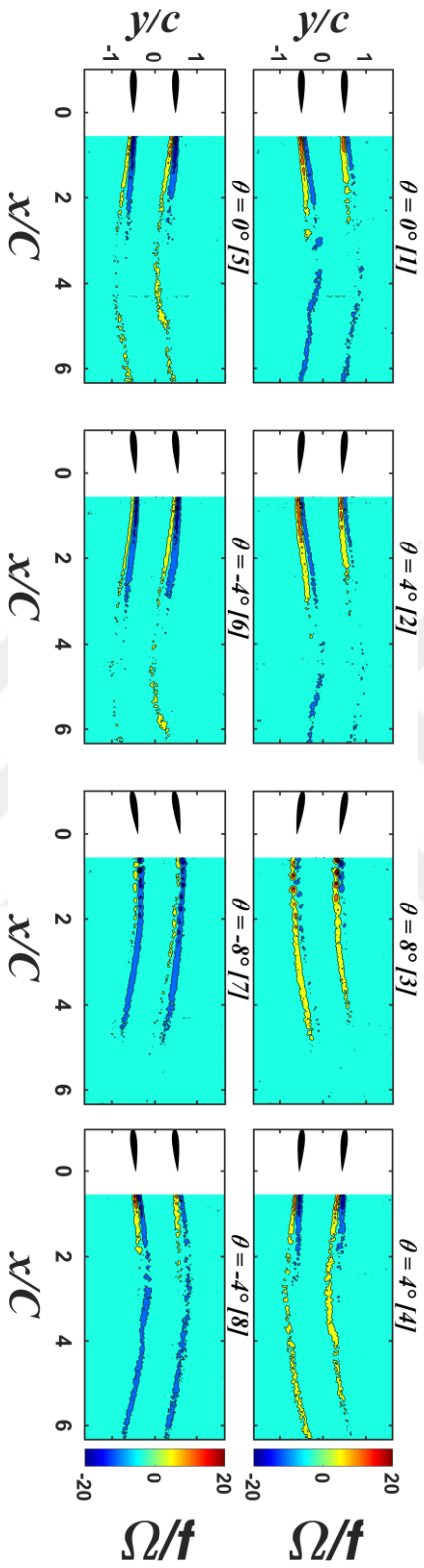


Figure A.29: Vorticity contour plots of FOV for reduced frequency k = 0.251 and with a maximum amplitude of $\bar{\theta} = 8^{\circ}$ in-phase case at different phase angles

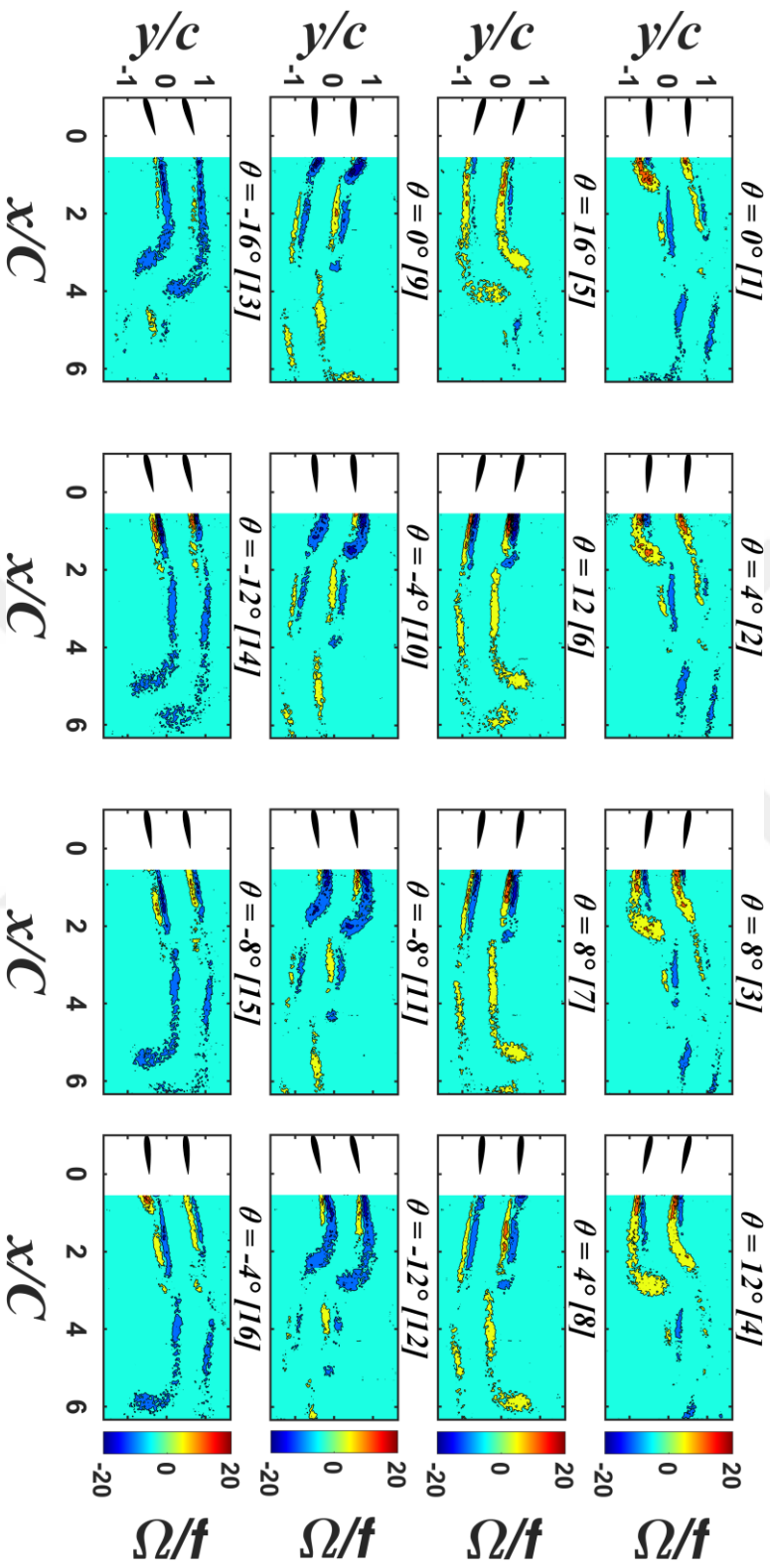


Figure A.30: Vorticity contour plots of FOV for reduced frequency k = 0.251 and with a maximum amplitude of $\bar{\theta} = 16^{\circ}$ in-phase case at different phase angles